UNIVERSITA' DEGLI STUDI DI PARMA

DOTTORATO DI RICERCA IN
"SCIENZA E TECNOLOGIA DEI MATERIALI"

CICLO XXX

3D ENGINEERED PHOTOANODES

FOR DYE-SENSITIZED SOLAR CELLS

Coordinatore:
Chiar.mo Prof. DALCANALE Enrico

Tutore:
Dr.ssa SANSON Alessandra

Dottorando: SANGIORGI Alex

Anni 2014/2017

“Life is 10% what happens to us and 90% how we react to it”

Dennis Paul Kimbro

Summary

Aim of the thesis

Energy and environmental issues are among the most dramatic and urgent challenges that modern society has to face. Critical factors, as the uncontrolled global energy demand, are in fact seriously jeopardizing the preservation of the planet and the survival of mankind. An important contribution to the improvement of the current situation could derive exploiting the sun for energy production, through photovoltaic devices.

Physicists and chemists have been interested for a long time in these technologies. Among all the different options, in the past 25 years lot of scientific community efforts and attention have been focused on an important technology that is rapidly evolving, commonly called Dye-sensitized Solar Cells (DSCs) [1]. These devices belong to the third generation photovoltaics. Their key features are high versatility, low cost and the use of environmental-friendly materials. A fundamental DSCs component is the photoanode (typically composed of titanium dioxide nanoparticles, NPs), which represents the device nucleus.

As negative electrode semiconductor material, TiO_2 guarantees superior electronic and optical properties and high dye loading capability thus enhancing both the performance and the stability of these devices. When used in form of supported nanostructured layer TiO_2 allows efficient photoanodes production. In DSCs, these films are normally realized using Dr. blade or screen-printing processes. The second one is mostly reported in literature as state of the art deposition technique for thick film; it is also cost-effective, able to realize big surface area and easily scalable to produce high-quality depositions. This process consists in forcing an ink through a screen by the motion of a squeegee blade, allowing to realize geometrically simple depositions. After a well-defined thermal treatment, the as-produced screen-printed film is essentially a flat mesoporous structure composed by ceramic NPs in contact with each other. This simple architecture is surely suitable for the desired application but perfectible, as it produces a random porous structure of TiO_2 electrode that gives rise to some undesired characteristics. These include low conductivity due to the tiny crystals (measuring 10 – 30 nm in diameter), that compose the film [2]. These small sizes do not support the formation of space charge region. This absence of an energy barrier at the electrode/electrolyte interface enhances the recombination rate of photo-injected electrons barrier [3] therefore decreasing the performances. Moreover, in a random porous network the access to the entire film surface, for dye and electrolyte, is very limited [4,5].

Consequently, techniques for fabricating large surface area TiO_2 photoanodes with good conductivity and improved accessibility to the semiconductor are of great interest for DSCs. Literature reports some alternative semiconductor layer geometries, for e.g. well-separated micro-tubes obtained by using the complex and highly cost photolithography method, that could improve these and other DSCs aspects [6]. However, there is a family of emerging techniques named Additive Manufacturing (AM) that could be useful to decrease the cost and increase the spreading of these architectures. They allow the creation of complex 3D objects (also at microscale length) like rods, columns, pillars and so on, with a layer-by-layer approach thus avoiding screens, masks, molds, etc. AM techniques offer some interesting advantages like reduced amount of wastes, the easiness to produce complex parts just starting from a CAD file and, finally, their excellent industrial scalability.

In this thesis, 3D engineered photoanodes for DSCs (Figure 1) were produced using two different AM techniques: robocasting (micro-extrusion) and inkjet printing . They were considered to produce three-dimensional structures, as micro-pillars, to improve DSCs performance. These features, composed of TiO_2 NPs were deposited on a mesoporous TiO_2 film obtained using the wet-powder spraying (WPS) technique. The latter is nowadays commonly used in the organic photovoltaics (OPVs) field as reliable deposition process [7] but it can also be seen as a promising low costs and environmental-friendly scree-printing alternative to deposit porous TiO_2 films [8,9].

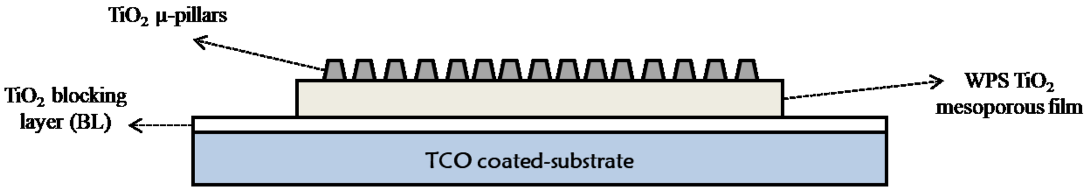

Figure 1. 3D engineered DSC photoanode

The work reported in this thesis was therefore focused on the production of highly performing, large area DSC photoanodes using unconventional deposition techniques.
To pursue this objective, the suspension/inks optimization as well as the accurate deposition processes parameters tuning were mandatory.

In detail, the experimental activity was divided in:

- Formulation and optimization of TiO_2-based ceramic suspensions for WPS. The optimal one was then used to deposit high-transparent mesoporous films that were deeply characterized and finally employed to produce working DSC prototypes.
- Formulation and optimization of highly-concentrated TiO_2-based inks for micro-extrusion. The best formulation was used to realize coarse 3D structures that, afterwards, were used to produce functioning DSC prototypes. Functional characterizations were performed to evaluate the micro-pillars effects on the DSCs performance.
- Formulation and optimization of concentrated TiO_2-based inkjet inks. An accurate evaluation of the several formulation components was performed aiming at producing a suitable ink.

All the depositions were performed using a stand-alone multi-head work machine thus highlighting both the high-degree of automation and the easier scalability of these processes.

References

[1] B. O'Regan, M. Gratzel, *A low cost, high efficiency solar cells based on dye-sensitized colloidal* TiO_2 *film*, Nature, 1991, 353, 737-740.

[2] M. Gratzel, *Perspectives for dye-sensitized nanocrystalline solar cells*, Progress Photovoltaics: Research and Applications, 2000, 8, 171-185.

[3] A. Zaban, S. G. Chen, S. Chappel, B. A. Gregg, *Bilayer nanoporous electrodes for dye sensitized solar cells,* Chemical Communications, 2000, 0, 2231-2232.

[4] M. K. Nazeeruddin, A. Kay, I. Rodicio, R. Humphry-Baker, E. Mueller, P. Liska, N. Vlachopoulos, M. Gratzel, *Conversion of light to electricity by cis-X2bis(2,2'-bipyridyl-4,4'-dicarboxylate)ruthenium(II) charge-transfer sensitizers (X = Cl-, Br-, I-, CN-, and SCN-) on nanocrystalline titanium dioxide electrodes,* Journal of the America Chemistry Society, 1993, 115, 6382-6390.

[5] A. Fillinger, B. A. Parkinson, *The adsorption behavior of a Ruthenium-based sensitizing dye to nanocrystalline* TiO_2 *coverage effects on the external and internal sensitization quantum yields,* Journal of the Electrochemical Society, 1999, 146, 4559-4564.

[6] T. H. Meen, C.J. Huang, Y. W. Chen, L. W. Ji, C. C. Diao, H. H. Chung, *Study of different* TiO_2 *electrode structures on Dye-Sensitized Solar Cell*, Key Engineering Materials, 2008, 368-372, 1716-1719.

[7] L. La Notte, D. Mineo, G. Polino, G. Susanna, F. Brunetti, T.M. Brown, A. Di Carlo, A. Reale, *Fabrication of fully-spray-processed organic photovoltaic modules by using an automated process in air,* Energy technology, 2013, 1, 12, 757-762.

[8] J. Halme, J. Saarinen, P. Lund, *Spray deposition and compression of* TiO_2 *nanoparticle films for dye-sensitized solar cells on plastic substrates*, Solar Energy Materials and Solar Cells, 2006, 90, 887-899.

[9] A. Ranga Rao, V. Dutta, *Low-temperature synthesis of* TiO_2 *nanoparticles and preparation of* TiO_2 *thin films by spray deposition*, Solar Energy Materials and Solar Cells, 2007, 91, 1075-1080.

Chapter 1

Dye-sensitized Solar Cells (DSCs)

1.1 Introduction

Energy and environmental issues are strongly related and are among the major challenges of modern society. Despite the global economic crisis, factors as the ever-growing demographic increase and the constant growth of developing countries contributed to exasperate energy demand. Mankind needs energy for living. The energy in food is necessary to sustain our body and its functions (100 W), but to make our life more comfortable we need 30 times more energy. The extensive use and growing dependence on electrical and electronic equipment increased the energy/power requirements on a global scale. With dwindling fossil-fuel reserves, there is an urgent need to find alternative energy resources to meet the growing demand; they must be efficient, cost-effective and ecologically friendly. The harnessing of solar energy, in this context, becomes very attractive; solar power is, in fact, potentially higher than any other source (Figure 1.1).

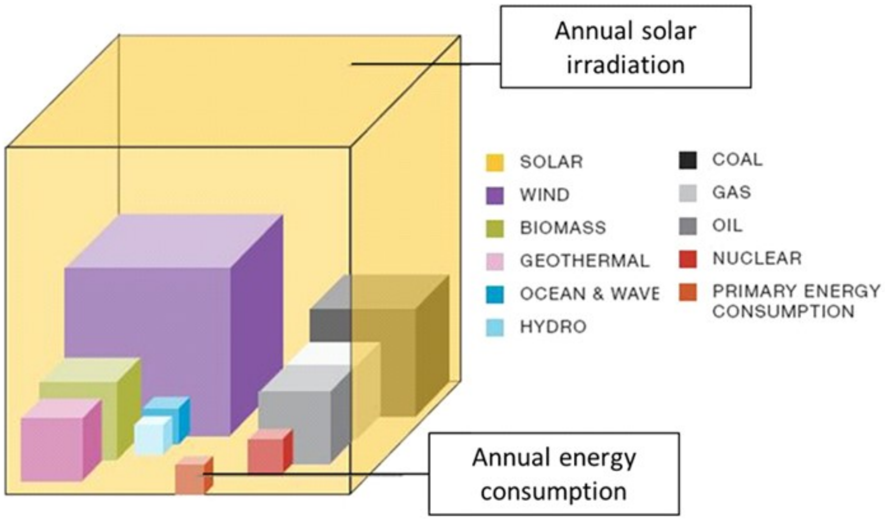

Figure 1.1. Comparison between annual energy consumption and alternative energy sources potential [1].

As a consequence, the sun is nowadays and will be in the next decades one of the most exploited renewable sources to produce electricity (Figure 1.2).

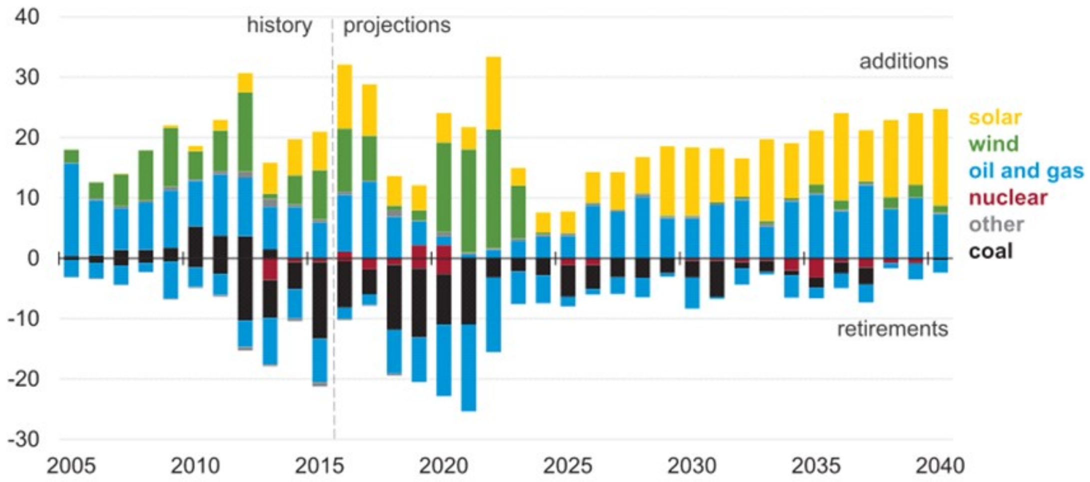

Figure 1.2. Annual electricity generating capacity (gigawatts) additions and retirements [2].

The sunlight reaching the earth surface every day (120000 TW) far exceeds the annual global demand (estimated about 18 TW); thus, a moderately efficient photovoltaic solar cell array (with 8-10% efficiency), covering a limited area of the planet, would be theoretically able to provide a huge amount of electric power helping to reduce also the greenhouse-gas emissions.

This prospective suggests the fundamental role of science in this field, in particular, in the development and optimization of efficient photovoltaic technologies.

1.2 PV technologies

Among all the renewable energy devices, photovoltaic technologies are considered as the most promising ones.

A photovoltaic cell (PV) is an electrical device that converts light energy directly into electricity using the photovoltaic effect [3,4]. Based on this physical principle, different kind of PV generations were produced from 1954 (first crystalline silicon solar cell with 6% efficiency produced at Bell laboratory) until today. The first generation (1G) solar cells, based on monocrystalline and polycrystalline silicon (mc-Si and pc-Si), have achieved power conversion efficiency up to 25% and have totally dominated the PV market so far. Silicon solar cell (Figure 1.3) has a quite simple structure that is based on two material layers: n-type, p-type and their interface, namely pn-junction (created by the connection between the previous two).

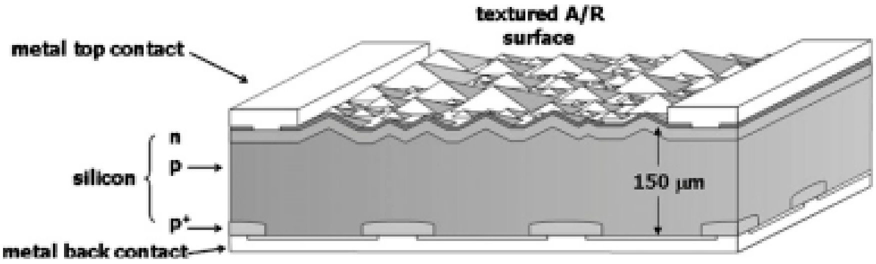

Figure 1.3 Basic silicon solar cell structure [3]

The n-type is a silicon layer doped with V group elements, traditionally phosphorous that has extra electrons and works as donor (anode). The p-type layer is doped with group III elements such as Boron that, lacking electrons, can create "holes" and consequently becomes the receptor (cathode). Light reception during solar illumination takes place in the pn-junction where each absorbed photon generates an electron-hole pair by exciting electrons from the junction valence band to the conduction band (electrons are driven to the negative layer and holes are left as positive). This mechanism leads to different potentials in the anode and cathode inducing an electron flows into the external circuit producing electricity. In Figure 1.4 a scheme relative to the p-n junction and photovoltaic effect is reported [5].

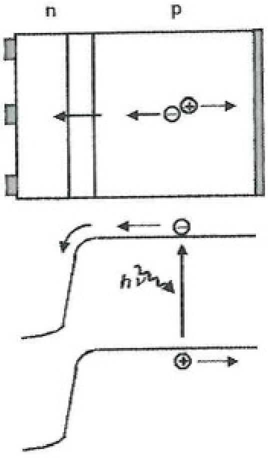

Figure 1.4 Scheme of p-n junction of solar cell (up) and relative photovoltaic effect (down)

High production costs and environmental issues of these systems have promoted the search for environmentally friendly and low-cost solar cells alternatives.

Second-generation (2G) technologies are single-junction devices that aim to use less material (reducing the total costs) while maintaining the efficiencies of 1G PV. 2G solar cells use amorphous-Si (a-Si), CuIn(Ga)Se_2 (CIGS), CdTe or polycrystalline-Si (p-Si) deposited on low-cost substrates such as glass (Figure 1.5).

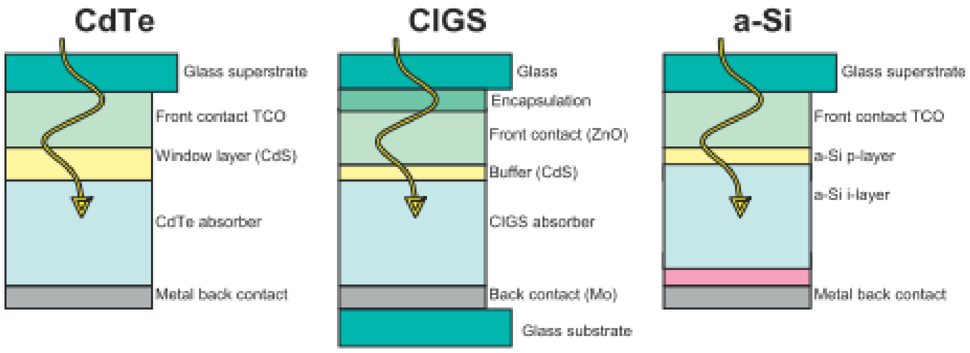

Figure 1.5. Schematic representations of thin-film CdTe, CIGS and a-Si thin-film PV devices

These technologies work because CdTe, CIGS and a-Si absorb the solar spectrum much more efficiently than pc-Si or mc-Si and use only 1 – 10 µm of active material. 2G PV offer the potential to reduce costs, financial pay-back and energy pay-back times compared to 1G. Efficiency and fabrication costs per unit area remain comparable to 1G technology. Research results from leading laboratories have provided ample evidence of thin-film PV potential; 21% (CdTe), 22% (CIGS). However, PV based on CdTe and CIGS has been slow to scale up. This is partly due to poor material reproducibility and uniformity over large areas and, similar to the first generation cells, high production and environmental costs (elements toxicity).

Finally, third generation solar cells (3G) emerged and includes Dye-sensitized Solar Cells (DSCs, efficiency ≈ 13%) [6], organic solar cells (≈ 11%), quantum dots solar cells (≈ 11.5%) and, recently, perovskite solar cells (≈ 21.1%) [3].

3G solar cells production is easier, cheaper and the cells are reasonably efficient even if they are still behind Si-based solar cells conventional efficiency values. The overall best research-cell efficiency for each PV technologies are shown in Figure 1.6.

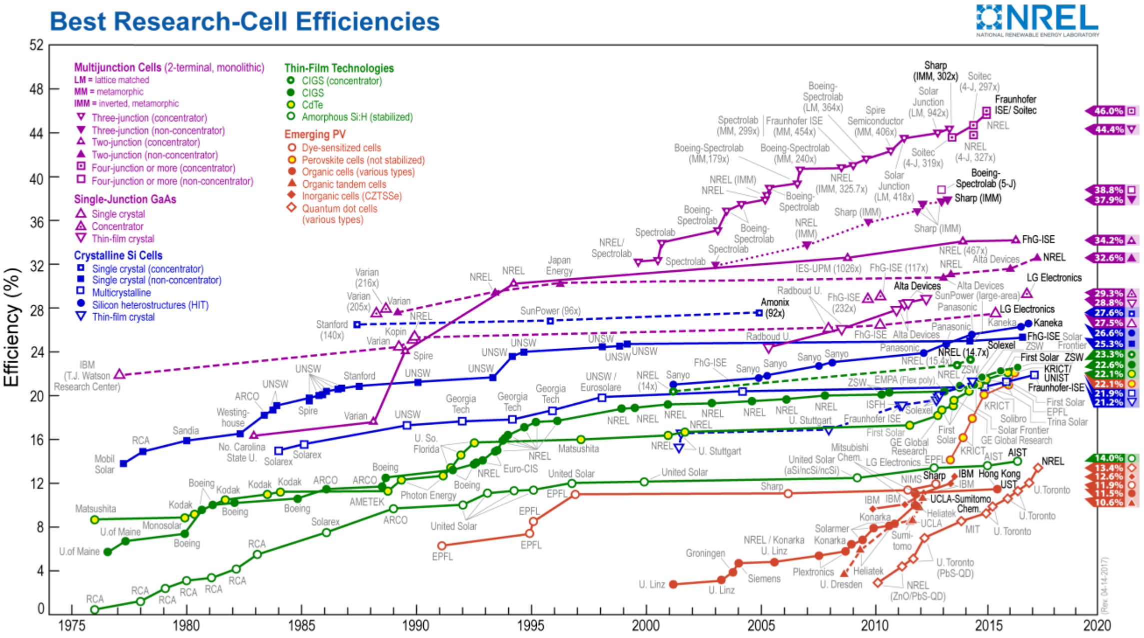

Figure 1.6. PV best research-cells efficiency (2017) [7]

1.3 Dye-Sensitized Solar Cells (DSCs)

DSCs have generated intense interest into scientific community providing a technically and economically technology complementary to the p–n junction photovoltaic devices [8-12]. DSCs, in fact, offer some important advantages like lightweight, flexibility, design opportunities (such as transparency and several colors) and so on. In contrast to the conventional systems where semiconductor acts both as light absorption and charge carrier transport, here the two functions are distinguished (similar to the photosynthesis process in plants). This separation leads to lower purity demand on raw materials and consequently makes DSCs a low-cost solar cells alternative. In particular, DSCs simulate the chlorophyllian photosynthesis (Figure 1.7).

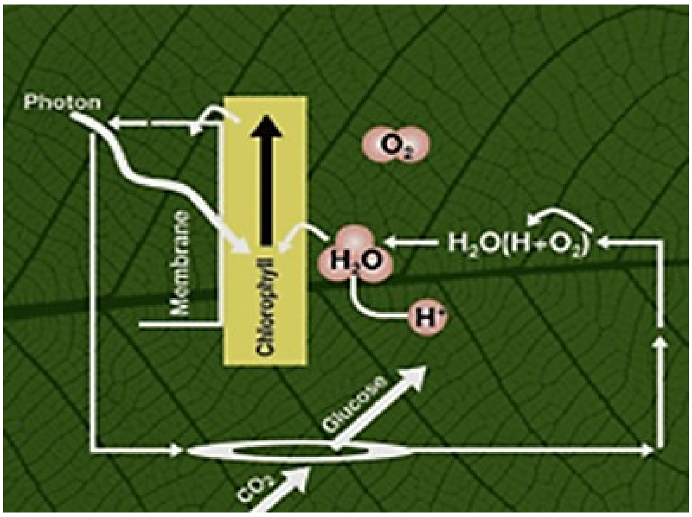

Figure 1.7. Mechanism of the chlorophyllian photosynthesis [13]

In plants, light is absorbed by chlorophyll which transfers the photogenerated electrons to the reactive centers where CO_2 and H_2O become glucose and O_2. The DSSC is an artificial device the tries to mimic the functioning mechanisms of the leaf.

Figure 1.8 shows its conventional architecture: the heart is the mesoporous oxide layer composed by a network of TiO_2 nanoparticles sintered together to establish electronic conduction.

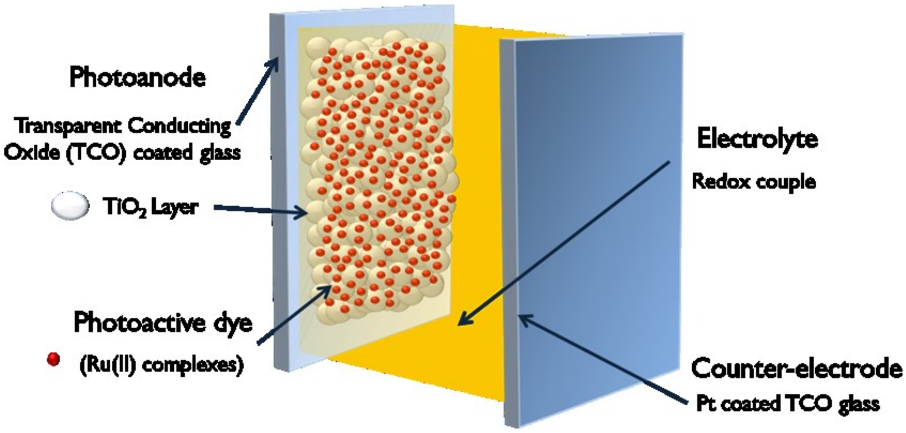

Figure 1.8. Schematic structure of a traditional DSC

Normally the film thickness is ca. 10 μm and the nanoparticle size is 10-30 nm in diameter. The porosity is 50-60%. The mesoporous layer is deposited on a transparent conducting oxide (TCO) on a glass or plastic substrate. The most commonly used substrate is glass coated with fluorine-doped tin oxide (FTO). Attached to the nanocrystalline film surface there is a monolayer of the charge-transfer dye (typically

Ruthenium complex). Photoexcitation of the latter results in the injection of an e- into the oxide conduction band, leaving the dye in its oxidized state. The dye is restored to its ground state by electron transfer from the electrolyte, usually an organic solvent containing the iodide/triiodide redox system. The I_3^- ions formed by oxidation of I^- diffuse at short distance (<50 µm) through the electrolyte to the cathode, which is coated with a thin layer of platinum catalyst, where the regenerative cycle is completed by electron transfer to reduce I_3^- to I^- [13]. For a simpler understanding the overall process is schematized in Figure 1.9.

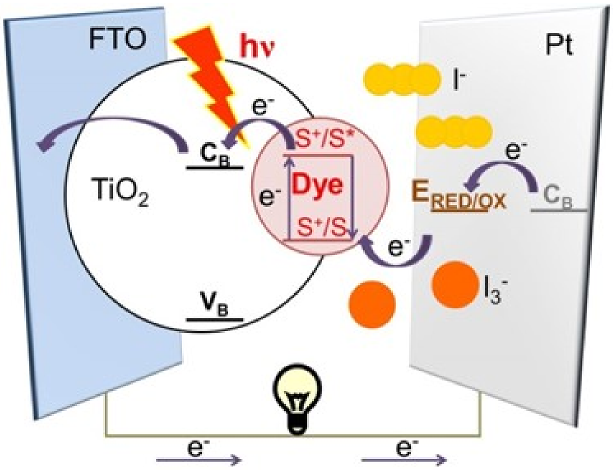

Figure 1.9. DSCs working mechanism

In order to realize highly efficient cells, the photoanode is normally treated twice with $TiCl_4$ solution: once before and once after the mesoporous TiO_2 layer deposition. The first treatment enhances the bonding strength between FTO and porous TiO_2 layer and it blocks charge recombination between e^- in the semiconductor layer and redox couple [14]. The second one enhances the porous semiconductor layer surface roughness consequently increasing the dye adsorption and the photocurrent.

Figure 1.10 shows the energy levels in the working principle of a DSC. In absence of light the TiO_2 Fermi energy level will be aligned with the redox energy level.

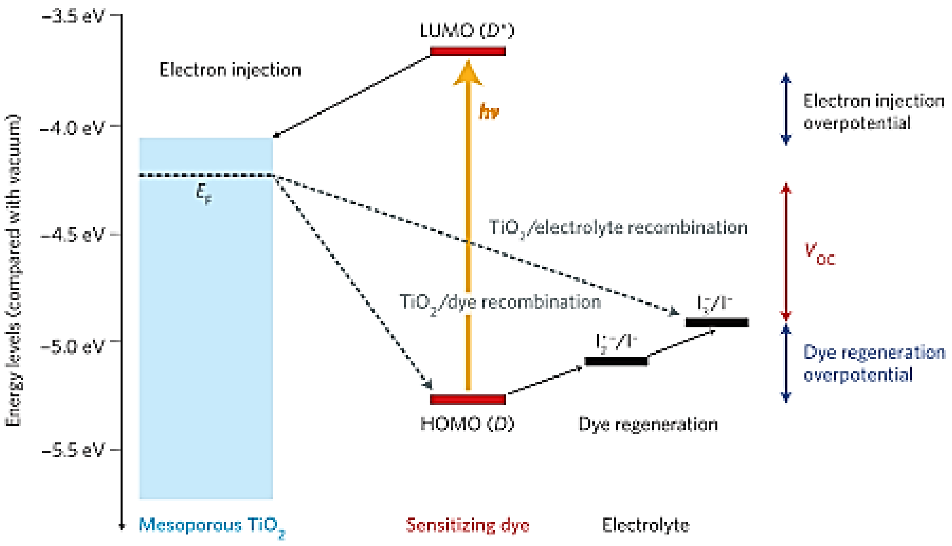

Figure 1.10. DSCs energy level and device operation.

Upon illumination the dye molecules (D) attached to the mesoporous TiO_2 surface absorb photons of energy, hv. Electrons in the highest occupied molecular orbital (HOMO) of the dye molecules will be excited into the lowest unoccupied molecular orbital (LUMO), (Eq.1).

$$D + hv \rightarrow D^*$$

where D* is the excited dye molecule. Electrons in the LUMO of the dye will be then transferred to the mesoporous TiO_2 within femtoseconds, $\sim 10^{-15}$ s. This process is called electron injection. As a consequence, the TiO_2 Fermi level will be increased towards the conduction band (CB) and the dye molecule will be in an oxidized or ionized state (D^+), Eq. (2).

$$D^* \rightarrow D^+ + e^- (CB)TiO_2$$

The oxidized dye receives then electrons from the reduced molecules (REDs) of the redox couple (present into the electrolyte) for its regeneration and consequently the reduced redox couple molecules become oxidized (OXs). OXs diffuse to the counter-electrode and are then reduced to recreate the electrolyte molecules. This reduction process is due to the electrons drives from the external load and generated from the photoanode that complete the circuit [12]:

$$e^{-}\,(CB)TiO_2 \rightarrow \text{external load} \rightarrow e^{-}\,(\text{counter-electrode})$$

$$OX + e^{-}\,(\text{counter-electrode}) \rightarrow RED$$

$$RED + D^{+} \rightarrow OX + D$$

The overall processes described above allow the generation of electric power from sunlight without any permanent chemical transformation. In Figure 1.8 the three main driving forces that contribute to the final photovoltaic cell efficiency are reported: the Open Circuit Potential (V_{oc}), and the overvoltages required for the dye regeneration (ΔV_{reg}) and electrons injection (ΔV_{inj}). The V_{OC} indicates the potential difference between the TiO_2 conduction band (CB) and the redox potential of the electrolyte molecules. ΔV_{inj} is related to the overpotential required to fill the gap between the LUMO level of the dye and the TiO_2 CB. ΔVreg refers to the overpotential required to fill the gap between the redox species potential and the dye HUMO level [15,16].

In order to achieve high efficient DSCs a high V_{OC} and low ΔV_{inj} and ΔV_{reg} are therefore required; this means that a fundamental element for the correct operation of DSCs is the unidirectional electron flux through different components. The process is however subjected to parasitic reactions, known as "back transfer", which cause energy losses and a drop in the device efficiency [12,17]. Figure 1.11 compares the correct electron transfers (green arrows) to the back transfer reactions (red arrows).

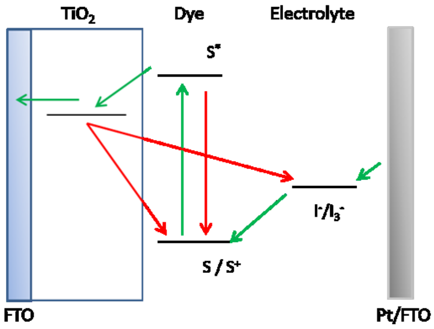

Figure 1.11. DSCs correct electron transfer (green arrows) vs. back transfer reactions (red arrows)

These reactions basically involve the recombination of the electron injected into the semiconductor layers with the oxidized state of the redox couple and with the dye. For the latter, moreover also the spontaneous relaxation is possible. It is also worth to remember that, differently from the bulk phenomena of p-n junction based cells, in DSCs the recombination is mainly an interfacial reaction, due to the peculiar structure and operating principle of these systems [18].

The photovoltage generated under illumination corresponds to the potential difference between the Fermi level of the electron in the TiO_2 film and the redox potential of the redox couple into the electrolyte (V_{OC}) [12]. Moreover, the photocurrent depends on the incident sunlight harvest efficiency, charge carrier transportation and collection efficiencies. The overall sunlight to electrical power conversion efficiency (η or PCE) of the DSCs is determined therefore by:

$$\eta = \frac{P_{MAX}}{P_{IN}} = \frac{J_{SC} \times V_{OC} \times FF}{P_{IN}}$$

where P_{MAX} is the maximum obtainable power, P_{IN} is the intensity of the incident light, J_{SC} is the photocurrent density measured at short circuit and FF is the solar cells Fill Factor. The obtainable P_{MAX} in a photovoltaic device is the product of two terms: maximum current I_{mpp} and maximum voltage V_{mpp}. The FF is defined by the equation:

$$FF = \frac{I_{mpp} \times V_{mpp}}{I_{SC} \times V_{OC}}$$

The FF can assume values between 0 and 1 and reflects the electrical losses during DSCs operation [12]. These photovoltaic parameters are often measured under standard irradiation conditions (1000 W/m^2 AM 1.5) acquiring a traditional current density-voltage curve (J-V curve). DSC efficiency, as defined above however, does not take into account the amount of light absorbed by the dye molecules but measures the overall conversion of incident sunlight to electrical power. Another important parameter is the "Incident photon-to-electrical-conversion efficiency" (IPCE) which describes a quantum yield term for the overall charge injection collection process measured using monochromatic light. IPCE measures the percentage of the absorbed light converted into current and it can be expressed as follows:

$$\mathrm{IPCE}\,(\lambda) = 1240\,\left({}^{\mathrm{I_{SC}}}\!/_{\lambda_{\varphi}}\right)$$

where λ is the wavelength, I_{SC} is the current at the short circuit (mA/cm^2) and φ is the incident radiative flux (W/m^2) [19]. Nowadays, the highest DSC efficiency obtained is equal to 13% [5].

1.3.1 DSCs components

The correct DSC operation mechanism derives from the optimization of its constituents and the deep synergy between them. The study and the complete comprehension of the different components are really important to continuously improving their efficiency and then the overall device performance. In this section, all the elements constituting a DSC are singularly listed and discussed.

Substrates

The substrate nature has a dominant impact on the possible process and materials that can be applied into the solar cell and consequently on the final performance. Recently, lightweight DSCs based on flexible substrates (in foil, mesh or wire shapes) have attracted much attention, due to the possibility to open new application area like portable electronics and wearable devices. The most mature industrial production processes still remain focused on rigid substrates, like FTO glass, for their enhanced physical-chemical stability and higher performance.

Counter-electrode

The counter-electrode injects electrons into the electrolytes to catalyze the reduction reaction after charge injection from the photo-oxidized dye. If the counter-electrode properties are increased also the device Fill Factor rises because this parameter is influenced by a series resistance (R_s). This is a combination of all the resistances inside the cell (charge transfer on the electrodes, diffusion resistance, substrate resistance) and it is strongly affected by the charge transfer resistance at the counter-electrode side (R_{CT}). A low R_{CT} value means high electrons transfer rate from counter-electrode to electrolyte for the triiodide reduction at the catalytic interfaces of the counter-electrode.

Conventional transparent conductive oxide layer (FTO or ITO), normally used as electrode substrate, presents a low rate of reduction and so the counter-electrode must be coated with a catalytic material to accelerate the reaction. The best material for this purpose is Platinum (Pt) thanks to its superior conductivity and high electrocatalytic activity. It also possesses high stability in air or in water even at high temperature, but it is very expensive and scarce in nature. In addition, Platinum is not effective as counter-electrode for other redox couples (e.g. $Co^{(II/III)}$-based complex and polysulfide) containing different ligands molecules. Moreover, Pt counter-electrode suffers from fast metal dissolution due to the corrosive $I_3^-/3I^-$ redox couple that decreases the final device long-term stability [20,21].

The most considered common materials able to replace Pt are based on carbon materials (e.g. CNTs and graphene [22,23]), transition metal compounds (TMCs) [24-26, 27-29], hybrids composite materials (e.g. rGO/CNTs and carbon/TMCs) and conductive polymers (e.g. polyaniline, polypyrrole and PEDOT [30-34]).

Sensitizers

The sensitizer is the heart of the DSC, it harvests sunlight and produces photo-excited electrons at the semiconductor interface [35]. To efficiently perform its function, it should possess a chemically absorbed group (like carboxylates, sulphonates and phosphate) able to make bonds with the semiconductor surface, appropriate LUMO and HOMO energy levels for reducing the overpotentials required for the electrons injection and for its regeneration. Moreover, for an efficient light harvesting is important to have high molecular extinction coefficients in the visible and near-infrared region. The most studied dye molecules are Ruthenium-based complex but a lot of research activities were carried out to develop new efficient and highly stable dye molecules. Nowadays, the different sensitizers are:

- Ruthenium-based dyes;
- organic dyes (metal-free);
- porphyrin-based dyes;
- quantum dots sensitizers (inorganic semiconductors with tunable size/shape properties);
- perovskite sensitizers (e.g. $CH_3NH_3PbX_3$ with X=Cl, Br, I).

In addition to this list many researchers are focusing on natural photosensitizers because of their low costs, abundance and environmental impact. The main issue related to these molecules is the obtained final efficiency, which is still low compared to the synthetic ones [36].

Electrolytes

The electrolyte is another crucial components in DSCs [3] providing high conductivity between the positive and the negative electrodes; it is responsible for the inner charge carrier transport between electrodes and continuously regenerates the dye and itself during DSC operation. The electrolyte has great influence on both the light-to-electric conversion efficiency and long-term devices stability. The redox couple inside the electrolyte transfers electrons from the counter-electrode to the oxidized dye. Its solubility and ionic mobility in organic solvent, the driving force for the dye regeneration and fast electron transfer kinetics with a minimal overpotential at the counter-electrode, are fundamental characteristics for an efficient redox electrolyte. There are three main categories of electrolytes (in relation to their physical state): liquid, quasi-solid electrolytes and solid-state hole transport materials (HTMs). Liquid electrolytes are mainly based on organic solvent, ionic liquid and, recently, also water [37]. In order to fix fluid leakage issues related to liquid electrolytes usage, quasi-solid electrolytes were studied. They are in a special state between solid and liquid. Several methods are used to solidify liquid electrolytes, in particular: i) using organic polymer gelators or ii) inorganic gelators (such SiO_2 and nanoclay) [3,38]. Finally, HTMs are applied to further increase solar cells stability and are based on solid-state ionic conductors, inorganic materials (like CuI, and CuSCN) and organic ones (P3HT and Spiro-OMe-TAD). These materials do not work as electrons mediator and ionic conductor but their activity is based on holes mobility. The redox couple plays a central role in the electrolyte; these molecules must complete the electrical working circuit regenerating the dye. Thanks to its good solubility, low light absorption, slow recombination kinetics with TiO_2 electrons and suitable redox potential, the iodine based redox couple ($I_3^-/3I^-$) is the most used in DSC application. Nevertheless, in order to increase the cell efficiency and stability, other redox couple based on different standard potential than triiodide has been developed: polypyridyl complex $Co^{(II/III)}$, ferrocenium/ferrocene (Fc/Fc$^+$) couple, Cu$^{(I/II)}$ complex, disulfide/thiolate mediator (T_2/T^-) [39] and metal polysulfide redox couple [40].

1.4 Nanostructured photoanode

This thesis is focused on the production and characterization of an engineered tridimensional microstructure to be used as DSC photoanode. In this section this electrode will be treated more specifically, starting from the most performing semiconductor (TiO_2) still used to produce it and also showing its main properties and possible improvements. Finally, the experimental activity carried out in this field will be introduced.

TiO_2 exists in nature as three different polymorphs: anatase, rutile and brookite (Figure 1.12).

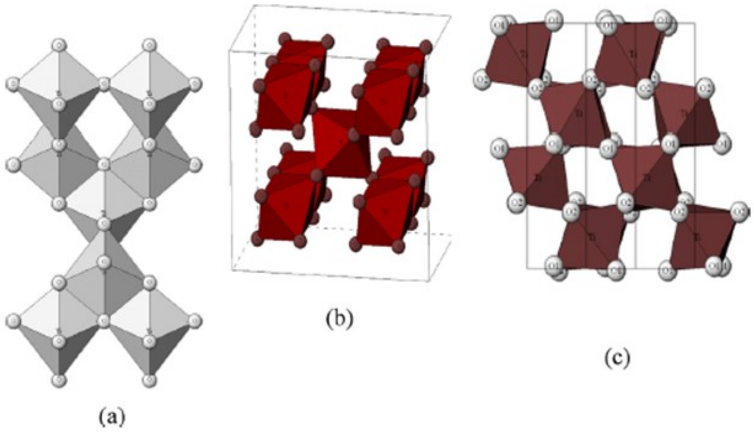

Figure 1.12. TiO_2 crystalline structures: a) anatase, b) rutile, c) brookite [41]

The most stable form, and primary TiO_2 source is rutile; anatase and brookite are metastable and transform into thermodynamically stable rutile after calcination at temperature over ≈ 500°C. In all the different forms, titanium atoms (Ti^{4+}) are coordinated to six oxygen (O^{2-}) atoms, in TiO_6 octahedra. Anatase structure consists in corner-sharing octahedral forming (001) planes, which results in a distorted tetragonal structure. On the other hand, in rutile the octahedra share edges at (001) planes to give a tetragonal structure and in brookite edges and corners are shared to give an orthorhombic structure. The anatase unit cell parameters are a/b = 3.784 Å, c = 9.513 Å; for rutile a/b = 4.594 Å, c = 2.958 Å and for brookite a = 5.455, b = 9.182 Å and c = 5.143 Å. TiO_2 is typically an n-type semiconductor due to the oxygen deficiency; the band gap is 3.2 eV for anatase, 3.0 eV for rutile and 3.2 eV for brookite [41]. The anatase phase is preferred for photovoltaic applications because of its potentially higher conduction band edge energy and lower recombination rate of electron-hole pairs [42]. As afore-mentioned, Ti^{4+} atoms are in a distorted octahedral structure and their electronic configuration is $3d^0$. In the anatase form, the valence band (VB) is mainly composed of 2p orbital of oxygen, hybridized with Ti 3d orbitals, while the conduction band (CB) is constituted only by the latter. This means that the electrons in VB and CB are in orbitals of different parity. For this reason the probability of spontaneous electronic relaxation from CB to VB is reduced, and so is the probability of the electron-hole recombination. Finally, among different semiconductors, TiO_2 is the most suitable one for DSC applications because it satisfies all the specific requirements needed such as photoactivity, absorption in the near UV range, chemical inertness, photostability, low-cost and low-toxicity.

The key breakthrough for the earliest DSCs development was the production of an efficient photoanode by using a mesoporous (pore diameter 5-50 nm) nanostructured TiO_2 film [9,10]. The latter allowed to increase dramatically the solar radiation absorbed by the device. Compared to a flat and dense morphology, the mesoporous microstructure produces an enormous increase in the film surface area, so that the light reaching the photoanodes hits a multitude of different layers of dye adsorbed onto the nanoparticles. Another photoanode role is the charge collection and transport, made possible by the nanocrystalline structure, through which the photogenerated electrons may reach the external load conserving their electrochemical potential. One of the crucial factors for DSCs success is that a film with such properties can be obtained using low-cost and highly reliable techniques [12,17,42-44]. However, in order to obtain an efficient ceramic layer, strict compositional and morphological controls are needed. Firstly, anatase TiO_2 is the most suitable for this application: DSC, based on same thickness anatase and rutile photoanodes were tested showed comparable Voc, but current density Jsc 30% higher for the anatase cell. This difference was mainly attributed to the lower amount of adsorbed dye on the rutile layer, due to is lower surface area. In addition, the charge transfer inside the rutile film resulted to be slower than in the anatase one. The motivation relied on the lower coordination number of the former reason for a less efficient conduction network [45]. The layer thickness of the photoanode must be optimized as well. Up to a certain value, due to the higher dye loading the efficiency increases, but after this limit the performance drops due to series resistance and the less efficient light capture. Currently the most common and performing cell architecture is based on a 10 μm-thick photoanode, with porosity ranging between 50-60% and particle size of about 20 nm [12]. The technological evolution of this component then involves different options. One is the application of a so-called "blocking layer", a thin and compact oxide layer (generally TiO_2) deposited between the substrate and the mesoporous film, aimed at improving their adhesion and reducing the back transfer reaction with the FTO surface [12,18]. An over layer, defined scattering layer", is commonly deposited upon the mesoporous one, with the function of increasing the optical light pathway into the photoanode, for maximizing its interaction with the dye. An additional standard layer optimization involves the treatment in a $TiCl_4$ diluted solution (40-50 mM), followed by firing. Through this procedure the film is covered with a thin layer of TiO_2 small nanoparticles, which was demonstrated to increase the dye adsorption and limit the recombination phenomena [12]. These modifications have become a standard to obtain good device performance.

1.4.1 Research trends in DSC photoanodes

Nowadays, the research to improve photoanode performance is still active and is based on three main approaches [42]:

- TiO_2 chemical modification;
- alternative photoanode materials;
- morphological optimization of the semiconductor layer.

TiO_2 chemical modification

One of the major limitation of TiO_2-based photanodes is the relatively slow electron diffusion through the nanocrystalline layer. It was in fact demonstrated that electron transport is slowed down by subsequent trapping and de-trapping between different electronic states. In order to overcome this limitation, and improve TiO_2 performance, different approaches have been considered [12,46]. In particular, the production of composite systems, core-shell structure or element doping have been studied. Eguchi et al. [47] studied the TiO_2-Nb_2O_5 composite with different compositions. The FF resulted to increase with the Nb_2O_5 content due to reduced recombination phenomena. Also Voc increased, thanks to the second oxide higher band gap energy (Eg). Jsc was instead reduced for the lower surface area of Nb_2O_5. The TiO_2-ZrO_2 composite was studied by Kitiyann et al. obtaining a relevant increase in efficiency despite the decay in FF [48]. The configuration reported confines the electron in the TiO_2 core of the system, thus reducing the recombination reactions. Palomares et al. [49] tested different materials as shells for DSC obtaining the best performance with Al_2O_3. Over a certain shell thickness however, the performance dropped due to an excessive surface area reduction limiting dye adsorption. The opposite behavior was observed with MgO, which favored an increase in the surface area an then in Jsc [50]. The results obtained with several TiO_2 modifications are summarized in Table I.

Table I. DSC performance with modified TiO_2, data referring to pure TiO_2 are reported in brackets.

Approach	Composition	V_{OC} (mV)	FF	J_{SC} (mA/cm^2)	η (%)
Core / Shell	TiO_2- ZrO_2[49]	675 (735)	0.60 (0.75)	9.1 (9.1)	3.6 (3.7)
	TiO_2/Nb_2O_5[50]	732 (659)	0.56 (0.51)	11.4 (10.2)	4.7 (3.5)
	TiO_2/SiO_2[49]	710 (735)	0.58 (0.55)	10.6 (9.1)	4.4 (3.7)
	TiO_2/Al_2O_3[49]	760 (735)	0.61 (0.55)	12.1 (9.1)	5.6 (3.7)
	TiO_2/MgO[52]	720 (640)	0.54 (0.47)	11.7 (10.2)	4.5 (3.1)
	TiO_2/ZnO[53]	620 (490)	0.52 (0.40)	11.7 (13.2)	4.5 (3.3)
Composite	95TiO_2-05ZrO_2[48]	670 (710)	0.72 (0.68)	11.2 (10.1)	5.8 (4.6)
	80TiO_2-20Nb_2O_5[47]	645 (600)	0.42 (0.29)	6.83 (7.89)	1.9 (1.4)
Doping	TiO_2:0.1% Nb[42]	841 (777)	0.69 (0.54)	3.1 (2.2)	1.8 (1.0)
	99TiO_2-1Zr[51]	715 (700)	0.69 (0.64)	16.5 (15.6)	8.1 (7.0)

The last approach listed in Table I involves the doping of TiO_2 lattice. In this context Durr and co-workers [51] substituted Ti^{4+} with Zr^{4+} ions, observing that ZrO_2 segregation did not occur up to a 2 mol.% concentration of Zr. Doped-TiO_2 cells showed a 15% increase in efficiency compared to the reference TiO_2 sample. The same trend was obtained using Nb_2O_5 [42]. At last, common to all the reported studies is the doped layers dye uptake increase, with a consequent Jsc enhancement. This is mainly related to the doping process, carried out by powder chemical synthesis, during which the dopant ions in TiO_2 lattice generally promote a contraction of the final particle size compared to pure TiO_2, thus increasing the surface area.

Alternative photoanode materials

As extensively treated in section 1.3, the operating mechanism of DSCs is based on the spontaneous dissociation of the photogenerated exciton. This process could be only possible if the dye LUMO is located at higher energy than the CB of photoanode material. Otherwise, the electron transfer does not occur and there is no current generation. In addition, charge separation is entropycally favoured by the higher density of state in the CB of a crystal (as the photoanode material) rather than in an organic dye molecular orbital. Therefore, the correct CB position is a fundamental requisite for a material to be a candidate photoanode. The band gap energy (Eg) is another determining factor. A large value of Eg, in fact, means a high energy difference with the electrolyte potential, with a positive impact on the Voc. In addition, a large Voc helps in preventing recombination phenomena [42]. The selection of an alternative photoanode material therefore requires a deep comprehension of its electronic properties. Figure 1.13 reports the schematization of the most common photoanode materials energy levels.

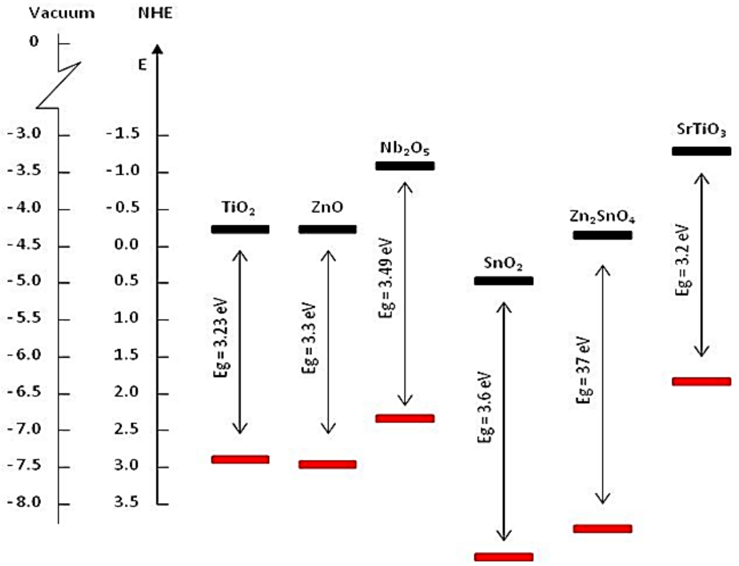

Figure 1.13. Most common anode materials bang gap energy and CB level.

Several materials have been tested as possible photoanodes. ZnO was one of the first compounds employed in sensitization studies with organic dyes [54,55]. Its electronic structure is quite similar to TiO_2, with Eg of 3.37 and a Fermi level located at -4.45 V. The most important ZnO limitation is its low compatibility with the common Ru-based dyes, due to their acidic nature that causes a rapid desorption and a relevant performance reduction. Moreover, dye molecules form aggregates on ZnO surface, compromising charge separation and collection [56]. Finally, the relatively low value of ZnO dielectric constant (8 vs 30-170 of TiO_2) may limit the exciton separation efficiency, causing a reduction in the performance. In conclusion, ZnO was also considered for the simplicity of producing several different morphologies, however it did not reach the stability and the performance of TiO_2 layers [42].

Nb_2O_5 has a wider band gap than TiO_2; for this reason it increases the cell Voc. However, the overall performance is affected by the oxide crystal structure, that limits the dye loaded amount and then the efficiency [57].

The same positive effect on Voc is expected considering SnO_2, due to its high band gap. However this material suffers from different drawbacks when used in DSCs [58,59]. First, more rapid recombination phenomena occur due to the electron diffusion coefficient up to 100 time higher than the TiO_2 one. In addition the negative shift of the conduction band may reduce and limit the electron generation and transfer. Finally, the low isoelectric point of the material (4-5) inhibits the adsorption of dyes with acidic character. A possible solution to overcome this limitation is the application of passive layer upon the SnO_2 one. Using MgO for example, the performance of a SnO_2-based cell registered a 7.02% efficiency [59].

Finally, also ternary oxides have been tested as possible TiO_2 substitutes. The first was $SrTiO_3$, having properties (as Eg and band position) similar to the ones of TiO_2 [60]. However, the efficiency was found to be still low due to the oxide structure: the basic (001) plane is in fact exposed and its nature causes problems with acidic dyes, as reported for ZnO. Lastly, Zn_2SnO_4 showed interesting characteristics, such as a maximum efficiency of 3.8% (comparable to ZnO based cells) and a good stability in acidic conditions [61]. However its main limitation is linked to the low efficiency of electron transfer and transport.

Morphological and topographical layer optimization.

Mesoporous films made of randomly oriented nanoparticles represent the paradigm of photoanodes for DSCs. When designing and producing this kind of photoelectrodes, the primary challenge is to obtain a well-dispersed, thick and crack free layer, in order to maximize its contribution to the overall cell performance. From the early development of DSCs up to now this film structure has been mainly produced by screen-printing constantly giving the best results. However, a variety of microstructures have been tested so far, basically motivated by the assumption that this common 3D structure provides a complicated pathway for electron transport, thus increasing the probability of charge recombination. In this context one dimensional (1D) morphologies are considered possible alternatives, theoretically providing direct pathways for charge transport. Hence, the research has been devoted to 1D architectures as nanotubes, nanowires, nanorods, etc. [62-70]. However, despite partially solving the afore-mentioned issues, these systems suffered from common limitations as the reduced surface area, affecting the dye loading and Jsc. Another problem is the opacity of some of these layers, that therefore requires back-side illumination. On the other hand, different 3D nanoparticles structures exhibited good potentialities, even improving the charge transport efficiency. Among them, the most relevant results were obtained using a film composed of octahedron-like TiO_2 single crystals. This system recorded an efficiency of 10.2% compared to the 9.6% obtained by the common nanoparticle based electrode. Promising results were also obtained using mesoporous anatase single crystals. The most important aspect was the low temperature production (150°C) [71]. Finally, a network made of TiO_2 nanorods showed good performance (light scattering, porosity and charge transfer) when used in conjunction with a solid hole transport material (HTM) [72]. Working on TiO_2 morphology represents the most exploited way to improve the photoanode properties but also the optimization of its topography, if well-designed, can positively affect the DSC operation. In particular, a TiO_2 structure composed by ordered and spatially separated rods (or cylinders), produced by photolithography, showed positive effects on the cell current density and FF providing clear evidence that the contact area between the semiconductor oxide-based electrode and the sensitizer plays an important role on the DSC efficiency [73].

Based on these final evidences, this PhD work was mainly oriented to the production of 3D engineered photoanodes, composed by a mesoporous layer film covered with 3D structures, able to increase DSC performance.

References

[1] Solar Generation 6 “EPIA – European Photovoltaic Industry Association, 2011”.

[2] U.S. Energy Information Administration, “Annual Energy Outlook 20017”.

[3] J. Wu, Z. Lan, J. Lin, M. Huang, Y. Huang, L. Fan, G. Luo, *Electrolyte in Dye-Sensitized Solar Cells*, Chemical Reviews, 2015, 115, 2136-2173.

[4] L. M. Gonçalves, V. de Zea Bermudez, H. A. Ribeiro, A. M. Mendes, *Dye-Sensitized solar cells: a safe bet for the future*, Energy & Environmental Science, 2008, 1, 655-667.

[5] T. Markvart, L. Castañer, *Solar Cells: Materials, Manufacture and Operation*, Elsevier Edition, 2005.

[6] S. Mathew, A. Yella, P. Gao, R. Humpry-Baker, B. F. E. Curchod, N. Ashari-Astani, I. Tavernelli, U. Rothlisberger, Md. K. Nazeeruddin, M. Grätzel, *Dye-Sensitized solar cells with 13% efficiency achieved through the molecular engineering of porphyrin sensitizers*, Nature Chemistry, 2014, 6, 242-247.

[7] https://www.nrel.gov/pv/assets/images/efficiency-chart.png

[8] H. M. Upadhyaya, S. Senthilarasu, M. H. Hsu, D. K. Kumar, *Recent progress and the status of dye-sensitized solar cell (DSSC) technology with state-of-the-art conversion efficiency*, Solar Energy Materials & Solar Cells, 2013, 119, 291-295.

[9] V. Sugathan, E. John, K. Sudhakar, *Recent improvements in dye sensitized solar cells: A review*, Renewable and Sustainable Energy Reviews, 2015, 52, 54-64.

[10] M. Ye, X. Wen, M. Wang, J. Iocozzia, N. Zhang, C. Li, Z. Lin, *Recent advances in dye-sensitized solar cells: prom photoanode, sensitizers and electrolytes to counter-electrode*, Materials Today, 2015, 18, 155-162.

[11] K. Kalyanasundaram, *Dye-Sensitized Solar Cells*, 2010 (First Edition), EPFL Press Lausanne (Switzerland).

[12] A. Hagfeldt, G. Boschloo, L. Sun, L. Kloo, H. Pettersson, *Dye-Sensitized Solar Cells*, Chemical Reviews, 2010, 110, 6595-6663.

[13] www.Dyesol.com.

[14] A. Sangiorgi, R. Bendoni, N. Sangiorgi, A. Sanson, B. Ballarin, *Optimized* TiO_2 *blocking layer for dye-sensitized solar cells*, Ceramics International, 2014, 40, 10727-10735.

[15] H. J. Snaith, *Estimating the maximum attainable efficiency in Dye-Sensitized Solar Cells*, Advanced Functional Materials, 2010, 20, 13-19.

[16] B. E. Hardin, H. J. Snaith, M. D. McGehee, *The renaissance of dye-sensitized solar cells*, Nature Photonics, 2012, 6, 162-169.

[17] M. Grätzel*, Dye-sensitized solar cells*, Journal of Photochemistry and Photobiology C: Photochemistry Reviews, 2003, 4, 145-153.

[18] P. J. Cameron, L. M. Peter, *Characterization of titanium dioxide blocking layers in dye-sensitized nanocrystalline solar cells*, Journal of Physical Chemistry B., 2003, 107, 14394-14400.

[19] A. Jena, S. P. Mohanty, P. Kumar, J. Naduvth, V. Gondane, P. Lekha, J. Das, H. K. Narula, S. Mallick, P. Bhargava, *Dye Sensitized Solar Cells: a Review*, Transactions of the Indian Ceramic Society, 2012, 71:1, 1-16.

[20] C. P. Cho, H. Y. Wu, C. C. Lin, *Impacts of sputter-deposited platinum thickness on the performance of dye-sensitized solar cells*, Electrochimica Acta, 2003, 107, 488-493.

[21] G. Syrrokostas, A. Siokou, G. Leftheriotis, P. Yianoulis, *Degradation mechanisms of Pt counter electrodes for dye-sensitized solar cells*, Solar Energy Materials and Solar Cells, 2012, 103, 119-127.

[22] J. G. Nam, Y. J. Park, B. S. Kim, J. S. Lee, *Enhancement of efficiency of dye-sensitized solar cell by utilizing carbon nanotube counter electrode*, Scripta Materialia, 2010, 62, 148-154.

[23] E. Ramasamy, W. J. Lee, D. Y. Lee, J. S. Song, *Spray coated multi-wall carbon nanotube counter electrode for tri-iodide reduction in dye-sensitized solar cells*, Electrochemistry Communications, 2008, 10, 1087-1089.

[24] S. Yun, A. Hagfeldt, T. Ma, *Pt-free counter electrode for Dye-Sensitized Solar Cells with high efficiency*, Advanced Materials, 2014, 26, 6210-6237.

[25] J. Theerthagiri, A. R. Senthil, J. Madhavan, T. Maiyalagan, *Recent progress in non-platinum counter electrode materials for Dye-Sensitized Solar Cells*, ChemElectroChem, 2015, 2, 928-945.

[26] S. Thomas, T. G. Deepak, G. S. Anjusree, T. A. Arun, S. V. Nair, A. S. Nair, *A review on counter electrode materials in dye-sensitized solar cells*, Journal of Materials Chemistry A, 2014, 2, 4474-4490.

[27] X. Zheng, J. Guo, Y. Shi, F. Xiong, W. H. Zhang, T. Ma, C. Li, *Low-cost and high-performance CoMoS4 and NiMoS4 counter electrodes for dye-sensitized solar cells*, Chemical Communications, 2013, 49, 9645-9647.

[28] M. Wu, X. Lin, Y. Wang, L. Wang, W. Guo, D. Qi, X. Peng, A. Hagfeldt, M. Grätzel, T. Ma, *Economical Pt-free catalysts for counter-electrodes of dye-sensitized solar cells*, Journal of American Chemical Society, 2012, 134, 3419-3428.

[29] S. Yun, L. Wang, W. Guo, T. Ma, *Non-Pt counter electrode catalysts using tantalum oxide for low-cost dye-sensitized solar cells*, Electrochemistry Communications, 2012, 24, 69-73.

[30] C. Bu, Q. Tai, Y. Liu, S. Guo, X. Zhao, *A transparent and stable polypyrrole counter electrode for dye-sensitized solar cell,* Journal of Power Source, 2013, 221, 78-83.

[31] X. Zhang, S. Wang, S. Lu, J. Su, T. He, *Influence of doping anions on structure and properties of electro-polymerized polypyrrole counter electrodes for use in dye-sensitized solar cells*, Journal of Power Source, 2014, 246, 491-498.

[32] L. Y. Chang, C. T. Li, Y. Y. Li, C. P. Lee, M. H. Yeh, K. C. Ho, J. J. Lin, *Morphological influence of polypyrrole nanoparticles on the performance of dye-sensitized solar cells*, Electrochimica Acta, 2015, 155, 263-271.

[33] D. K. Hwang, D. Song, S. S. Jeon, T. H. Han, Y. S. Kang, S. S. Im, *Ultrathin polypyrrole nanosheets doped with HCl as counter electrodes in dye-sensitized solar cells*, Journal of Materials Chemistry A, 2014, 2, 859-865.

[34] J. Wu, Y. Li, Q. Tang, G. Yue, K. Lin, M. Huang, L. Meng, *Bifacial dye-sensitized solar cells: a strategy to enhance overall efficiency based on transparent polyaniline electrode*, Scientific Reports, 2014, 4, 4028.

[35] P. Chawla, M. Tripathi, *Novel improvements in the sensitizers of dye-sensitized solar cells for enhancement in efficiency-a review*, International Journal of Energy Research, 2015, 39, 1579-1596.

[36] M. R. Narayan, *Review: Dye sensitized solar cells based on natural photosensitizers*, Renewable and Sustainable Reviews, 2012, 16, 208-215.

[37] F. Bella, C. Gerbaldi, C. Barolo, M. Grätzel, *Aqueous dye-sensitized solar cells*, Chemical Society Reviews, 2015, 44, 3431-3473.

[38] A. F. Nogueira, C. Longo, M. A. De Paoli*, Polymers in dye sensitized solar cells: overview and perspectives*, Coordination Chemistry Reviews, 2004, 248, 1455-1468.

[39] M. Wang, N. Chamberland, L. Breau, J-E. Moser, R. H-Baker, B. Marsan, S. M. Zakeeruddin, M. Grätzel, *An organic redox electrolyte to rival triiodide/iodide in dye-sensitized solar cells*, Nature Chemistry, 2010, 2, 385-389.

[40] L. Li, X. Yang, J. Zhao, J. Gao, A. Hagfeldt, L. Sun, *Efficient organic dye sensitized solar cells based on modified sulfide/polysulfide electrolyte*, Journal of Materials Chemistry, 2011, 21, 5573-5575.

[41] M. Pelaez, N. T. Nolam, S. C. Pillai, M. K. Seery, P. Falaras, A. G. Kontos, P. S. M. Dunlop, J. W. J. Hamilton, J. A. Byrne, K. O'Shea, M. H. Entezari, D. D. Dionysiou, *A review on the visible light active titanium dioxide photocatalysts for environmental applications*, Applied Catalysis B: Environmental, 2012, 125, 331-349.

[42] R. Jose, V. Thavasi, S. Ramakrishma, *Metal oxide for dye-sensitized solar cells*, Journal of the American Ceramic Society, 2009, 92, 289-301.

[43] B. O'Regan, M. Grätzel, *A low cost, high efficiency solar cell based on dye sensitized colloidal* TiO_2 *films*, Nature, 1991, 353, 737-740.

[44] M. Grätzel, *Solar energy conversion by dye-sensitized photovoltaic cells*, Inorganic Chemistry, 2005, 44, 6841-6851.

[45] Y. Bai, I. Mora-Sero, F. De Angelis, J. Bisquert, P. Wang, *Titanium dioxide nanomaterials for photovoltaic applications*, Chemical Reviews, 2014, 114, 10095-10130.

[46] R. Beranek, *(Photo)electrochemical methods for the determination of the band edge positions of* TiO_2*-based nanomaterials*, Advances in Physical Chemistry, 2011.

[47] K. Eguchi, H. Koga, K. Sekizawa, K. Sasaki, *Nb2O5-based composite electrodes for dye-sensitized solar cells*, Journal of the Ceramic Society of Japan, 2000, 108, 1067-1071.

[48] A. Kitiyanan, S. Yoshikawa, *The use of* ZrO_2 *mixed* TiO_2 *nanostructures as efficient dye-sensitized solar cell's electrodes*, Materials Letter, 2005, 59, 4038-4040.

[49] E. Palomares, J. N. Clifford, S. A. Haque, T. Lutz, J. R. Durrant, *Control of charge recombination dynamics in dye sensitized solar cells by the use of conformally deposited metal oxide blocking layers*, Journal of the American Ceramic Society, 2003, 125, 475-482.

[50] A. Zaban, S. G. Chen, S. Chappel, B. A. Gregg, *Bilayer nanoporous electrodes for dye sensitized solar cells*, Chemical Communications (Cambridge), 2000, 22, 2231-2232.

[51] M. Durr, S. Rosselli, A. Yasuda, G. Nelles, *Band-gap engineering of metal oxides for dye-sensitized solar cells*, The Journal of Physical Chemistry B, 2006, 110B, 21899-21902.

[52] H. Jung, J. K. Lee, M. Nastasi, S. W. Lee, J. Y. Kim, J. S. Park, K. S. Hong, H. Shin, *Preparation of nanoporous MgO-coated TiO2 nanoparticles and their application to the electrode of dye-sensitized solar cells*, Langmuir, 2005, 21, 10332-10335.

[53] S. Roh, R. S. Mane, S. Min, W. Lee, C. D. Lokhande, S. Han, *Achievement of 4.51% conversion efficiency using ZnO recombination barrier layer in TiO2 based dye-sensitized solar cells*, Applied Physics Letters, 2006, 89, 253512.

[54] G. Redmond, D. Fitzmaurice, M. Grätzel, *Visible light sensitization by Cis-Bis (thiocyanato) Bis (2,2'-bipyridyl-4.4'-dicarboxylato) Ruthenium(II) of transparent nanocrystalline ZnO films prepared by sol-gel techniques*, Chemistry of Materials, 1994, 6, 686-691.

[55] H. Rensmo, K. Keis, H. Lindstrom, S. Sodergren, A. Solbrand, A. Hagfeldt, S. E. Lindquist, L. N. Wang, M. Muhammed, *High light-to-energy conversion efficiencies for solar cells based on nanostructured ZnO electrodes*, The Journal of Physical Chemistry B, 1997, 101, 2598-2601.

[56] K. Keis, J. Lindgren, S. E. Lindquist, A. Hagfeldt, *Studies of the adsorption process of Ru complexes in nanoporous ZnO electrodes*, Langmuir, 2000, 16, 4688-4694.

[57] P. Guo, M. A. Aegerter, *Ru(II) sensitized Nb2O5 solar cell made by the sol gel process*, Thin Solid Films, 1999, 351, 290-294.

[58] E. Ramasamy, J. Lee, *Ordered mesoporous SnO2-based photoanodes for high performance dye-sensitized solar cells*, The Journal of Physical Chemistry C, 2010, 114, 22032-22037.

[59] M. K. I. Senevirathna, P. K. D. D. P. Pitigala, E. V. A. Premalal, K. Tennakone, G. R. A. Kumara, A. Konno, *Stability of the SnO2/MgO dye-sensitized photoelectrochemical solar cell*, Solar Energy Materials and Solar Cells, 2007, 91, 544-547.

[60] P. Balaya, J. Jamnik, J. Fleig, J. Maier, *Mesoscopic electrical conduction in nanocrystalline SrTiO3*, Applied Physics Letters, 2006, 88.

[61] B. Tan, E. Toman, Y. Li, Y. Wu, *Zinc stannate (Zn2SnO4) dye sensitized solar cells*, Journal of the American Ceramic Society, 2007, 129, 4162-4163.

[62] J. M. Macak, H. Tsuchiya, A. Ghicov, P. Schmuki, *Dye-sensitized anodic* TiO_2 *nanotubes*, Electrochemistry communications, 2005, 7, 1133-1137.

[63] J. H. Park, T. W. Lee, M. G. Kang, *Growth, detachment and transfer of highly-ordered TiO2 nanotube arrays: use in dye-sensitized solar cells*, Chemical Communications, 2008, 25, 2867-2869.

[64] K. Zhu, N. R. Neale, A. Miedaner, A. J. Frank, *Enhanced charge-collection efficiencies and light scattering in dye-sensitized solar cells using oriented TiO_2 nanotube arrays*, Nano Letters, 2007, 7, 69-74.

[65] J. Jiu, S. Isoda, F. Wang, M. Adachi, *Dye-sensitized solar cells based on a single-crystalline TiO_2 nanorod film*, The Journal of Physical Chemistry B, 2006, 110, 2087-2092.

[66] B. Liu, E. S. Aydil, *Growth of oriented single-crystalline rutile TiO2 nanorods on transparent conducting substrates for dye-sensitized solar cells*, Journal of the American Chemical Society, 2009, 131, 3985-3990.

[67] H. Wang, M. Liu, M. Zhang, P. Wang, H. Miura, Y. Cheng, J. Bell, *Kinetics of electron recombination of dye-sensitized solar cells based on TiO_2 nanorods arrays sensitized with different dyes*, Physical Chemistry Chemical Physics, 2011, 13, 28, 17359-17366.

[68] E. Enache-Pommer, J. E. Boercker, E. S. Aydil, *Electron transport and recombination in polycrystalline TiO2 nanowire dye-sensitized solar cells*, Applied Physics Letters, 2007, 91, 123116.

[69] X. Feng, K. Zhu, A. J. Frank, C. A. Grimes, T. E. Mallouk, *Rapid charge transport in dye-sensitized solar cells made from vertically aligned single-crystal rutile TiO_2 nanowires*, Angewandte Chemie International Edition, 2012, 51, 2727-2730.

[70] J. Y. Liao, B. X. Lei, H. Y. Chen, D. B. Kuang, C. Y. Su, *Oriented hierarchical single crystalline anatase TiO_2 nanowire arrays on Ti-foil substrate for efficient flexible dye-sensitized solar cells*, Energy and Environmental Science, 2012, 5, 5750-5757.

[71] J. W. Shiu, C. M. Lan, Y. C. Chang, H. P. Wu, W. K. Huang, E. W. Diau, *Size-controlled anatase titania single crystals with octahedron-like morphology for dye-sensitized solar cells*, ACS Nano, 2012, 6, 10862-10873.

[72] E. J. W. Crossland, N. Noel, V. Sivaram, T. Leijtens, J. Alexander-Webber, H. J. Snaith, *Mesoporous TiO_2 single crystals delivering enhanced mobility and optoelectronic device performance*, Nature, 2013, 495, 215-219.

[73] T. H. Meen, C. J. Huang, Y. W. Chen, L. W. Ji, C. C. Diao, H. H. Chung, *Study of different* TiO_2 *electrode structures on Dye-Sensitized Solar Cell*, Key Engineering Materials, 2008, 368-372, 1716-1719.

Chapter 2

Unconventional DSCs production processes

2.1 Screen-printing as traditional deposition process for mesoporous layers

Screen-printing (SP) is a widespread deposition technique (Figure 2.1), of particular importance at the industrial scale. It covers an extended range of different applications, from textile to electronics.

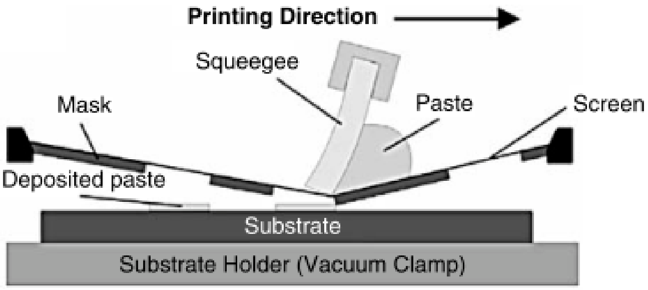

Figure 2.1. Basic principles of the screen printing process

In the ceramic field, SP finds different uses such as in tiles decoration, due to its simplicity, the high printing definition and the low-cost. For advanced ceramics it is the reference technique for the realization of thick films for electronics, sensors and also DSCs [1,2].

The SP enables the homogeneous and uniform deposition of a material in a layered structure onto a substrate. The material to be deposited is converted into a paste with the right viscosity that consists of organics, (polymers, solvents, etc.) and the homogeneously inorganic solid particles of interest. During screen printing the paste is moved over the screen by a squeegee, while the screen is pressed on the substrate and the paste is forced through the meshes. The screen mesh is masked except for the part reproducing the desired pattern. The printed paste adheres to the surface of the substrate and after removing the screen the paste forms an even and continuous film on the substrate.

In most technical applications a precise layer thickness is important. Therefore, the squeegee pressure, the viscosity and the solids content of the paste must be exactly controlled. Screen printed structures are in most cases functional layers, meaning that their technical and physical properties control the application potential. There are applications that require dense layer structures (e.g. SOFC electrolytes) and there is sometimes a need to produce porous layers as in the case of DSCs. However, the screen-printing process have some important limitations [3]; it is a laborious multistep process, so it takes a lot of time to set up a deposition in particular with complex designs. As is the case with similar method of printing, SP requires a series of different step optimization before the actual printing. Therefore, preparation times could be particularly long, especially for high quality applications like the solar cells one.

Moreover, SP is not environmentally friendly. It is still a reality that screen printing wastes a lot of water to clean the screens, which may not seem like much at first, but considering an industrial production, this aspect become even more alarming.

2.2 Wet-powder spraying as screen-printing alternative

Wet-powder spraying (WPS) is normally used as a collective term for some similar coating methods also familiar as “suspension spraying”. In the WPS process a suspension, consisting of a powder and a carrier liquid-binder mixture is sprayed onto a substrate using a modified airbrush [4].

A spraying gun (or a spray valve) is used and is often mounted on a robotic system that allows complex 2D or 3D movements where flat, tubular, and three-dimensional parts can be coated. WPS allows the processing of a wide variety of ceramic, metallic, and composite powders. The particle diameter can change from nanometer scale to about 100 μm [5].

To obtain reproducible and high-quality coatings advanced control of the key parameters is necessary. The latter are the nozzle size of the gun, the distance between nozzle tip and the substrate surface, the viscosity and the feed rate of the suspension, the operating pressure and the operating speed between the gun and the structural parts.

The function of the spray apparatus (Figure 2.2) is the uniform distribution of the powder suspension onto the substrate surface.

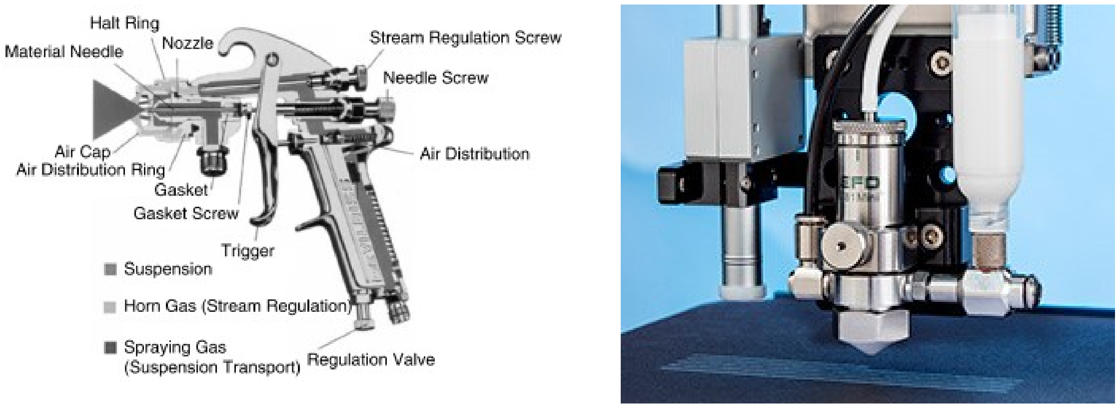

Figure 2.2. Schematic drawing of a suspension spray gun [4] and a spray valve (right) [6]

For this purpose, the suspension is atomized with the aid of pressurized air (sometimes N_2 gas). The droplets formed in the micrometer range and containing solid powder particles fly in the spraying direction and hit the part surface where they are further scattered. As in all spraying processes, WPS efficiency is also dependent on the overspray. Changing the spray pattern and the deposition rate are easily accessible parameters to influence the amount of overspray which represents the quantity of material deposited outside the desired area.

Besides the spray parameters, the quality of the deposited layer is influenced by the suspension properties [7,8], in particular drying behavior and viscosity. For an efficient deposition procedure, the suspension has to be optimized for each powder, taking also into account the surface properties of the substrate for the suspension–surface interactions. Besides the carrier liquid, typical spraying suspensions contain a solid powder (ceramic or metallic), a dissolved binder and other agents able to influence viscosity, zeta potential, pH value, and drying behavior. High-quality deposition results can be obtained by correctly dispersing powder particles in the liquid phase. Sometimes, however, WPS suspensions cannot be produced in a fully stabilized manner. In this case, the particles tend to agglomerate and sedimentation takes place over time. Spraying of such unstabilized suspensions is done while stirring continuously to avoid agglomeration and sedimentation. As previously mentioned, reproducible and high-quality films are strictly dependent from the control of the key process parameters. In particular, the ones that mainly affect the deposition quality are: nozzle size, spraying distance, speed and pressure, and they will be deeply described in Chapter 3. In nearly all cases, the sprayed layer has to be sintered to obtain sufficient mechanical properties or to achieve the intended function. Before the sintering procedure starts a drying step is necessary. During drying the solvent or the water evaporates and only the binder and additives (if present) remain in the porous powder layer. Sintering in most cases takes place in a solid-state below the melting temperature of the powder particles [9,10].

WPS has become a well-established processing method in the last decade, in particular to deposit layers on planar and complex-shaped 3D parts. Although completely dense layers are achieved by this method, the main applications are related to porous layers and structures. WPS represents also a convenient method for the large area production of solar cells [11]; it allows the deposition on arbitrary substrate materials and geometries [12] of fluids with different rheology in a simple and low-cost way, minimizing the material waste. For these reasons, in this PhD thesis WPS was considered as a promising alternative technique to the traditional SP for the deposition of the mesoporous TiO_2 layer that will act as basement for the 3D structures realized through additive manufacturing techniques. Its applicability to meet this purpose is even more concrete considering that during the process, films are formed by depositing small aerosolized droplets and consequently numerous voids are formed. These pores represent the ideal situation for a performing DSC photoanode which will be able to host higher amount of dye and thus potentially improve the cell performance.

2.3 Photolitography as conventional deposition process for complex patterns

Lithography literally means writing on stones. In the case of semiconductor, lithography (called photolithography, PLy) stones are silicon wafers and the patterns are written with a light sensitive polymer called a photoresist. PLy (Figure 2.3) is a subtractive process which creates high-resolution patterns (feature sizes < 1 μm): (i) the material is deposited in a blanket layer, typically using a vacuum-based process such as chemical vapour deposition or physical vapour deposition; (ii) the substrate is then coated with a photoresist; (iii) the photoresist is exposed using a photolithographic system through a mask; (iv) the photoresist is developed to remove the resist from mask-determined regions of the substrate; (v) the deposited film is etched using a wet chemical or dry (i.e. plasma-based) etch; the deposited film is only etched from regions where the photoresist has previously been developed; (vi) the remaining resist is stripped away to expose the patterned film, and finally, (vii) the substrate is cleaned to remove residue from the resist and etch process.

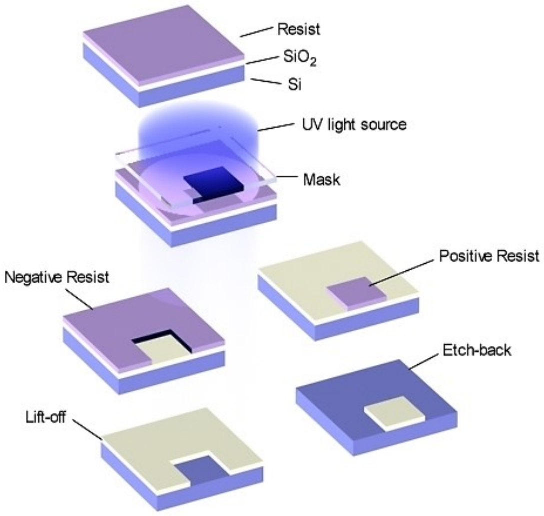

Figure 2.3. Schematization of the main processes composing photolithography [13]

This seven-step process is repeated several times with multiple masking and etch steps to create sophisticated patterns. From this description emerges that the Ply process is time consuming, labour intensive, and expensive. Since the solvent used in the etching process is corrosive, the choice of substrate is limited. Moreover, the Ply process generates high volumes of hazardous waste which are environmentally destructive and for which treatment is becoming prohibitively expensive. For these reasons, the Ply replacement becomes an interesting issue able to lead to substantial cost reduction for the realization of complex semiconductor systems and in a more eco-friendly approach. In the last decade, the printed electronics industry and researchers have focused their consideration on the promising additive manufacturing (AM) methods (accurately described in the next section), paying particular attention to the inkjet printing technique. In this thesis, the latter will be considered as powerful deposition method to create high-aspect ratio 3D semiconductor structures on mesoporous sprayed layer; however, inkjet is a quite complex technique that needs an exact long-lasting optimization process of the ink formulation, of the printhead parameters and finally of the ink-substrate interactions. Thus, even the less sensitive robocasting (specifically micro-extrusion) technique that belongs to the AM extrusion grouping, will be simultaneously investigated aiming to obtain, coarser three-dimensional structures which however should be able to demonstrate the positive effect of a photoanode engineering.

2.4 Additive Manufacturing

Different from conventional materials removal method, additive manufacturing (AM) is based on a novel material incremental manufacturing philosophy. The AM process (Figure 2.4) begins with a 3D model of the object, usually created by computer-aided design (CAD) software or a scan of an existing artifact. Specialized software slices this model into cross-sectional layers, creating a computer file that is sent to the AM machine. The latter than creates the object by forming each layer via the selective placement (or forming) of material.

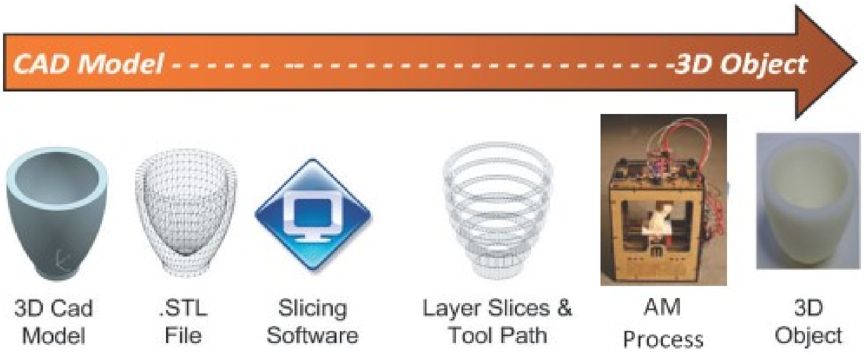

Figure 2.4. Generalized AM process [14]

In this section, the development history of AM technology is briefly introduced and the general advantages and drawbacks of the principal AM techniques are also presented.

2.4.1 AM technology: definitions and development history

The additive manufacturing (AM) term indicates a class of technologies. AM is, therefore, also called solid freeform fabrication, or recently, “3D printing”; the latter has been used to denominate the AM technology and is widely used in the news media, which is hopefully considered as the driver of a “third industrial revolution” due to its potential capability to revolutionize the way used to fabricate almost everything [15].

Since the first technique for AM became available in the late 1980s and was used to fabricate models and prototypes [16,17], AM technology has experienced more than 20 years of development and today is one of the rapidly developing advanced manufacturing techniques in the world. The main AM advantages over the traditional manufacturing processes are reported in Table I.

Table I. Summary of the main AM advantages compared with traditional manufacturing processes

Allows to create complex shapes (e.g. curving internal cooling channels)
Improves the product customizability without additional costs
Reduces material waste and scrap
Limits the amount of energy used
More efficient use of raw materials
Minimal harmful (e.g. etching) chemicals needed
Environmentally friendly product designs possible
Changes to design streamlined
Carbon footprint of a given product reduced (via reduced need for global shipping)

Different to the material removal method in conventional machining processes, AM is based on a completely contrary discipline [17] that implies layer-by-layer shaping and consolidation of feedstock to arbitrary configurations. A wide range of feedstock can be applied for AM technology, from the low melting point polymer materials to the high melting point metals and ceramics. Meanwhile, different forms of materials, including liquid, powder, solid, wire, etc., are feasible for AM. Based on the similar processing philosophy, the established AM techniques are versatile. An overview of the different processes is given in Table II.

Table II. Overview of various additive manufacturing processes and relative acronyms

Process	Description	Typical AM techniques	Materials
Photopolymer vat	Liquid photopolymer is selectively cured using a light source.	SLA, 2PP	Photo-curable polymers
Material extrusion	Material selectively is dispensed through a nozzle or extruder.	FDM, Robocasting	Polymers, ceramics, metals
Powder bed fusion	Thermal energy selectively fuses regions of powder bed material	SLS, SLM, EBM, SMS	Polymers, metals, ceramics
Material jetting	Droplets of build material are selectively deposited layer by layer	DoD Inkjet printing, PJT	Polymers, metals, ceramics
Binder jetting	Liquid bonding ink is selectively spread to join solid powder material	3DP	Polymers, metals, ceramics

The processes considered and briefly discussed in this section are stereolithography (SLA) [18], fused deposition modeling (FDM) [19] and selective laser sintering (SLS) [20]. Then, Robocasting and Material Jetting (MJ) will be deeply described in separated sections since they were used during the thesis activity to produce the 3D-enginnered DSC photoanodes.

2.4.2 Stereolitography (SLA)

Stereolithography, initially developed by 3D Systems Inc. in 1986, was the first and most widely applied rapid prototyping process. In essence, it is a liquid-based process that consists of the curing or solidification of a photosensitive polymer when an ultraviolet laser makes contact with the resin. The thickness of each layer as well as its resolution depend on the equipment used. A platform is created to hold the piece and to support any overhanging structures. An ultraviolet laser applied to the resin initiates solidification at specific locations of each layer. When the single layer is produced the platform is lowered. The key components of a stereolithography machine are shown in Figure 2.5.

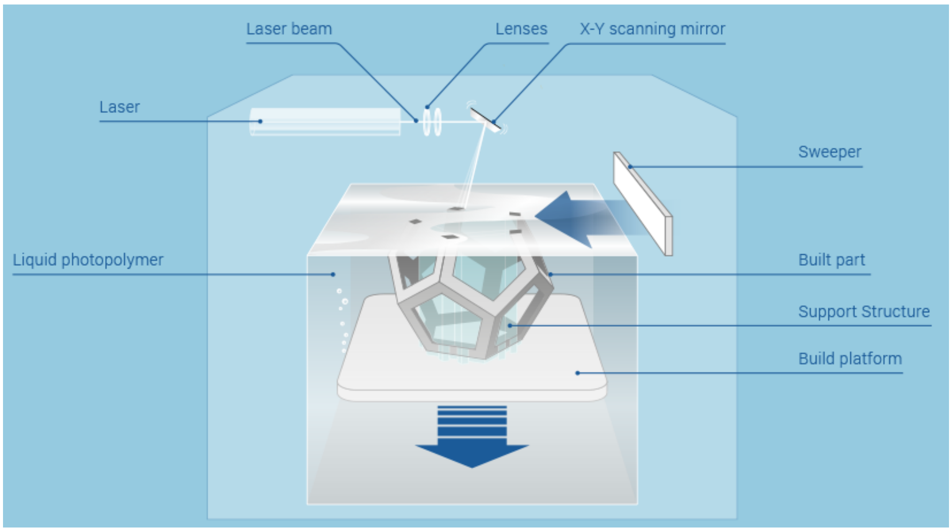

Figure 2.5. SLA apparatus scheme [21]

The basic principle governing the stereolithography process is photopolymerization [22]. This is essentially a process where a liquid monomer or a polymer is converted into a solid by the application of ultraviolet light. The ultraviolet light acts as a catalyst for the reactions. It has also been found to be applicable for powders of a ceramic suspended in a liquid [23-25].

A significant error that often occurs during SLA processing is over-curing, which tends to take place in overhanging parts because of the lack of fusion with a bottom layer. Because the resin used is a high-viscosity liquid, the thickness of the layer is often the only variable and errors can occur during position control. Other errors can occur when the part or component must have a specific surface finish that under normal circumstances would be provided manually [26]. Finally, the resins and other additives employed in this technique are toxic and during the curing process they tend to generate vapors that are potentially dangerous.

2.4.3 Fused Deposition Modeling (FDM)

In this technique, a thermoplastic material is easily extruded from a movable FDM head and then deposited in thin layers onto a substrate. Basically, the material is heated to one degree above its melting point so that it solidifies immediately following extrusion and also easily cold welds to the previous layers. The materials that have been used for this AM technique include acrylonitrile butadiene styrene (ABS), polylactic acid (PLA), and even ceramics. In recent years, machines having two nozzles have been developed; one nozzle is for the part material and the other for the support material, which is often less expensive and can be easily removed from the parent without impairing its surface finish [27].

A schematic of the basic fused deposition modeling process is shown in Figure 2.6. The advantages of this process include: no chemical post-processing and less expensive equipment than SLA for the absence of a curing step.

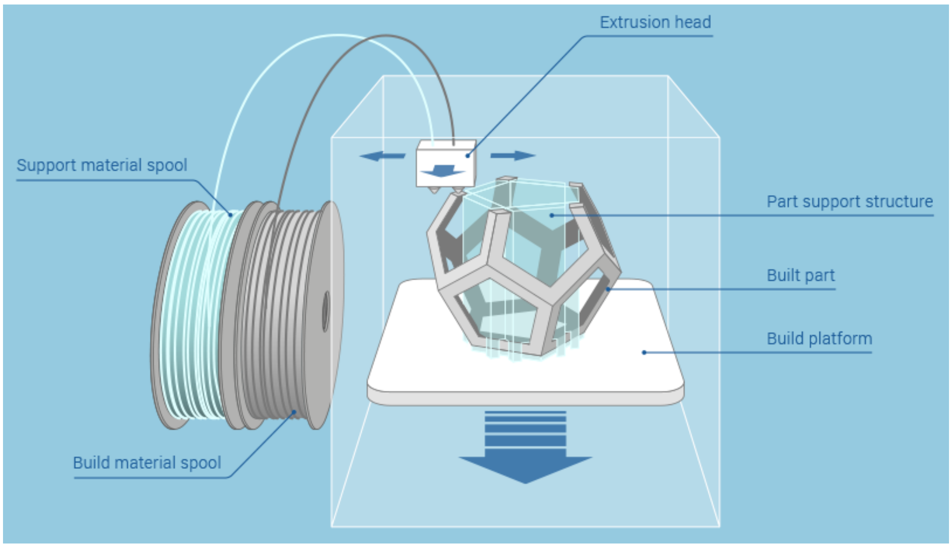

Figure 2.6. FDM apparatus scheme [21]

The noticeable disadvantages of this technique are: longer build-up time, sometimes requiring days to build complex parts, delamination arising as a direct consequence of fluctuation in temperature and finally, low resolution of the Z-axis compared to other AM techniques.

2.4.4 Selective Laser Sintering (SLS) [28]

This AM process uses a high-power laser to fuse small particles of the build material (metal, ceramic, polymer, glass, or any material that can be easily pulverized). The fabrication powder bed is heated to just below the melting point of the material with the primary objective of minimizing thermal distortion and to concurrently facilitate fusion to the previous layer. Each layer is then drawn on the powder bed using a laser to sinter the material. The sintered material forms the part while the un-sintered powder remains in place to support the structure; it can be cleaned away and recycled once the part of interest has been built.

This process of selective laser sintering offers the freedom to build complex parts that are often more durable and provide better functionality compared to other existing and preferentially used AM processes. Further, in this process no post-curing is required, and the build time is noticeably fast. Its disadvantages are basically: (i) accuracy is strictly limited by the size of the particles of the chosen material; (ii) oxidation must be avoided by executing the process in an inert atmosphere or vacuum; (iii) the process must occur at a constant temperature near the melting point of the chosen material.

2.4.5 3D printing (3DP)

The patent for three-dimensional printing (also known as binder jetting, BJ) was deposited in 1993 [29]. In BJ, a water-based liquid binder is applied in a jet onto a starch-based powder to print the data from a CAD drawing. The powder particles lie on a powder bed and become glued to each other when the binder is applied. Following the sequential application of layers, the unbound powders are carefully removed (Figure 2.7).

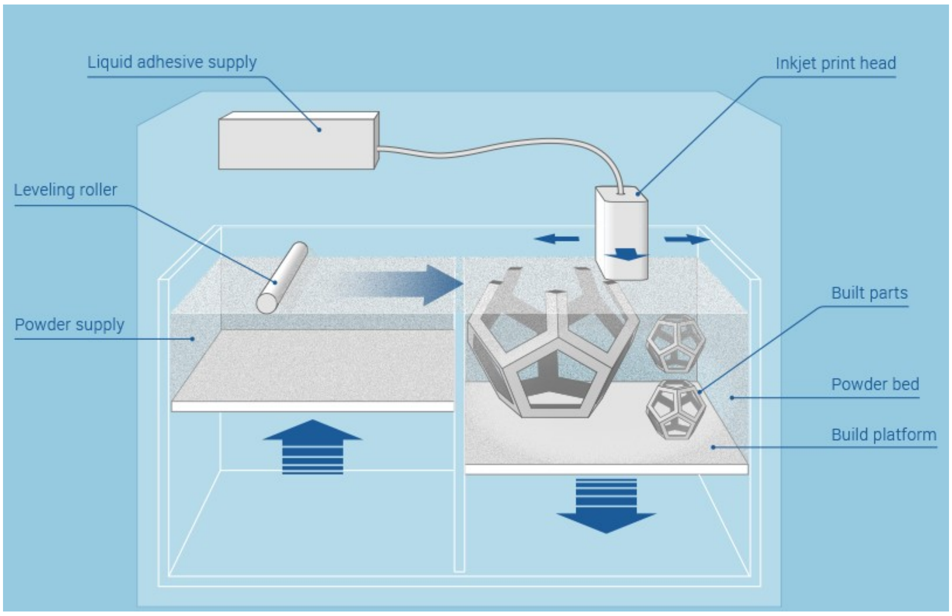

Figure 2.7. BJ apparatus scheme [21]

The process is referred to as 3DP primarily because of its similarity to the inkjet printing process used for two-dimensional printing on paper. Initially, the technique was used for handling a variety of polymeric materials [30,31], however, it can also be applied for the production of metal and ceramic parts. Various materials can be dispensed using different print heads, thus 3D printing can be used to exercise control over the local material composition. This technique can be used to create a part of any geometry from the material chosen while concurrently facilitating the controlling of both the microstructure and resultant properties of the part being produced. In essence, the 3DP technique offers the advantage of speedy fabrication and reduced material cost [32]. Currently, it can easily be considered to be one of the fastest growing of all of the commercially available AM processes.

2.4.6 Robocasting (Micro-extrusion)

Robocasting (or Direct Ink Writing, DIW) [33] is an extrusion-based AM technique which has being developed for the freeform fabrication of ceramics and composites [34,35]. Robocasting layerwise deposits ceramic slurries through an orifice. The process (Figure 2.8) is mainly based on the extrusion of highly loaded ceramic slurries that are typically composed by 50-65 vol.% ceramic powder and 35-50 vol.% of a volatile solvent (usually water).

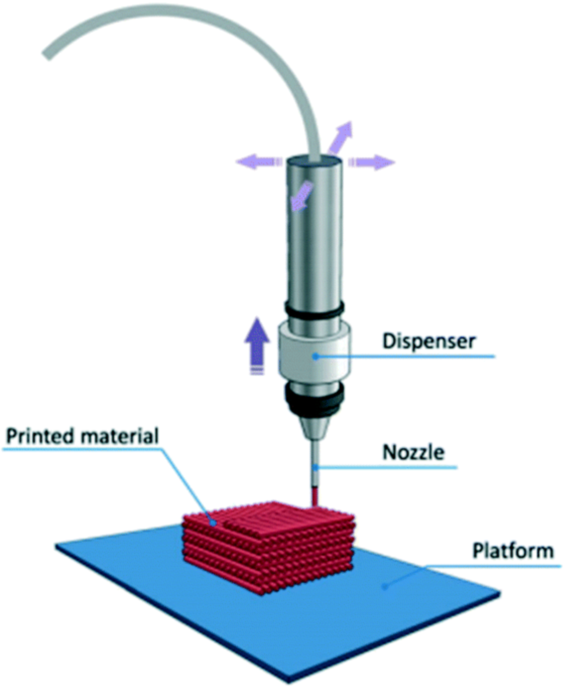

Figure 2.8. Micro-extrusion process scheme [36]

In general, a robocasting slurry must meet three criteria: 1) it must be pseudoplastic enough to flow through a small orifice at modest shear rates; 2) it must set-up into a nonflowable mass upon dispensing; and 3) it must be able to "accept" multiple layers without defects to form a uniform mass. Probably the most unique and interesting aspect of robocasting is the process by which the flowing pseudoplastic slurry transforms into a solid-like mass after deposition. In contrast to gel casting, robocasting does not require organic polymerization reactions or solidification of a polymeric melt for the solid transformation; it relies on the rheology of the deposited slurry and on partial drying of the individual layers. Typical ceramic powder slurries have an average particle size on the order of several microns and possess a relatively monosized distribution. Ceramic powders with this characteristic, typically pack into a consolidated structure that is approximately 65% of the theoretical density. For robocasting, the character of flowable slurries with solids loadings just below the consolidated density is crucially important. At low solids loadings, dispersed slurries have very low viscosity and are Newtonian. Around 40 volume percent solids, the slurries begin to show pseudoplastic shear-thinning behavior even though the viscosity is still relatively low. As the solids content approaches 60 volume percent, inter-particle interactions and inter-particle collisions become dominant; viscosity begins to increase appreciably and the rheological behavior becomes highly shear-thinning. At approximately 63 volume percent solids, particle mobility becomes restricted and the slurry locks up into a dilatant mass. Therefore, it is desirable to realize slurries that have solids loadings approaching the dilatant transition so that with minimal drying, a robocasted layer becomes structurally sound and a foundation upon which more layers may be deposited. Typically, parts are built upon a platform heated between 30 and 60°C to assist the pseudoplastic to dilatant transition. If the drying rate is too slow, the pseudoplastic to dilatant transition is delayed and accumulated weight from several layers eventually surpasses the yield stress of the pseudoplastic layers. This condition can induce slumping and the creation of non-uniform walls. Conversely, if the drying rate is too fast, warping, cracking, and delamination may occur.

In general, proper robocasting requires a synergistic control of the: 1) solids percentages in the ceramic powder slurry, 2) viscosity and rheology of the slurry, 3) dispensing rate of the slurry through the orifice, and 4) drying kinetics of the dispensed bead of slurry. When a proper balance of these variables is achieved, robocasting can be used to make intricate ceramic bodies, like in this case where 3D elongated structures are needed to improve the DSCs efficiency.

2.4.7 Material Jetting (MJ)

Material jetting is the use of inkjet printing or similar techniques to deposit, differently from 3DP, droplets of build material (normally a mixture of powder, solvents and organic additives) that are selectively dispensed through a nozzle to build up a 3D layer-by-layer structure (Figure 2.9).

In material jetting processes, liquid material (in the form of a droplet) is jetted and often turns into solid after deposition via cooling (e.g. vitrification), chemical changes (e.g. polymer cross-linking) or solvent evaporation [37].

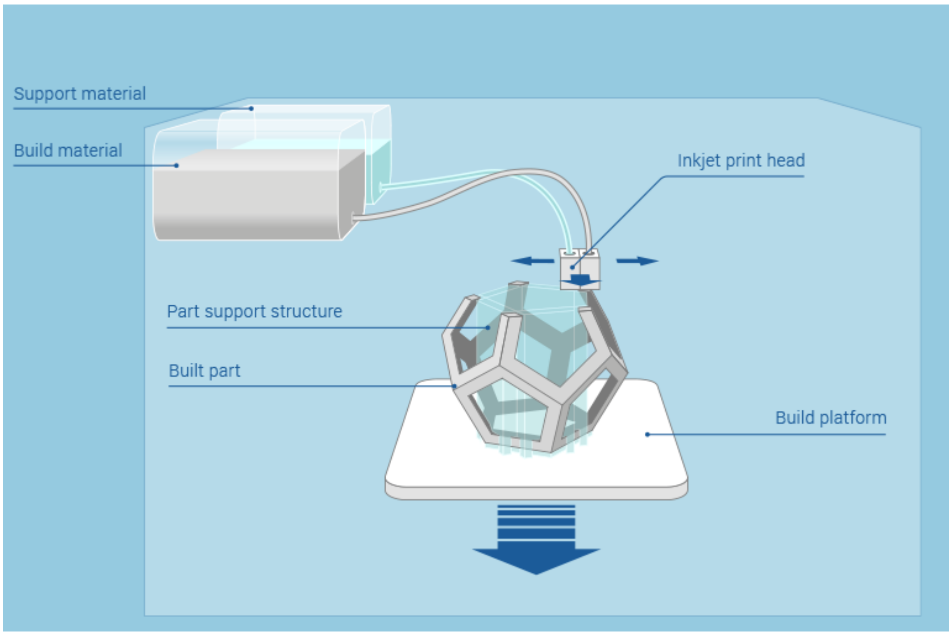

Figure 2.9. MJ apparatus scheme [21]

Two different modes are predominantly used for material droplet creation, namely Drop on Demand (DoD) and continuous inkjet (CIJ). Generally, CIJ systems use fluids with lower viscosity and are mostly used where printing speed is an important matter. In contrast, DoD is used where smaller drop size, and higher accuracy is required and it has fewer limitations on ink properties as compared with CIJ [38]. In DoD printing, droplets are formed only when individual pressure pulses in the nozzle cause the fluid to be expelled; these pressure pulses are created at specific times by thermal, piezoelectric or other actuators [39]. In the current DoD printing industry, thermal and piezoelectric actuator technologies dominate. Thermal DoD is restricted to water as a solvent and thus places strict limitations on the number of materials that can be processed [40]. Piezoelectric actuators rely on the deformation of a piezoelectric element to reduce the volume of the liquid reservoir, which causes a droplet to be ejected. Piezoelectric DoD printhead, like the ones used in this thesis, is an appropriate apparatus for a variety of solvents and thus suited for different applications ranging from piezoelectric devices to printed electronics and solar cells [41]. In these fields, inkjet provides a noncontact, maskless additive patterning process, which can be used to deposit and pattern a very wide range of materials. With the high costs of materials used in traditional lithographic patterning processes, the reduced material waste and scalability to large-scale manufacturing are further attractive attributes.

There are several significant phenomena which affect the quality of the inkjet process such as the ink/substrate interaction and above all, the chemical-physical ink properties. In the next paragraphs, these aspects will be deepened focusing the attention on the ones that will be mainly considered and evaluated during the PhD experimental activities.

2.5 Ceramic inkjet inks

At the simplest level, the components within an inkjet fluid fulfill one of two primary roles. Firstly there are components such as solvent, humectants and surfactants which are present to enable the production of a stable ink capable of being jetted reliably under standard operating conditions, and secondly there are the components chosen for their effective function in the substrate (such as dyes, pigments and functional materials) The reliability and printing characteristics of any ink are not inherent properties of the formulation but are strongly dependent on the print-head and process architecture, thus requiring a holistic approach to ink design.

The printing process consists of three distinct stages: drop generation, drop flight and drop impact. Each of these operations imposes physical limitations on both the ink formulation and the printing process. The important physical properties of a fluid forming droplets are its density (ρ), surface tension (σ) and viscosity (η), commonly grouped in dimensionless form using the Weber number (We) and Reynolds number (Re).

In formulating a robust inkjet ink, consideration must be given to:

- ink chemistry: ability to formulate stable inks which do not detrimentally interact with the materials of construction of the inkjet printer;
- ink flow within the print-head: ability to wet the different surfaces throughout the head allowing ease of priming and avoidance of bubble nucleation;
- creation of a stable meniscus at the nozzle: dependent upon whether a wetting or non-wetting faceplate technology is used, and on the need to balance the surface tension forces of the meniscus and gravity feed from the ink reservoir;

- droplet formation and jet stability: stable droplet formation with control of ligament length, drop size, satellite formation and directionality;
- drop–substrate interaction: interaction of the droplet with the surface to enable the correct spatial deposition of the functional material in the x, y and z planes;
- in-use functionality: dried printed ink must have the correct topology, morphology and physical properties to perform the required function.

Carefully attention is paid at all times to filtration and degassing of the ink as these steps help successful ink formulation. Inkjet inks can be classified into five generic classes based upon the nature of the solvent or carrier vehicle: (i) water-based or aqueous inks (which often contain up to 20% of organic co-solvents), (ii) oil-based inks (glycols and hydrocarbons), (iii) phase-change or hot-melt inks (wax), (iv) UV-curable inks and, (v) solvent-based inks (methyl ethyl ketone, alcohols).The main advantage that the water-based inks developed over the last 30 years have over the other ones is that they contain little or no volatile organic components making this approach more eco-friendly. This is the reason why, water-based inkjet ceramic inks have been considered in this thesis and accordingly described in detail below.

The deposition of ceramic inks [42] is a still growing field. However, several difficulties are connected with their composition and application. The first is the rheology of ceramic suspensions. The viscosity of suspensions in general shows a shear dependency that depends on the volume fraction of solids, the particles size and shape, and the interparticle forces. During the printing process high shear rates are exerted on the ink, so the shear dependent viscosity of an ink may strongly influence the inkjet pumping mechanism. Secondly, due to the high density of ceramics, the chemical stability of ceramic inks is an important issue. The sedimentation of solids within the print head leads in fact to clogging of the nozzles.

The rheology of suspensions generally differs from fluids as a result of the hydrodynamic forces acting on the particles. Since flows in print heads are in the range of low Reynolds numbers (deeply discussed later in the text), the velocity profile within (circular) capillaries is parabolic. At very low shear rates, particles in a chemically stable suspension approximately follow the layers of constant velocities, as indicated in Figure 2.10.

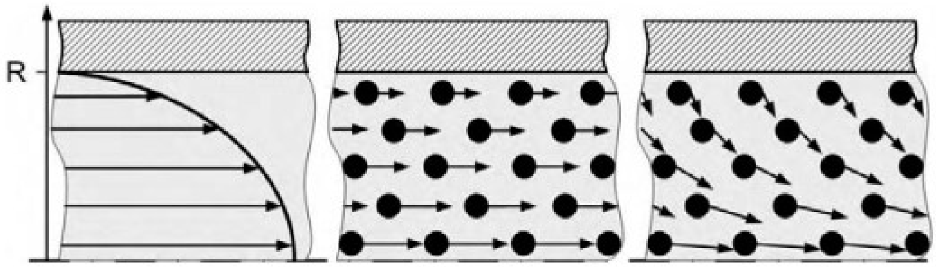

Figure 2.10. Laminar flow within a capillary: hydrodynamic forces drive particles out of layers of constant velocity [42]

But at higher shear rates hydrodynamic forces drive particles out of layers of constant velocity. The competition between hydrodynamic forces that distort the microstructure of the suspension and drive particles together, and the Brownian motion and repulsive interparticle forces keeping particles apart, leads to a shear dependency of the viscosity of suspensions. These effects depend on the effective volume fraction of solids in the suspension, the particles interaction (the strength of repulsion), and their size, shape and surface properties. During the fire pulses high shear rates are exerted on the ink, about $\gamma = 10^4 - 10^6$ 1/s, depending on whether single or multiple pulses are used to generate drops. It is difficult to conduct experiments at such high shear rates, so the studies on the viscosity of suspensions have been commonly obtained at lower shear rates using traditional rheometers. The qualitative behavior of the viscosity of suspensions over a large range of share rates is represented in Figure 2.11.

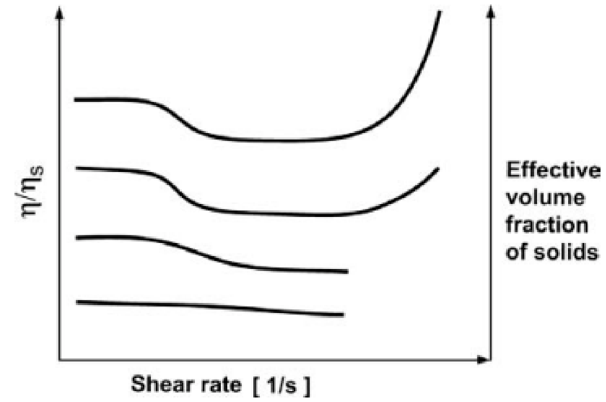

Figure 2.11. Qualitative sketch of the shear dependency of the viscosity of stable suspensions over a large range of shear rates [42]

The most evident feature in Figure 2.11 is the onset of shear thickening at high shear rate. The instantaneous increase in viscosity of an ink during the fire pulse in fact would easily defeat the inkjet pumping mechanism. The rheological parameters, described in detail in the next paragraph, that qualify a fluid to be applicable to inkjet printing are the viscosity (η) and surface tension (σ) (typical ranges are η = 6 to 20 mPas and σ = 25 to 35 mN/m). Depending on the specific printhead, these ranges may change. In the case of suspensions, the effective volume fraction of solids and the particle properties enter as additional parameters; i.e., if the volume fraction of solids of a chemically stable suspension is continuously increased where the low shear viscosity (and surface tension) are kept within the acceptable ranges, the inkjet process begins to get unstable at some point and finally fails (nozzle clogged).

It is difficult to prove that shear thickening is the origin of this instability of the printing process, but results obtained for colloidal suspensions suggest that shear thickening may well occur at the high shear rates exerted during the fire pulse. Shear thickening only appears if particles are permitted to approach sufficiently close. Dispersants or surfactants added to inks may help to postpone or even suppress the onset of shear thickening [43]. Shear thickening in colloidal suspensions is governed by particle size and surface roughness, in addition to the effective volume fraction of solids [44]. A different important issue in this context is the chemical stability of ceramic suspensions, which is indispensable for inkjet printing. Due to the high density of ceramics, a stable suspension also requires that the particles not be too large (conventionally smaller than 2 μm). To summarize, problems with the application of ceramic suspensions with inkjet printers grow with the (effective) volume fraction of solids and the size of particles.

2.5.1 Surface tension and viscosity [45]

Two physical properties of the liquid dominate the behavior of the jets and drops involved in inkjet printing: surface tension and viscosity.

The surface tension of a liquid reflects the fact that atoms or molecules at a free surface have a higher energy than those in the bulk. There is a cost in terms of energy in creating new surface area. For a free droplet of liquid the shape with the lowest surface area, and therefore the lowest surface energy, is a sphere, and in the absence of other influences is the shape which a free drop will adopt. If the liquid is in contact with a solid surface, for example after it has been printed onto a substrate, then not only the energy of its free surface is considered (which is usually in contact with air) but also the energy of the interface between the liquid and the solid substrate. In that case (and if, as in inkjet printing, the effect of gravity is negligible), the equilibrium shape of the drop becomes a spherical cap. The surface tension in a liquid causes a force to act in the plane of the free surface perpendicularly to a free edge in that surface, which can be measured directly by various experimental methods. The force is proportional to the length of the edge, and the surface tension (σ) can therefore be defined as the force per unit length (N/m).

Most liquids of practical interest for inkjet deposition have σ of the order of tens of mN/m. For pure water at 20°C, σ = 72.5 mN/m, while for many organic liquids (which have smaller intermolecular energies than water), lies in the range from 20 to 40 mN/m. The tendency of a liquid to form the shape with the lowest total energy, which in the case of a free drop causes it to become a sphere, is crucial to the processes of inkjet printing. A continuous stream of liquid emerging from a circular nozzle will initially be cylindrical, but that shape is unstable. Under the action of surface tension, disturbances in the shape of the cylinder will grow and the jet will eventually break up into a series of spherical drops. This is the classical Rayleigh–Plateau instability. The forces which resist the contraction of a liquid jet through the action of surface tension have two origins: the inertia of the liquid and its viscosity. Inertial forces are proportional to ink density and the rate of change of velocity. Viscous forces arise from the interactions between molecules of the liquid and act between regions of liquid moving relative to each other. The simple term viscosity, without further qualification, usually means the dynamic viscosity. The SI unit for dynamic viscosity is the Pascal second (Pas). Water has a viscosity of almost exactly 1 mPa s at 20°C, while fluids which are used in inkjet printing typically have viscosities in the range from ∼2 to ∼50 mPas. The viscosities of most liquids fall rapidly with increasing temperature, and this is often exploited in inkjet printing.

2.5.2 Ohnesorge and other dimensionless numbers [45]

Surface tension, inertia and viscosity play key roles in the formation and behavior of liquid jets and drops. Two important dimensionless numbers can be used to characterize their relative importance: the Reynolds number (Re) and Weber number (We). The Re number represents the ratio between inertial and viscous forces in a moving fluid, and is defined by:

$$Re = \frac{\rho d V}{\eta}$$

where ρ is the density of the fluid, V is its velocity, η is its viscosity and d is a characteristic length, typically the diameter of the jet, nozzle or drop. We number depends on the ratio between inertia and surface tension:

$$We = \frac{\rho d V^2}{\sigma}$$

where σ is the surface tension.

The influence of velocity in these two dimensionless groups can be removed by combining them to form a further group, the Ohnesorge number (Oh), defined by:

$$Oh = \frac{\sqrt{We}}{Re} = \frac{\eta}{\sqrt{\sigma \rho d}}$$

The value of the Oh number (independent of the fluid V), which reflects only the physical properties of the liquid and the size scale of the jet or drop, turns out to be closely related to the behavior of a jet emerging from a nozzle, and thus to the conditions in DoD printing. If Oh number is too high (Oh ≥1), then viscous forces will prevent the separation of a drop, while if it is too low (Oh ≤ 0.1), the jet will form a large number of satellite droplets (that are additional drops resulting from the collapse of the liquid column by surface tension). Satisfactory performance of a fluid in DoD inkjet printing thus requires an appropriate combination of physical properties, which will also depend on the droplet size and velocity (through the value of the Re or We numbers) as shown in Figure 2.12 [46,47].

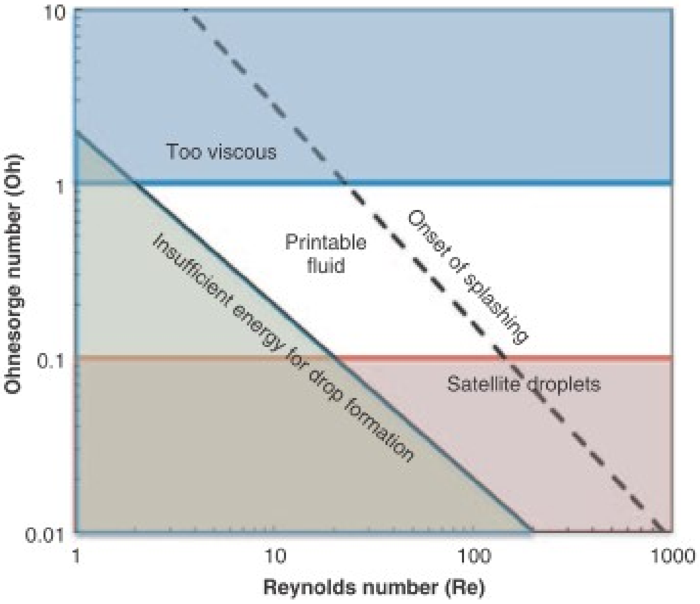

Figure 2.12. Schematic diagram showing the operating regime for stable operation of DoD inkjet printing, in terms of the Oh and Re numbers [45]

Sometimes the symbol Z is used as the inverse of the Ohnesorge number (Z = 1/Oh). The range over which liquids can be printed is often quoted as 10 > Z > 1 [48], although other work has suggested that 14 > Z > 4 may be more appropriate [49]. The ranges of the Ohnesorge number provide some bounds to the 'printability' of the liquid, but other factors must also be considered: the jet must possess enough kinetic energy to be ejected from the nozzle (leading to the solid diagonal line in Figure 2.12), and it is also desirable to avoid splashing of the drop on impact with the substrate (dashed line in Figure 2.12) [46].

2.5.3 Drop-substrate collision

In inkjet printing the final desired image or pattern is a solid object on the substrate. Thus an important stage in the generation of the pattern is the impact of the liquid drop on a substrate and the subsequent phase change that transforms the liquid into a solid. The latter can occur by a number of mechanisms including: solvent evaporation, gelling of a polymer precursor, chemical reaction and so on. In all these cases, solidification occurs post-deposition and the printed pattern must retain some stability in the liquid state prior to solidification. This retention capability is strongly dependent from the capillarity-driven spreading of droplets that can be described by these three concepts: (i) droplet-substrate equilibrium, (ii) contact line motion and (iii) contact angle hysteresis.

When a liquid is put into contact with a solid, the liquid will tend towards an equilibrium shape if no other forces act upon it. This manifest itself in the form of an equilibrium contact angle (θ_{eqm}) that is dependent upon the balance of the three salient surface energies (Figure 2.13): (σ_{LV}) the surface energy between the liquid and the surrounding environment, (σ_{SV}) the surface energy between solid and the surrounding environment and finally (σ_{LS}) the surface energy between the liquid and the solid.

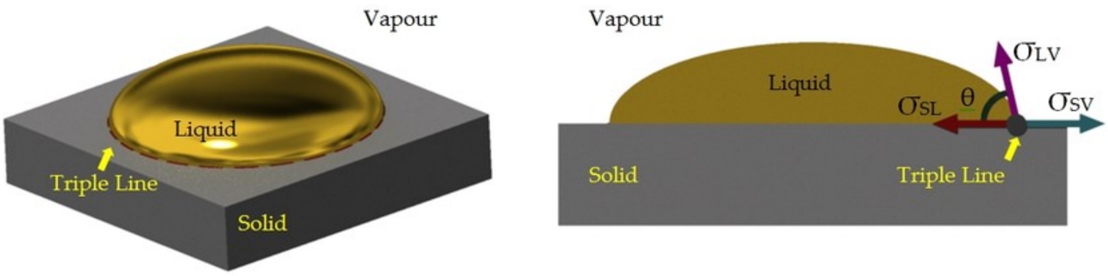

Figure 2.13. Schematic diagram illustrating the truncated sphere geometry adopted by sessile droplets when gravitational forces are not considered. The relevant surface energies and consequent equilibrium contact angle are also illustrated [50]

The balance between these three surface energies and their relation to θ_{eqm} is given by the Young equation:

$$\sigma_{SV} = \sigma_{LS} + \sigma_{LV} cos\theta_{eqm}$$

This equation is valid in the immediate vicinity of the contact line at equilibrium. If gravitational forces are negligible like in the inkjet printing, the liquid profile can be calculated on the assumption that the liquid will tend to minimize surface energy by forming truncated sphere geometries (Figure 2.13). The equilibrium wetting of a droplet on a substrate can be further influenced by the use of heterogeneous and structured substrates. Without a means of supplying additional energy, a droplet on a rough surface will therefore not always form a truncated sphere geometry that would be expected on a smooth surface.

The spontaneous spreading of a liquid upon a substrate entails the redistribution of the liquid volume such that it ends up in equilibrium with the substrate at the equilibrium contact angle. To achieve this, it is necessary to both move the contact line from an initial position and redistribute the liquid volume across the contact area with the substrate [51].

Contact angle hysteresis is caused by an energy barrier inhibiting the movement of the contact line and leads to two contact angles measured on a substrate that are dependent upon the direction of contact line movement: an advancing contact angle and a receding contact angle [51]. There are a number of possible sources for this hysteresis, such as surface roughness and chemical heterogeneity of the substrate, but perhaps the most relevant to inkjet printing is the presence of an additional solid phase at the contact line, such as a powder within the droplet. This presence can introduce either a mechanical barrier to the receding contact line or a change in the surface energy equilibrium in the vicinity of the contact line. If the deposition of solid material at the contact line is great enough, this will lead to the receding contact angle being reduced to zero. This means that the initial equilibrium state of the droplet on the substrate before phase change will control the size of deposit left after evaporation of the carrier solvent has occurred [52].

2.5.4 Droplet evaporation

As already mentioned, in most applications of inkjet printing, it is necessary for the liquid ink to be converted to a solid phase, whether this is by the evaporation of solvent or, by the solidification of wax droplets in the formation of 3D ceramic pre-forms [53]. If the phase change involved in the deposition process takes place over a timescale much greater than deposition, as in the evaporation mechanism, contact line pinning (and, therefore, determination of feature resolution) that occurs will be as a result of contact angle hysteresis. As previously mentioned, the presence of a solid phase within the ink, as in this case with TiO_2 nanoparticles, is the most relevant cause; the TiO_2 can introduce either a mechanical barrier to the receding contact line or a change in the surface energy equilibrium in the contact line vicinity.

Contact line pinning results in the contact line retraction of an evaporating droplet proceeding in a two-stage process [54]. In the first stage, the contact area between droplet and substrate remains constant and the contact angle between droplet and substrate is reduced. This stage continues until the contact angle has been reduced to the receding contact angle, at which point the contact line will retract and the contact area shrinks. These two stages can be repeated several times over the entire retraction process, resulting in the droplet having a series of concentric metastable states as the evaporation proceeds [55].

The mass transport of fluid upon evaporation is proportional to the surface area of the liquid, but in a drop with pinned contact lines the droplet cannot uniformly change volume. The extra volume needed to maintain the mass transport due to evaporation must come from the center of the droplet, and an outward radial flow is induced. This fluid flow possesses a great enough force to overcome gravitational forces acting upon any small suspended particles, and the solid is therefore segregated to the perimeter of the droplet. It has been found that this ‘coffee staining’ effect (Figure 2.14) can be overcome by inducing a Marangoni flow (induced by the temperature gradient caused by evaporation changing the surface tension profile across the droplet) within the droplet towards the center to counteract the flow due to mass transport [56].

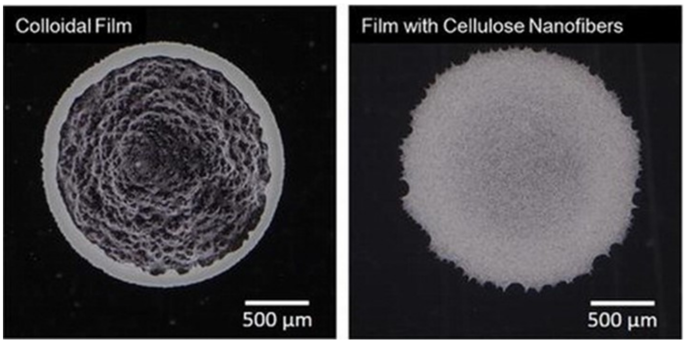

Figure 2.14. Digital camera images of thin films after drying: (left) pronounced coffee stain effect (right) suppressed coffee staining [57]

Solute segregation has also been controlled by the use of binary solvent mixtures [58], where two solvents with a significantly different volatility are used. As the more volatile species will be first to evaporate, the concentration of this species will be reduced at the periphery of the droplet compared to the center due to the differing relative evaporation rates across the droplet. The increased concentration of the volatile species at the center of the droplet will then compensate for the variation in evaporation rate due to the droplet geometry and prevent solute segregation.

Although originally devised for dilute suspensions, previous work has shown that segregation also occurs in more concentrated suspensions [59]. Rather than complete segregation of the solid to the perimeter, a raised ring of material is present at the perimeter. The incomplete segregation is most probably due to both the magnitude of the induced fluid flow not being sufficient to move all the material within the timescale of evaporation, and the solid material being unable to move outside the constraints of the droplet fluid.

Among all the listed techniques, as already mentioned, the WPS, micro-extrusion and DoD inkjet printing will be employed for the production of 3D engineered DSC photoanodes. These unconventional processes are alternatives to traditional techniques used in DSCs and electronics production (e.g. screen-printing and photolitography) due to their advantages such as fully-automation, easy scalability, low costs and reduced environmental impact.

References

[1] M. R. Parikh, W. F. Quilty, K. M. Gardiner, *SPC and setup analysis for screeprinted thick films,* IEEE Electronic Manufacturing Technology Symposium., 1991, 14, 493.

[2] S. Ito, P. Chen, P. Comte, M. Nazeeruddin, P. Liscka, P. Pechy, M. Grätzel, *Fabrication of screen printing pastes from TiO_2 powders for dye-sensitized solar cells,* Progress in Photovoltaics: Research and Applications, 2007, 15, 603-612.

[3] J. R. Groza, J. F. Shackelford, E. J. Lavernia, M. T. Powers, *Materials processing handbook,* CRC Press, Taylor & Francis Group, Boca Raton FL, 2007.

[4] L. Zhao, *Manufacture and characterization of composite graded filter membranes for microfiltration.* Ph.D. thesis; Forschungszentrum Jülich reports, JÜL-4079. 2003.

[5] R. Vaßen, D. Stöver, *Processing and properties of nanophase ceramics*, Journal of Materials Processing Technology, 1999, 92-93, 77-84.

[6] http://www.nordson.com/en/divisions/efd/about-us/news/new-nordson-efd-781mini-spray-valve-uniform-spray-control-in-smaller-form-factor-8-23-16.

[7] S. Baklouti, C. Pagnoux, T. Chartier, J. F. Baumard, *Processing of aqueous α-Al_2O_3, α-SiO_2 and α-SiC suspensions with polyelectrolytes*, Journal of the European Ceramic Society, 1997, 17, 1387-1392.

[8] H. Terayama, K. Okumura, K. Sakai, K. Torigo, K. Esumi, *Aqueous dispersion behavior of drug particles by addition of surfactant and polymer*, Colloids and Surfaces B: Biointerfaces, 2001, 20, 1, 73-77.

[9] K. Darcovich, D. Roussel, F. N. Toll, *Sintering effects related to filtration properties of porous continuously gradient ceramic structures*, Journal of Membrane Science, 2001, 183, 2, 293-303.

[10] M. Stech, P. Reynders, J. Rödel, *Constrained film sintering of nanocrystalline TiO_2*, Journal of the American Ceramic Society, 2000, 83, 8, 1889-1896.

[11] L. La Notte, D. Mineo, G. Polino, G. Susanna, F. Brunetti, T. M. Brown, A. Di Carlo, A. Reale, *Fabrication of Fully-Spray-Processed Organic Photovoltaic Modules by using an Automated Process in Air*, Energy Technology, 2013, 1, 757–762.

[12] A. Abdellah, B. Fabel, P. Lugli, G. Scarpa, *Spray deposition of organic semiconducting thin-films: Towards the fabrication of arbitrary shaped organic electronic devices,* Organic Electronics, 2010, 11, 6, 1031-1038.

[13] https://www2.warwick.ac.uk/services/ris/impactinnovation/impact/photolithography/

[14] T. Campbell, C. Williams, O. Ivanova, B. Garrett, *Could 3D Printing Change the World? Technologies, Potential, and Implications of Additive Manufacturing,* Atlantic Council, Strategic Foresight Report, 2011.

[15] http://www.economist.com/node/21552901.

[16] D. L. Bourell, H. L. Marcus, J. W. Barlow, J. J. Beaman, C. R. Deckard (1991) *Multiple material systems for selective beam sintering*. US Patent 5076869.

[17] C. K. Chua, K. F. Leong, C. S. Lim, *Rapid prototyping: principles and applications*, World Scientific Publishing Company, Singapore, 2003.

[18] A. P. West, S. P. Sambu, D. W. Rosen, *A process planning method for improving build performance in stereolithography*, Computer Aided Design, 2001, 33, 1, 65–79.

[19] R. W. Gray, D. G. Baird, J. H. Bohn, *Effects of processing conditions on short TCLP fiber reinforced FDM parts*, Rapid Prototyping Journal, 1998, 4, 1, 14–25.

[20] D. L. Bourell, H. L. Marcus, J. W. Barlow, J. J. Beaman, *Selective laser sintering of metal and ceramics*, International Journal of Powder Metallurgy, 1992, 28, 4, 369–381.

[21] https://www.additively.com

[22] J. W. Halloran, V. Tomeckova, S. Gentry, *Photo-polymerization of powder suspensions for shaping ceramic materials,* Journal of the European Ceramic Society, 2011, 31, 14, 2613–2619.

[23] D. T. Pham, C. Ji, *Design for stereolithography,* Proceedings of the Institution of Mechanical Engineers, Part C: Journal of Mechanical Engineering Science, 2000, 214, 5, 635–640.

[24] J. S. Yun, T. W. Park, Y. H. Jeong, J. H. Cho, *Development of ceramic-reinforced photopolymers for SLA 3D printing technology,* Applied Physics A, 2016.

[25] P. V. Evdokimov, V. I. Putlyaev, V. M. Ievlev, E. S. Klimashina, T. V. Safronova, *Osteoconductive ceramics with a specified system of interconnected pores based on double calcium alkali metal phosphates,* Doklady Chemistry, 2015, 460, 2, 61-65.

[26] H. Kim, C. Jae Won, R. Wicker, *Scheduling and process planning for multiple material stereolithography,* Rapid Prototyping Journal, 2010, 16, 4, 232–240.

[27] D. T. Pham, R. S. Gault, *A comparison of rapid prototyping technologies*, International Journal of Machine Tools and Manufacture, 1998, 38, 1257–1287.

[28] T. Hwa, L. Hsing,, C. Ming, Y. H. Chuan, *Slurry-based selective laser sintering of polymer-coated ceramic powders to fabricate high strength alumina parts*, Journal of the European Ceramic Society, 2011, 31, 8, 1383–1388.

[29] E. Sachs, M. Cima, J. Cornie, *Three-dimensional printing: rapid tooling and prototypes directly from a CAD model.* CIRP Annals Manufacturing Technology, 1990, 39, 201–204.

[30] K. G. Cooper, *Rapid Prototying Technology: Selection and application*, Marcel Dekker, 2001, New York.

[31] J. Skelton, *Fused deposition modeling. 3D Printers and 3D-Printing Technologies Almanac*, 2008, http://3d-print.blogspot.com/2008.

[32] R. Miller, *Additive manufacturing (3D printing): past, present and future*. Industrial Heating, 2014, May 39–41.

[33] J. Cesarano III, *A review of robocasting technology*, Materials Research Society Symposium Proceedings, 1999, Vol. 542, 133-139.

[34] E. Peng, X. Wei, U. Garbe, D. Yu, B. Edouard, A. Liu, J. Ding, *Robocasting of dense yttria-stabilized zirconia structures,* Journal of Materials Science, 2018, 53, 1, 247-273.

[35] E. Feilden, E. García-Tuñón Blanca, F. Giuliani, E. Saiz, L. Vandeperre, *Robocasting of structural ceramic parts with hydrogel inks,* Journal of the European Ceramic Society, 2016, 36, 10, 2525-2533.

[36] C. Hurt, M. Brandt, S.S. Priya, T. Bhatelia, J. Patel, P.R. Selvakannan, S. Bhargava, *Combining additive manufacturing and catalysis: a review,* Catalysis Science & Technology, 2017, 7, 3421-3439.

[37] K. K. B. Hon, L. Li, I. M. Hutchings, *Direct writing technology-Advances and developments,* Cirp Annuals - Manufacturing Technology, 2008, 57, 601-620.

[38] M. Vaezi, H. Seitz, S. Yang, *A review on 3D micro-additive manufacturing technologies*, The International Journal of Advanced Manufacturing Technology, 2012, 1-34.

[39] I. Gibson, D. W. Rosen, B. Stucker, *Additive Manufacturing Technologies*, Springer, 2010.

[40] B. J de Gans, U. S. Schubert, *Inkjet printing of polymer micro-arrays and libraries: Instrumentation, requirements, and perspectives*, Macromolecular Rapid Communications, 2003, 24, 659-666.

[41] F. C. Krebs, M. Jorgensen, K. Norrman, O. Hagemann, J. Alstrup, T. D. Nielsen, J. Fyenbo, K. Larsen, J. Kristensen, *A complete process for production of flexible large area polymer solar cells entirely using screen printing-first public demonstration*, Solar Energy Materials and Solar Cells, 2009, 93, 4, 422–441.

[42] S. Magdassi, *The chemistry of Inkjet Inks,* World Scientific Publishing Co. Pte. Ltd, 2010.

[43] J. Bergenholtz, J. F. Brady, M. Vicic, *The non-Newtonian rheology of dilute colloidal suspensions*, Journal of Fluid Mechanics, 2002, 456, 239–275.

[44] .E. Smith, C. F. Zukoski, *Flow properties of hard structured particle suspensions,* Journal of Rheology, 2004, 48, 1375–1388.

[45] I. M. Hutchings, G. D. Martin, *Inkjet technology for digital fabrication,* John Wiley & Sons Ltd, 2013.

[46] B. Derby, *Inkjet printing of functional and structural materials: fluid property requirements, feature stability, and resolution*. Annual Review of Materials Research, 2010, 40, 395–414.

[47] G. R. McKinley, M. Renardy, *Wolfgang von Ohnesorge. Physics of Fluids,* 2011, 23, 127101.

[48] N. Reis, B. Derby, *Ink jet deposition of ceramic suspensions: modelling and experiments of droplet formation,* Materials Research Society Symposium Proceedings, 2000, 625, 117–122.

[49] D. Jang, D. Kim, J. Moon, *Influence of fluid physical properties on inkjet printability*, Langmuir, 2009, 25, 2629–2635.

[50] M. Caccia, A. Camarano, D. Sergi, A. Ortona, J. Narciso, *Chapter 5: Wetting and Navier-Stokes Equation - The Manufacture of Composite Materials,* Wetting and Wettability, InTech, 2015.

[51] P. G. de Gennes, *Wetting – statics and dynamics. Reviews of Modern Physics*, 1985, 57, 3, 827–863.

[52] P. C. Duineveld, *The stability of inkjet-printed lines of liquid with zero receding contact angle on a homogeneous substrate*, Journal of Fluid Mechanics, 2003, 477, 175–200.

[53] K. A. M. Seerden, N. Reis, J. R. G. Evans, *Inkjet printing of wax-based alumina suspensions*, Journal of the American Ceramic Society, 2001, 84, 11, 2514–2520.

[54] M. E. R. Shanahan, C. Bourges, *Effects of evaporation on contact angles on polymer surfaces,* International Journal of Adhesion and Adhesives, 1994, 14, 3, 201–205.

[55] R. D. Deegan, O. Bakajin, T. F. Dupont, G. Huber, S. R. Nagel, T. A. Witten, *Capillary flow as the cause of ring stains from dried liquid drops,* Nature, 1997, 389, 6653, 827–829.

[56] H. Hu, R. G. Larson, *Marangoni effect reverses coffee-ring depositions*, Journal of Physical Chemistry B, 2006, 110, 14, 7090–7094.

[57] Y. Ooi, I. Hanasaki, D. Mizimura, Y. Matsuda, *Suppressing the coffee-ring effect of colloidal droplets by dispersed cellulose nanofibers*, Science and Technology of Advanced Materials, 2017, 18, 1, 316-324.

[58] B. J de Gans, U. S. Schubert, *Inkjet printing of well-defined polymer dots and arrays*, Langmuir, 2004, 20, 18, 7789–7793.

[59] R. Noguera, M. Lejeune, T. Chartier, *3D fine scale ceramic components formed by inkjet prototyping process,* Journal of the European Ceramic Society, 2005, 25, 12, 2055–2059.

Chapter 3

Experimental

3.1 Introduction

In the present study, three different deposition technologies, installed in an all-in-one machine (XCEL, AUR'EL Automation s.p.a., Italy) were investigated: wet-powder spraying (WPS), micro-extrusion and inkjet printing. Each of these technique demands suitable suspensions or inks aiming to realize homogeneous mesoporous films and/or high-aspect ratio three dimensional structures. Thus, three different approaches were mainly used:

- for WPS, a commercial TiO_2 colloidal aqueous suspension was selected as starting product. The effect of different dilution ratios on its stability was evaluated and the impact of some specific deposition parameters on the sprayed films morphologies and transparencies was inspected;
- for the micro-extrusion process, aqueous powder-based inks were initially formulated. The effects of different amounts and compositions of cellulosic blends on the rheological properties of TiO_2 inks were investigated. Afterwards, their formulation procedure was modified introducing a commercial TiO_2 suspension, similar to the spray one, as matrix for the inks. Also in this case the binder impact on the rheological properties of TiO_2 inks was analysed; finally, the optimized ink was used to produce micro-pillars;
- for the inkjet printing, aqueous powder-based inks were primarily formulated considering the effect of pH, dispersant, binder and surfactant on their stability, viscosity, surface tension, etc. Moreover, the effect of different milling processes on the powder particles was investigated. Concluding, a stable organic solvent-based ink containing higher TiO_2 powder amount was prepared and its applicability demonstrated by ejecting it through an industrial printhead specifically designed for ceramic inks.

In this section, the components and the initial processing of the inks are presented. The employed deposition equipment, the main process parameters, the production of films and 3D structures are also introduced. Finally, the prototypes production and the principal characterization techniques considered in these studies are reported.

3.2 XCEL apparatus

XCEL (Figure 3.1) is a stand-alone multi-head work cell for, in this configuration, WPS, micro-extrusion and ink jet printing.

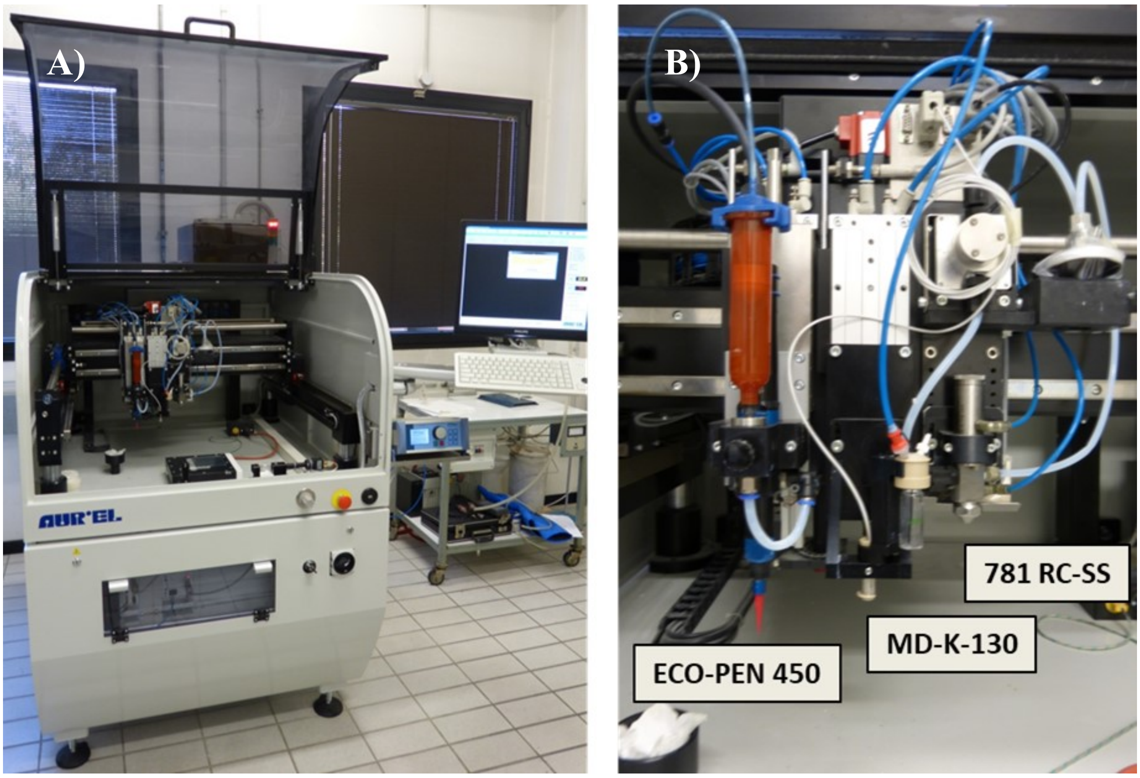

Figure 3.1 A) XCEL machine panoramic view and B) ECO-PEN 450 micro-extruder, MD-K-130 inkjet printhead and 781 RC-SS spray valve.

The main machine characteristics are reported in Table I while the specific features of each deposition device will be reported in a dedicated section.

Table I. XCEL main characteristics

Characteristic	Value / Description
Substrate dimension	20x20 cm^2
X-Y axis, Linear motors	Max speed 600 mm/s, repeatability error ± 5 µm
Z axis	Max speed 50 mm/s, repeatability error ± 5 µm
Vision system	CCD camera with lighting and drop watcher system
Compressed air	Up to 5 bar
Sample holder temperature	Up to 200 °C

The experimental trials were performed by using a dedicated software designed by Aurel that allows to control the overall deposition processes from the managing of the variables to the deposition path design. Due to the huge number of process variables, the attention was focused only on the most affecting ones. For each of the considered techniques a dedicated paragraph is reported: there, the main process parameters will be described and discussed in terms of their impact on the depositions.

3.3 WPS suspensions: composition and processing

3.3.1 Components

A commercial TiO_2 colloidal aqueous suspension, called CristalACTiV™ PC-S7 (Willebroek, Belgium), was considered as starting material for the spray coating technique; its characteristics are listed in Table II.

Table II. CristalACTiV™ PC-S7 characteristics

	Limits	**Result**
TiO_2 [%]	8.5 - 11.5	10.0
pH	7.0 - 9.0	7.8
SO3 [%]	≤ 0.80	0.44
Fe [mg/Kg]	≤ 150	36
S.S.A BET [m^2/g]	≥ 250	341

The different dilution ratio with distilled water (DW) will be reported in the *Results and discussion* section focusing on the effect of this approach on the suspension stability and wetting behavior.

3.3.2 Processing

A simple process for the production of the suitable suspensions was adopted, based on DW additions to the commercial product and subsequent ultrasonication of the diluted suspensions for 10 minutes.

3.4 WPS depositions

The different suspensions were deposited using a low volume low pressure (LVLP) liquid spray valve 781RC-SS (Figure 2, Nordson EFD, USA) with the characteristics reported in Table III:

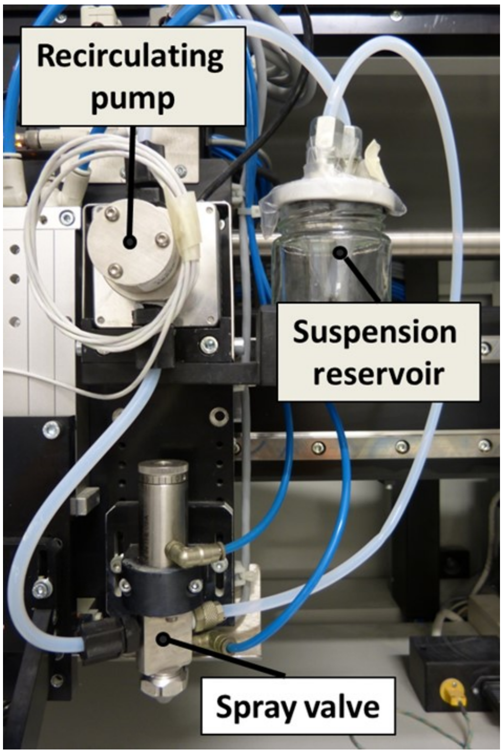

Figure 3.2. Spray coating apparatus

Table III. 781RC-SS spray valve main characteristics

Characteristic	Value / Description
Free flow orifice	360 µm
Air cap and piston material	Stainless steel
Needle and nozzle material	Stainless steel
Maximum air pressure required	6.2 bar
Maximum operating temperature	102 °C
Special feature	Recirculation system

The input air pressure retracts the needle from its nozzle seat, allowing liquid to flow from the nozzle. At the same time, nozzle air is turned on and flows from an annulus around the liquid nozzle. This adjustable nozzle air creates a pressure drop around the nozzle causing the liquid to be atomized in fine droplets.

The orifice diameter, equal to 360 µm, together with the other main process parameters considered in this study are discussed below:

- *Nozzle size:* the nozzle size has a considerable effect on the spraying efficiency. Typical nozzle sizes vary in a wide range from about 100 µm to some millimeters, depending on the suspension viscosity, drying behavior, substrate properties, etc. Under unfavorable conditions the spray nozzle can become clogged or operates in a pulsating unstable manner. To prevent plugging the nozzle diameter should be at least 10 to 20 times larger than the particle diameter.
- *Spraying distance (Z):* the spraying distance can be changed to optimize the deposition conditions. With increasing Z, the layer thickness decreases and the amount of overspray is also directly influenced.
- *Spraying velocity:* similar to Z, also the spraying speed can be chosen to change the layer thickness.
- *Spraying pressure:* the spraying pressure is directly related to the volume of gas passing the nozzle and dispersing the suspension in fine droplets. Finding the right spraying pressure is always a compromise between feed rate (or Fluid flow) and overspray. The higher the pressure, the stronger the atomization will be and the smaller the zone with a homogeneous deposition thickness. Too large volumes of air can also cause powder agglomerates on the substrate surface. If too much carrier liquid evaporates during the flight time, the particles then hit the surface in a “dry” state and tend to form agglomerates.
- *Sample holder T°:* the sample holder temperature determines the drying rate of the sprayed films. In this study, considering water as main solvent, it was fixed at 90°C to rapidly dry the deposited suspensions avoiding the solvent boiling that induces defects on the film morphology.
- *Fluid flow:* the feed rate affects the suspension amount for each deposition cycle. The fluid flow is finely tuned by the operator using the spray valve stroke control. The latter is a graduated scale (ranging from 1/24 to 24/24) to reduce or increase the suspension amount reaching the nozzle.

- *N° of consecutive cycles:* the number of cycles indicates the number of consecutive depositions performed thus affecting the total amount of sprayed suspension.

3.4.1 Sprayed DSCs photoanodes

Ceramic sprayed layers were deposited onto Fluorine-doped Tin Oxide (FTO) glass substrates (sheet resistance 7 Ω/sq, Sigma-Aldrich) additionally coated with a TiO_2 blocking layer (BL), deposited according to a procedure developed in ISTEC laboratories [1]. The optimized sprayed films were produced using the following parameters:

Area	**Nozzle Ø**	**Spray Pressure**	**Deposition velocity**	**Sample holder T°**	**Fluid Flow**	**Z**	**N° of consecutive cycles**
1 cm^2	360 μm	1 bar	50 mm/s	90°C	7/24	75 mm	15

Afterwards the as-realized films were treated at 450°C for 30 minutes. The thickness of the films was adjusted at about 3 μm.

3.5 Micro-extrusion inks: composition and processing

3.5.1 Components

Different ink formulations were considered, in order to evaluate the effect of the different components. The latter are listed in this section.

Semiconductor powder: TiO_2 Aeroxide P25, weight ratio of anatase and rutile 80:20, primary particle size 25 nm, BET surface area 57 ± 15 m^2/g (Evonik Industries, Germany).

Solvent: Milli-Q water, resistivity (at 25°C) 18.2 MΩ·cm (Merck, USA) with few NH_4OH drops.

Dispersant: Duramax D3005 [2], ammonium salt of a polyelectrolyte (Figure 3.3), total solids 35%, MW ~ 2400 daltons, (Rohm and Haas, USA).

Binders: hydroxypropyl cellulose [3], MW 100000, viscosity (5 wt.% aqueous solution, 25°C) 75-150 mPas (purchased from Alfa Aesar, Germany). Tylose H10000 P2, hydroxyethyl cellulose, viscosity (2 wt.% aqueous solution, 25°C) 6000 - 7500 mPas (purchased from SE Tylose, Germany). The celluloses will be labelled as HPC and HEC (Figure 3.3) and followed by numbers corresponding to their weight ratios.

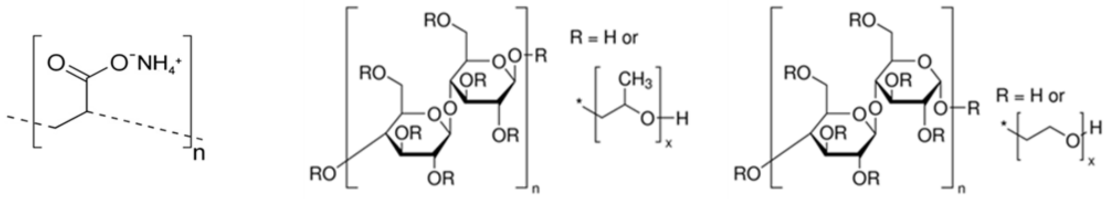

Duramax D3005 **HPC** **HEC**

Figure 3.3. Structural formulas of Duramax D3005, HPC and HEC

Humectant: ethylene glycol, vapor pressure (at 25°C) 0.123 hPa (Sigma-Aldrich, St. Louis, MO, USA). The humectant function is to reduce the ink drying rate avoiding undesired effects like nozzle clogging or cracks on the extruded material.

Finally, a commercial TiO_2 colloidal aqueous suspension, called CristalACTiV™ S5-300B (Willebroek, Belgium), was considered as an alternative to the semiconductor powder; the relative characteristics are listed in Table IV:

Table IV. CristalACTiV™ S5-300B characteristics

	Limits	**Result**
TiO_2 [%]	15 – 20	18.0
pH	10.5 - 12.5	12.0
SO3 [%]	≤ 0.70	0.54
Fe [mg/Kg]	≤ 80	40
S.S.A BET [m^2/g]	≥ 250	311

The compositions of the prepared inks will be reported in the *Results and discussion* section focusing on the different variables considered.

3.5.2 Processing

Different TiO_2 inks production processes were adopted during this phase of the study. The initial one was based on moderate mechanical stirring method for the mixing and homogenization of the components. The schematized procedure is reported in Figure 3.4.

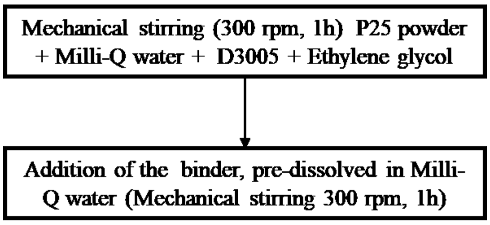

Figure 3.4. Mechanical stirring processing of TiO_2 powder-based inks for micro-extrusion

In more detail, the systems were mixed by mechanical stirring at 300 rpm using a vertical shovel connected to an electrical motor. The 10 wt.% HPC and 6 wt.% HEC solutions were prepared by dissolving the natural polymers in Milli-Q water. Two additional approaches to improve the formulation process were tested (ball milling and ultrasonitcation) and they will be treated more in detail in the *Results and discussion* section of the work. Finally, the original procedure was deeply modified:

- the P25 powder, D3005 and Milli-Q water were substituted by the CristalACTiV™ S5-300B product;
- the HPC and HEC were directly dissolved in the Cristal product exploiting its water content;
- the mechanical stirring was completely substituted by a treatment with a planetary centrifugal mixer (Thinky, Japan), in order to obtain a more efficient particle dispersion and a suitable homogenization of the constituent materials.

These modifications will be presented more specifically in the Results and discussion section of the work.

3.6 Micro-extrusion depositions

The inks were deposited using a dispenser unit (referred as micro-extruder), ECO-PEN 450 (Figure 3.5, Preeflow by ViscoTec, Germany) with the following characteristics (Table V):

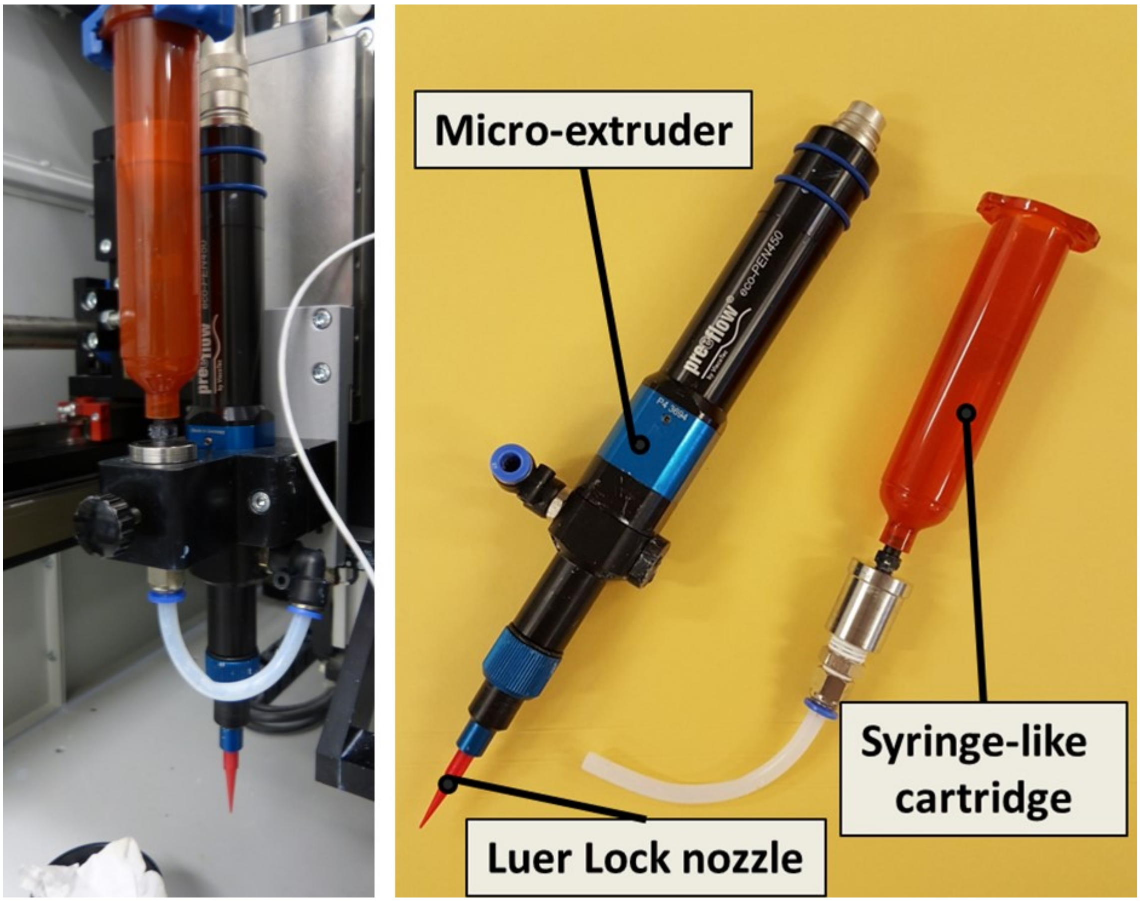

Figure 3.5. ECO-PEN 450 micro-extruder

Table V. ECO-PEN 450 main characteristics

Characteristic	Value / Description
Max operating pressure	0 – 6 bar
Material part in contact with the media	HD-POM/stainless steel
Approx. dosing vol. per revolution	0.05 ml
Accuracy of dosing	± 1%
Min. dosing quantity	0.004 ml
Volume flow	0.5 to 6.0 ml/min

The volume flow represents one of the main process parameters considered in this study, the other ones, excluding the ones in common with the spray technique, are here discussed:

- *Nozzle diameter:* the diameter strongly determines the print quality. In this study different diameters (from 400 down to 50 μm) were considered to realize finest 3D structures. Thinner layers are necessary to produce high quality depositions.
- *Extrusion modality:* three different dosing programs can be selected; (i) the quantity program is used to deposit a fixed and defined quantity of the medium. Depending on the dispenser and the medium used, it is possible to set very small amounts per dosing (ml/g per minute). The dosing time is determined by the volume flow. (ii) The start/stop (or pulse) program is used when the dispenser is set to convey the medium for the relevant individual period by the operator. The amount that is dispended can be defined (ml/g per minute). The dosing quantity is determined by the volume flow. Finally, (iii) the time program is used if the dosing has to be done for a set period. This is triggered by the operator and the amount that is dispensed can be defined (ml/g per minute).
- *Deposition time:* the deposition time indicates the time required to realize the desired geometry.
- *Supply advance time:* it represents a short period of time, just before the depositions, where the micro-extruder moves aside from the desired path and the material starts to flow from the nozzle. This is a standard procedure normally applied in the micro-extrusion field to homogenize the material flow avoiding discontinuities during the deposition process.

3.6.1 3D Engineered photoanodes for DSCs

Three dimensional ceramic structures were micro-extruded onto the optimized spray coating films using the following parameters: nozzle diameter 50 μm, applied pressure 5 bar, holding time 1 s and Z equal to 0.25 mm. Afterwards the layers were dried at room conditions for 24 h and finally treated at 450°C for 30 minutes. The TiO_2 micro-pillars mean height was adjusted at about 15 - 20 μm.

3.7 Inkjet inks: composition and processing

3.7.1 Components

Different ink formulations were prepared, in order to evaluate the effect of this components.

Semiconductor powders: TiO_2, anatase phase 100%, primary particle size 140 nm, BET surface area 10.91 m^2/g (Sigma-Aldrich, St. Louis, MO, USA).
TiO_2 Aeroxide P25, weight ratio of anatase and rutile 80:20, primary particle size 25 nm, BET surface area 57 ± 15 m^2/g (Evonik Industries, Germany).

Solvent: buffer aqueous solution of NH_4OH in Milli-Q water, resistivity (at 25 °C) 18.2 MΩ•cm (Merck, USA).

Dispersant: Duramax D3005, ammonium salt of a polyelectrolyte, total solids 35%, MW ~ 2400 daltons, (Rohm and Haas, USA).

Binders: poly (vinyl alcohol) [4] (PVA, Figure 3.6), MW (85000-124000), viscosity (4 wt.% aqueous solution, 25 °C) 23-27 mPas (purchased from Sigma-Aldrich, St. Louis, MO, USA). Duramax B-1000, acrylic latex emulsion, total solids 55%, viscosity ≤ 140 mPas (Rohm and Haas, USA).

Surfactant: Triton X-100 [5] (Figure 3.6), non-ionic compound (Sigma-Aldrich, St. Louis, MO, USA).

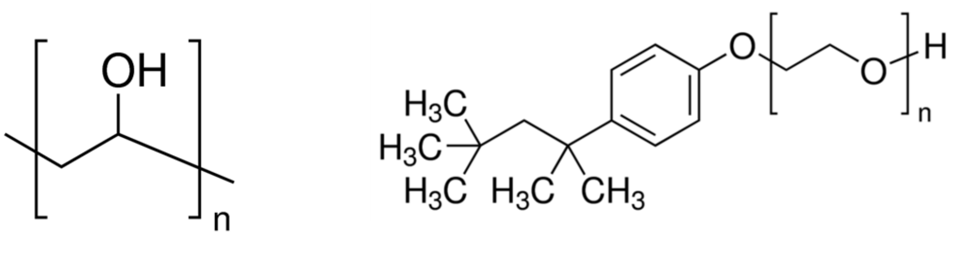

PVA

Triton X-100

Figure 3.6. Structural formulas of PVA and Triton X-100

3.7.2 Processing

Different processes for the production of TiO_2 inkjet inks were adopted during the study. The starting one was based on a gentle magnetic stirring step for the mixing and homogenization of the components. The procedure is schematized in Figure 3.7.

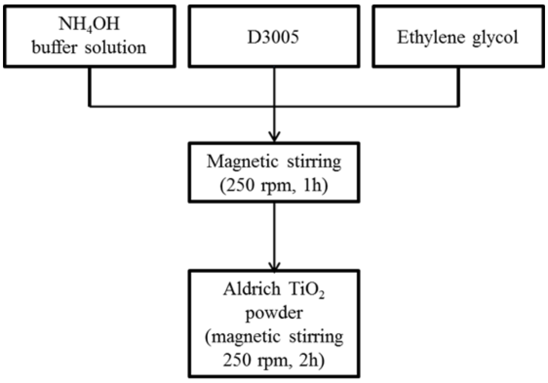

Figure 3.7. Magnetic stirring processing for the initial inkjet inks formulation

The raw materials were mixed by magnetic stirring at 250 rpm. Other three different approaches were tested (ball milling, planetary ball milling and ultrasonitcation) to improve the formulation quality.

3.8 Inkjet depositions

The designated equipment for the high aspect ratio pillars production using the aqueous inks is the print head MD-K-130 (Figure 3.8, Microdrop, Germany).

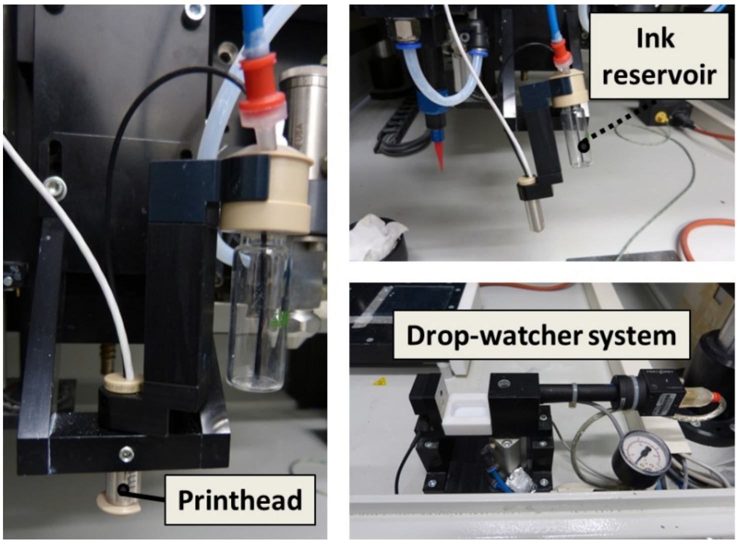

Figure 3.8. MD-K-130 printhead and the drop-watcher system

The device characteristics are reported in Table VI.

Table VI. MD-K-130 main characteristics

Characteristic	Value / Description
Viscosity range	0.4 – 20 mPas
Inner nozzle diameter	50 µm
Droplet volume range	20 – 180 pl
Life time	> 100 billion cycles

The viscosity range is the key parameter to be taken into account for the inkjet printing. However, there are other parameters that are extremely important for the correct execution of this process like the pulse voltage and duration and the frequency (discussed in Chapter 4). Their fine tuning lead to a stable droplet generation which ensures high quality depositions.

3.9 DSCs assembly

The as-obtained photoanodes were dipped for 20 hours in a 0.3 mM ethanolic solution of (cis-diisothiocyanato-bis (2,2'-bipyridyl-4,4'-dicarboxylato) ruthenium (II) bis (tetrabutylammonium) dye (Figure 3.9, N719, Sigma-Aldrich). Prior to complete the DSC prototypes production, the dye uptake on sprayed layers and complete engineered photoanodes was quantified desorbing the ruthenium complex by using a 0.1 M NaOH aqueous solution. The resulting solution (4 ml) was analyzed by UV-Vis spectroscopy and the related absorbance was used to calculate the concentration of dye molecules, using a previously obtained calibration curve.

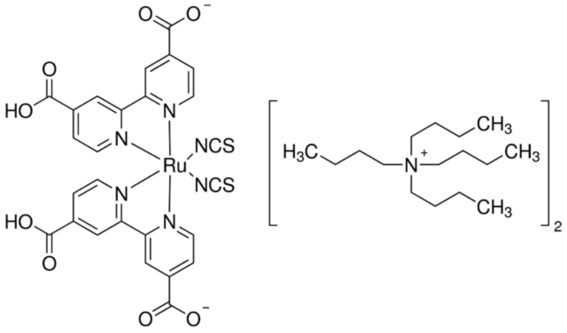

Figure 3.9. Structural formula of the N719 dye

After the photoanodes sensitization, a pre-drilled FTO coated glass covered with a sputtered Pt layer was used as counter electrode. The electrodes were then assembled into a sandwich type cell and sealed with a hot melt gasket made of meltonix (Solaronix, Switzerland). The latter was used selecting two different film thicknesses: 25 and 60 μm. The second one was used for the sealing of engineered photoanodes containing micro-pillars in order to avoid short circuit issues. Profilometer analysis in fact, revealed some 3D objects with heights higher than 25 microns, thus a thicker gasket was preferable. Iodide/tri-iodide (100 mM) based-electrolyte, composed by a mixture of an ionic liquid, alkylbenzimidazole, thiocyanate and 3-methoxypropionitrile (Iodolyte Z100, Solaronix, Switzerland), was introduced in the cell via vacuum back filling through the hole in the counter electrode. Finally the hole was sealed using a Meltonix film and a small cover glass. The active area of the solar cells was fixed at 1 cm^2.

3.10 Characterizations

3.10.1 Dynamic Light Scattering and zeta potential

Dynamic light scattering (DLS) [6], also known as photon correlation spectroscopy, and zeta potential (ζ) have emerged as simple techniques executable under ordinary lab environments to investigate the (hydrodynamic) size and surface charge of nanoparticles (NPs), respectively. Dispersions of NPs in colloidal systems show dual phases (dispersed and dispersant), do not settle over time and are characterized by Brownian motion of the particles [7]. For charged NPs the system becomes even more complex due to the interactions between surfaces, molecules and ions leading to the creation of adsorbed layers on NPs [8]. Both DLS and ZP utilize these properties of colloid dispersions in order to deduce the hydrodynamic radius (R_H) [9] and potential difference at the characteristic slipping plane of electrophoretically mobile particles [10].

DLS is based on the scattering originated by the impact of a laser with a colloidal suspension, with sub-micrometric particle dimension (0.6 nm – 6μm). The technique is based on the assumption that every particle, subjected to a Brownian motion, produces scattering effects when hit by light. The velocity of the particles is proportional to their dimension, large particle will then move more slowly than small ones. The fluctuation frequency of scattered light is dependent on the scattering velocity that is itself related to the dimensions. For this reason particle dimension can be extrapolated by analyzing the fluctuation of scattered light intensity.

The zeta potential (ζ), also termed as electrokinetic potential, is the potential at the slipping/shear plane of a colloid particle moving under electric field [11]. ζ reflects the potential difference between the electric double layer (EDL) [12] of electrophoretically mobile particles and the layer of dispersant around them at the slipping plane.

When a charged particle is dispersed, an adsorbed double layer (referred as EDL) develops on its surface (Figure 3.10).

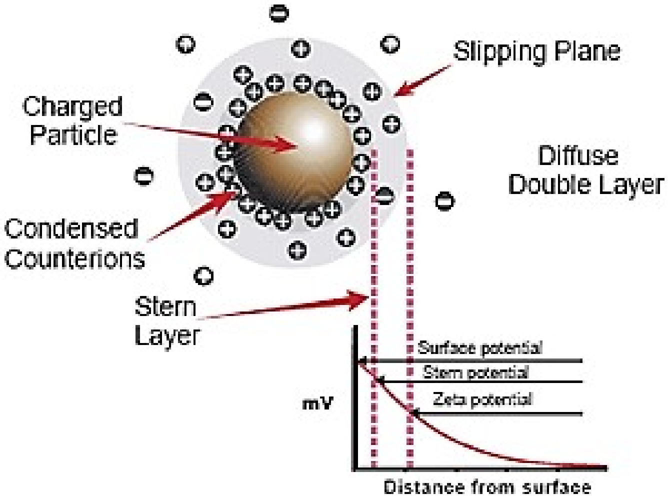

Figure 3.10. Schematic showing the distribution of ions around a charged particle [13]

The inner layer consists predominantly of ions/molecules with opposite charge to that of the particle (Stern layer). Beyond Stern layer the electrostatic effects due to the surface charge on the particles decrease as per Debye's law which states that with the distance of each Debye length the field decreases by a factor of 1/e [14].

This electrostatic effect is only present, experimentally, till few nm from particle surface. Due to the electrostatic field of the charged NPs, a diffuse layer consisting of both same and opposite charged ions/molecules grow beyond the Stern layer which along with the Stern layer forms the EDL. The composition of this diffuse layer is dynamic and varies depending on a variety of factors (e.g., pH, ionic strength, etc). When an electric field is applied to such dispersion, the charged particles move towards the opposite electrode (electrophoresis). Within this diffuse layer there is a hypothetical plane which acts as the interface between the moving particles and the layer of dispersant around it while electrophoresis. This plane is the characteristic slipping/shear plane and ζ is the potential at this particle-fluid interface.

These two techniques are often coupled in one single instrument, like the Zetasizer Nanoseries (Malvern Instruments, UK) used in this thesis, with the possibility to determine NPs dimensions and their zeta potential simultaneously. For DLS measurements, the analysis were carried out using, as radiation source, a laser (λ = 633nm) that is scattered by the NPs in all directions and detected only in the one corresponding to the position of the detector (173° with respect to the incident ray). The system measures the R_H of particle, that is comprehensive of the coordination sphere and species eventually adsorbed on the surface. Concerning the zeta potential determination, an electric field is applied and the electrophoretic mobility of the particles is measured. During electrophoresis, the moving NPs scatter the incident laser light which has different frequency than the original laser and the frequency shift is proportional to the particles speed (Doppler shift). Briefly, the laser beam is split into two and while one beam is directed towards the sample the other one is used as reference beam. The scatter light from the sample is combined with the reference beam to determine the Doppler shift. The magnitude of particle velocity is deduced from the Doppler shift and then ζ is measured through a series of mathematical equations (Henry Eq., Helmholtz-Smoluchowski Eq. and Hückel Eq.).

3.10.2 Contact Angle and Surface Tension measurements

Surface tension, expressed as mN/m, is a force acting at the interface between different phases (solid-liquid-gas) and for the liquids can be defined as the energy needed to increase the surface of a unit. This force is responsible for the tendency of liquids to reduce their surface, it is strictly dependent on the chemical-physical characteristics of the systems and by the thermodynamic equilibrium between the phases. Depending on the considered interface it can be distinguished into: surface tension, measured at the liquid-gas interface (pendant drop in air); interfacial tension, if the measure is referred to a liquid-liquid interface (between not miscible liquids, i.e. oil drop in water); surface energy, performed on solids at the solid-gas interface, provides information about solid wettability, in particular is an expression of hydrophylicity, hydrophobicity and oleophobicity behaviors.

Contact angle is related both to the surface tension and the thermodynamic equilibrium between phases, and it is analyzed to measure the wettability of surfaces. Considering a droplet deposited on a horizontal surface, it can be defined contact angle the angle formed by the liquid-gas interface with respect to the solid. Usually, surfaces showing contact angle with water higher than 90 are considered hydrophobic and for contact angle lower than 90 degrees hydrophilic (Figure 3.11).

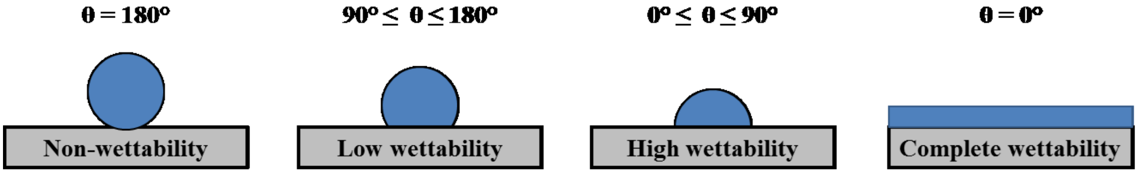

Figure 3.11. Relations between wetting tension and the wetting of a solid surface

Surface tension and contact angle determinations were performed using an optical contact angle system (OCA 15 Plus, DataPhysics Instruments, Germany). The instrument software (SCA 20) provides information about the samples throughout the analysis of its image, while an algorithm based on the Young-Laplace equation, is used to correlate the drop shape with the surface tension and the contact angle. With this instrument is possible to measure the surface tension through the pendant drop method and the contact angle by using the sessile drop method. In the pendant drop method, a drop hangs by the top of a flat needle, while in the sessile drop method, a drop of a liquid is placed on a solid, plane and waterproof surface. In both cases the drop gets a shape that depends by its weight, density, surface tension and by the liquid affinity toward the surface. The drop profile is analyzed by the high performance video camera and processed by the software in order to obtain surface tension and contact angle.

3.10.3 Rheological analysis

Rheology is the study of flow and deformation of materials under applied forces which is routinely measured using a rheometer. The measurement of rheological properties is applicable to all materials, from fluids such as dilute solutions of polymers to semi-solids such as pastes and creams, to molten or solid polymers. Many commonly-used materials and formulations exhibit complex rheological properties, whose viscosity and viscoelasticity can vary depending upon the external conditions applied, such as stress, strain, timescale and temperature. Internal sample variations such as solid concentration and stability are also key factors that determine rheological properties. The latter can be measured from bulk sample deformation using a rotational rheometer, as in this work. This type of rheometer applies a known force to the sample and measure how it reacts to the force and the force that the sample then exerts on the rheometer. Rotational rheometry is a powerful technique for the measurement of complex shear rheology across several material types, it is ideal for discerning structural and compositional changes of materials, which can be critical controlling factors in flow and deformation properties.

The basics of the rotational rheometry technique are as follows: (i) the sample is loaded into the gap of a measuring system (or geometry), such as parallel plates, a cone and plate or a concentric cylinder system (Figure 3.12) specifically designed to impose simple shear flow when rotated. (ii) Various rheological characteristics of the sample can be determined by rotating, oscillating or applying a step function to the measuring system, either by controlling motor torque (stress controlled rheometry) or position change (strain controlled rheometry). Common test modes are rotational (or flow) to measure shear viscosity, and oscillation to measure dynamic material properties such as viscoelastic modulus and phase angle [15].

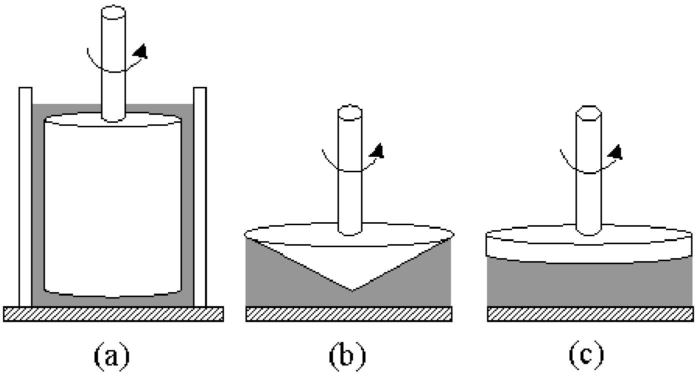

Figure 3.12. Schematic diagram of basic tool geometries for a rotational rheometer: (a) concentric cylinder, (b) cone and plate, (c) parallel plate [16].

In this thesis, the rheological measurements were performed by using a controlled-stress rotational rheometer (Bohlin C-VOR 120, Bohlin, Malvern, UK) equipped with plate-plate (d = 20 mm) and cone-plate (cone of 4° and d = 40 mm plate) flow geometries. All the measurements were performed at 25°C setting the distance between the plates at 500 μm. The different set-ups were used to measure the flow curves (viscosity vs. shear rate) and the frequency sweep.

Flow curves: Viscosity-shear rate measurements, for the micro-extrusion inks, were performed by sweeping over 50 values of shear rate (in logarithmic scale), between 0.01 and 500 s-1. Before the measurement a pre-shear of 1 minute at 0.01 s-1 was first applied, after which the shear rate was increased and subsequently decreased. For the inkjet inks on the contrary, the analyses were performed over 70 values of shear rate between 2 and 1500 s-1. Pre-shear conditions were applied also in this case.

Frequency sweep (only for the micro-extrusion ink): The viscoelastic response was determined by keeping a constant oscillation frequency (1 Hz) over a shear stress range between 0.1 and 1000 Pa.

3.10.4 UV-Vis spectroscopy

UV-Vis analyses were performed to evaluate the photoanode transparency. UV-Vis spectroscopy is based on the selective absorption of radiations with wavelength between 10-780 nm. In practice, a ray is generated by a source, generally a tungsten lamp for the visible region and a deuterium one for the UV, and then it is direct to a monochromator that separates the polychromatic ray in a series of monochromatic bands. The resulting ray is split by a chopper into two rays directed respectively to the sample and the reference. After having interacted with the samples, the rays reach the detector that converts the energy in an electrical signal. Defining I0 the intensity of the incident light and I the resulting one, the ratio I/ I0 is the transmittance (T), which shows values ranging from 0 to 1. The amount of absorbed light is instead defined Absorbance (A) calculated as Log T. When analyzing solids, light is scattered in all directions, and in this case the technique is defined diffuse reflectance. For such technique a so-called integrating sphere is used. It consists of a chamber whose inner parte is made of a material generating the highest reflection in the visible range. In this way, the light diffused by the sample reaches the detector without being dispersed. The analyses were carried out using the PVE300 system of Bentham (United Kingdom).

3.10.5 Profilometry

Profilometry analyses were conducted to study the surface features of both the deposited sprayed layers and 3D structures determining their thickness and aspect ratio respectively. In order to not damage the surface of the samples, a non-contact system was used (Contour GT-K 3D non-contact profilometer, Bruker, Germany). This system is based on white light interferometry, that uses the wave superimposition principle to combine waves in order to extract information from the results of their combination. In particular the waves form a pattern depending on the phase difference between them, which will generate a constructive or destructive interference. In practice, a CCD sensor is placed at the point where the two images are superimposed. A white light source is used to illuminate the test and the reference surface, and a lens collimates the light. Then a splitter separates the light into the reference and measurement beams reflected by the reference mirror and from the test surface respectively. The returning beams are then collected by the CCD sensor that converts the resulting interference pattern into the surface topography.

3.10.6 Photovoltaic performance

The photovoltaic performance of the produced devices were determined using a solar simulator (SUN 2000, Abet Technologies, USA) at 1000 W m^{-2} AM 1.5G illumination (calibrated with a standard silicon cell).

J-V curves were obtained by applying an external bias (with imposed scan rate) to the cell and measuring the generated photocurrent with a Keithley SourceMeter (Model 2400) [17]. The shape of the traditional J-V curves was reported in Figure 3.13.

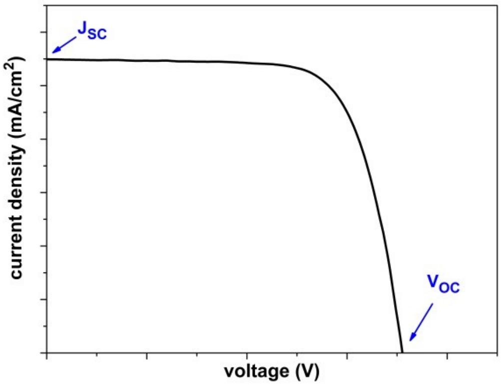

Figure 3.13. Traditional shape of J-V curve under illumination related to DSC

From J-V curve the short circuit current density (J_{sc}) were determined at applied voltage equal to zero, while the Open Circuit Potential (V_{oc}) was determined at the applied current equal to zero. Considering these two fundamental parameters and the Fill Factor of the cell, the final photovoltaic efficiency was equal to:

$$\eta = \frac{J_{SC} \times V_{OC} \times FF}{P_{IN}} \ (\%)$$

where P_{in} correspond to the incident power and was equal to 1000 W/m^2. The IPCE was quantified with the IPCE PVE300 system (Bentham, United Kingdom) with dual xenon/quartz halogen light source, in the wavelength range between 300 and 1800 nm.

3.10.7 Electrochemical impedance spectroscopy (EIS)

Considering a generic circuit composed of a capacity (C), an inductance (L) and a resistance (R), powered by an alternated tension V(t), sinusoidally function of time $V(t) = AM \cos(\omega t + \alpha)$ (with AM, ω and α respectively amplitude, pulse and phase of the wave) the resulting current I(t), itself sinusoidal, is calculated using the so-called symbolic Ohm law: $V = ZI$, with Z defined as $Z = R + j(\omega L - 1/\omega C)$.

This quantity is defined the Impedance of the circuit, and represents the ability of the system to impede the charge current flux. The real part corresponds to the resistance of the circuit, while the imaginary one, called reactance, depends on the other components of the system. The inverse of impedance is defined admittance of the circuit.

The impedance is then a more extended concept than resistance since it is also dependent on time and frequency, so $Z = V(t) / I(t)$.

In practice, the impedance analysis is carried out by applying a low intensity alternate current, so to work in pseudo-linearity conditions. The frequency range typically varies from 100 KHz to 1 mHz. The resulting sinusoidal current presents variations of amplitude and phase due to the characteristic of the system under investigation. Analyzing this perturbation is then possible to study the components of interest. This technique is extremely useful since it allows to simulate electrochemical systems with the so-called equivalent circuits, composed of resistances, capacities, inductances and other elements that allow to describe and study the electrochemical phenomena occurring in the system.

EIS was carried out using an Autolab PGSTAT302N with an internal frequency response analyzer (Eco Chemie, The Netherlands). The impedance spectra were elaborated using the Z-view software (Scribner Associates, USA). EIS spectra were registered in the frequency range from 0.05 to 10^5 Hz, with an amplitude of 10 mV, under illumination (1000 W/m^2) and open circuit conditions.

3.10.8 Scanning electron microscopy (SEM)

Scanning electron microscopy was used to observe the microstructure of the ceramic layers and 3D structures. This technique exploits an accelerated electron beam to scan the surface of the sample and to register an image. This process generates different signals, the most used are the ones produced by secondary and back-scattered electrons. The first are electrons with energy up to 50 eV, deriving mainly from the interaction between the beam and the nuclei of the sample atoms. In this case a field emission gun-scanning electron microscope (FE – SEM, ΣIGMA: Zeiss, Germany) was used. In this class of microscopes, the beam is produced by a tungsten single crystal, in this way the beam is smaller, more coherent and has an higher current density than the ones generated by traditional termoionic emitters (LaF_6). The results is a significant improvement in the signal-to-noise ratio and resolution.

References

[1] A. Sangiorgi, R. Bendoni, N. Sangiorgi, A. Sanson, B. Ballarin, *Optimized TiO_2 blocking layer for dye-sensitized solar cells*, Ceramics International, 2014, 40, 10727-10735.

[2] A. Tsetsekou, C. Agrafiotis, A. Milias, *Optimization of the rheological properties of alumina slurries for ceramic processing applications, Part I: Slip-casting,* Journal of the European Ceramic Society, 2001, 21, 363-373.

[3] O. W. Guirguis, M. T. H. Moselhey, *Thermal and structural studies of poly(vinyl alcohol) and hydroxypropyl cellulose blends,* Natural Science, 2012, 4, 1, 57-67.

[4] F. Chabert, D. E. Dunstan, G. V. Franks, *Cross-linked Polyvinyl Alcohol as a Binder for Gelcasting and Green Machining,* Journal of the American Ceramic Society, 2008, 91, 3138–3146.

[5] Z. Zhang, C. Qu, T. Zheng, Y. Lai, J. Li, *Effect of Triton X-100 as Dispersant on Carbon Black for LiFePO4 Cathode,* International Journal of Electrochemical Science, 2013, 8, 6722-6733.

[6] S. Bhattacharjee, *DLS and zeta potential – What they are and what they are not?*, Journal of Controlled Release, 2016, 235, 337-351.

[7] A. Satoh, R. W. Chantrell, G. N. Coverdale, *Brownian dynamics simulations of ferromagnetic colloidal dispersions in a simple shear flow*, Journal of Colloid and Interface Science, 1999, 209, 44–59.

[8] L. Dalstein, M. Ben Haddada, G. Barbillon, C. Humbert, A. Tadjeddine, S. Boujday, B. Busson, *Revealing the interplay between adsorbed molecular layers and gold nanoparticles by linear and nonlinear optical properties*, Journal of Physical Chemistry C, 2015, 119, 17146–17155.

[9] J. Lim, S. P. Yeap, H. X. Che, S. C. Low, *Characterization of magnetic nanoparticle by dynamic light scattering*, Nanoscale Research Letters, 2013, 8, 381.

[10] A. V. Delgado, F. González-Caballero, R. J. Hunter, L. K. Koopal, J. Lyklema, *Measurement and interpretation of electrokinetic phenomena*, Journal of Colloid and Interface Science, 2007, 309, 194–224.

[11] M. Kaszuba, J. Corbett, F. M. Watson, A. Jones, *High-concentration zeta potential measurements using light-scattering techniques*, Philosophical Transactions of the Royal Society A: Mathematical, Physical and Engineering Sciences, 2010, 368, 4439–4451.

[12] F. J. Montes Ruiz-Cabello, G. Trefalt, P. Maroni, M. Borkovec, *Electric double-layer potentials and surface regulation properties measured by colloidal-probe atomic force microscopy*, Physical Review E, 2014, 90, 012301.

[13] http://www.malvern.com

[14] Z. Chen, Z. Wei, Y. Chen, C. Dames, *Anisotropic Debye model for the thermal boundary conductance*, Physical Review B, 2013, 87, 125426.

[15] https://www.malvern.com/en/products/technology/rheometry-rotational

[16] https://ciks.cbt.nist.gov/~garbocz/SP946/node14.htm

[17] S. Ito, M. K. Nazeeruddin, P. Liska, P. Comte, R. Charvet, P. Péchy, M. Jirousek, A. Kay, S. M. Zakeeruddin, M. Grätzel, *Photovoltaic characterization of dye-sensitized solar cells: effect of device masking on conversion efficiency*, Progress in Photovoltaics: research and applications, 2006, 14, 589-601.

Chapter 4

Results and Discussion

4.1 Introduction

In this chapter, the obtained results and relative discussion are presented. The activity carried out during the PhD program was focused on the following points:

- deposition of TiO_2 porous films using the spray coating technique aimed at producing porous layer with high transparency. The target was properly pursued modifying a commercial aqueous-based colloidal TiO_2 suspension. The interactions between the latter and the FTO substrate were evaluated. The modified suspension stability was investigated in terms of particles dispersion and ζ potential. Subsequently the relationship between the process parameters and the obtained films was evaluated in terms of transparency and microstructure; the most suitable film was then sensitized and used to produce a complete DSC prototype;
- development of a 3D architecture composed of coarse TiO_2 micro-pillars realized using micro-extrusion. The goal was achieved through the formulation of a high-solid loaded ink that possesses proper rheological characteristics; the optimization of the depositions was carried out working on the main process parameters such as velocity, material flow etc. The as-obtained structures were characterized in terms of aspect ratio, microstructure and finally tested in a complete DSC prototype;
- preliminary work on an aqueous-based inkjet ink for high-aspect ratio micro-pillars production. The ink stability, rheology and interaction with the substrate were investigated. An alternative solvent and heavy milling treatments were then applied to effectively increase the ink stability and ensure its printability.

These points will be now described more diffusely, focusing on their role in the realization of 3D engineered photoanodes for DSCs.

4.2 Optimization of the TiO_2-based spray suspension

Spray-deposition combines the possibility of elaborating films with a thickness varying between 200 nm and several micrometers with the capability of depositing these films onto substrates of large dimensions, different shapes and rigidities. Nevertheless, so far, the poor homogeneity and high rugosity of the films made with this technique has been considered as a major drawback for many applications, in particular the optical ones. The main reason comes from the principle of the technique itself, which involves the drying of large droplets whose distribution over the substrate may induce a poor homogeneity and high roughness. Moreover, the drying of the droplet leads to a so-called "coffee-ring effect" that has been documented both theoretically and experimentally in the literature for micrometer-sized particles [1-3]. During the drying process, the drop edges are not free to move but are pinned to the substrate, leading to a solvent flow that drives the particles from the drop center toward the edges and thus to this ring formation. Recently, Yunker et al. studied the drying process of 1.3 µm polystyrene particles with different aspect ratios and have thus proved that the particle shape has a strong effect on the ring formation [3].

Starting from these results, this part of the thesis aims at revisiting the deposition of nanoparticulate coatings to produce a thick mesoporous TiO_2 film with high transparency. The basic idea is that the "coffee-ring effect" could be tuned by destabilizing the TiO_2 colloidal solution prior to its deposition. The presence of aggregates with increased attractive interactions between the NPs would reduce their mobility during the drying of the droplets and would permit a better control of the surface roughness and coatings with an improved transparency. The dimensions of this aggregates must be well controlled and lower than the spray nozzle diameter, which is equal to 360 µm, to avoid clogging issues.

For this study a commercial suspension of 10 nm-sized TiO_2 (pure anatase phase) NPs dispersed in water (CristalACTiV^{TM} PC-S7) was used as starting material. This can be considered as a model system as the NPs are nearly mono-disperse and highly stable in water. Considering this colloidal suspension and in particular its aqueous matrix, one of the easiest way to tune its stability is to increase the water amount. Thus, different amount of Milli-Q water were added to the starting suspension in order to manage the coffee-ring effect (Table I);

Table I. Dilution ratios considered and their corresponding amount of TiO_2 and pH

Sample	Dilution ratio	TiO_2 wt.%	pH
PC-S7_0.2	1:0.2	8.26	8.25
PC-S7_3	1:3	2.50	8.24
PC-S7_5	1:5	1.67	8.23
PC-S7_10	1:10	0.91	8.22
PC-S7_20	1:20	0.48	8.17
PC-S7_40	1:40	0.24	8.02

Table I clearly shows that an increasing amount of water, other than obviously lowering the total TiO_2 amount is affecting the suspension pH shifting it from 8.25 to 8.02 for the most diluted system. In stabilized suspensions, the pH value is fundamental because strictly related to the surface potential of the colloids; alterations of this parameter, even if very small, can lead to strong aggregation effects and thus modification of the related suspension stability. In order to evaluate and quantify these variations the effects derived from the water addiction were evaluated in terms of Z-Ave and ζ potential and consequently in terms of surface tension and drop/substrate interaction.

4.2.1 Suspensions stability: particle dimensions and ζ potential

The suspension stability is a key parameter for the characterization of the spray suspensions. In a colloidal suspension it is generally required to have dispersed NPs to reduce as much as possible their mutual interactions. In this case, the reverse approach was investigated trying to finely tune the suspension stability inducing slight aggregation of the TiO_2 nanoparticles. To precisely follow this approach, size, PDI and ζ potential measurements were performed onto the different diluted samples (Table II and Figure 4.1).

Table II. Z-Averages and ζ potentials of the different diluted samples

Sample	TiO_2 wt.%	Z-Ave [nm]	PDI	ζ Potential [mV]
PC-S7_0.2	8.26	59.4 ± 0.6	0.199 ± 0.007	-28.2 ± 0.9
PC-S7_3	2.50	59.6 ± 0.4	0.170 ± 0.009	-38.2 ± 1.8
PC-S7_5	1.67	59.8 ± 0.3	0.140 ± 0.012	-38.4 ± 1.1
PC-S7_10	0.91	62.1 ± 0.1	0.138 ± 0.010	-40.4 ± 0.3
PC-S7_20	0.48	62.7 ± 0.2	0.129 ± 0.004	-40.9 ± 0.5
PC-S7_40	0.24	63.4 ± 0.2	0.129 ± 0.009	-41.6 ± 1.4

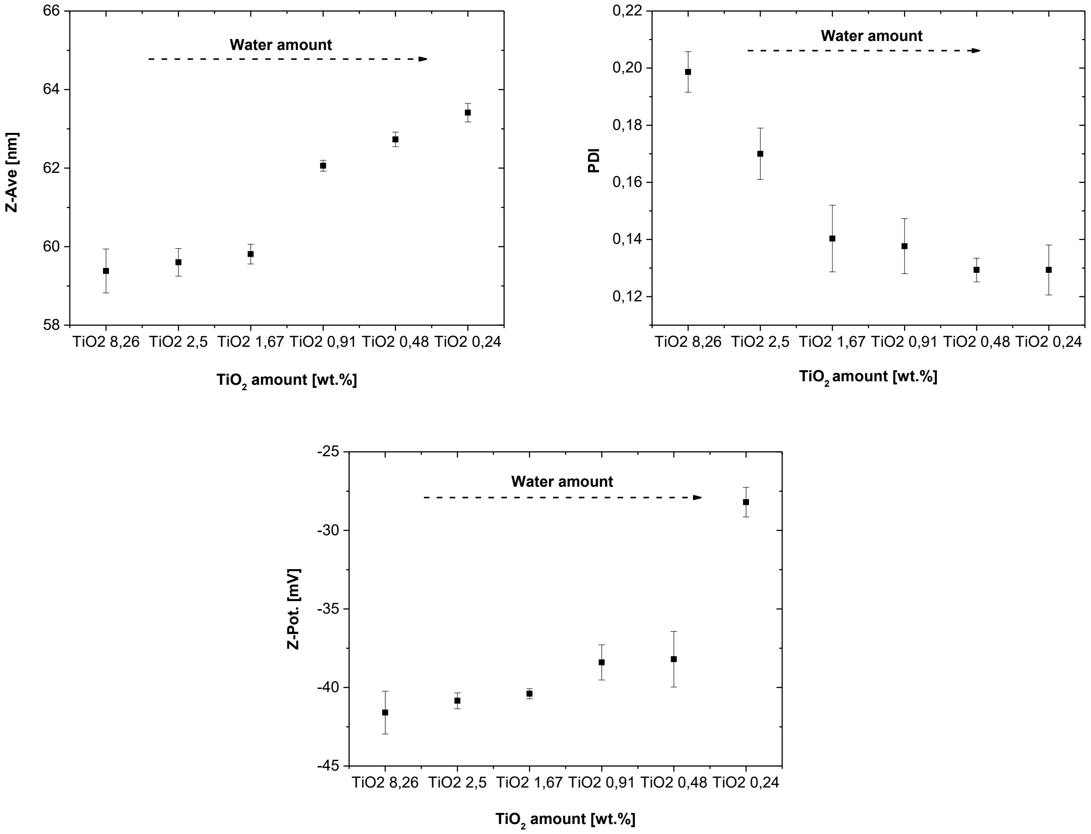

Figure 4.1. Z-Average, Polydispersity Index and ζ potential of the diluted spray suspensions

The water addition reduces the Polydispersity Index (PDI), the higher is the water amount the lower is PDI. This index gives an idea about the particle size distribution (monodisperse systems show PDI ≤ 0.2) thus going from 0.199 down to 0.129 means that the most concentrated suspension is just on the edge between polydispersion and monodispersion while the most diluted ones are clearly monodispersed. The same trend is followed by the ZP (from -28.2 to -41.6 mV): such behavior indicates, as expected, that the diluted suspensions are more stable than the concentrated ones. The Z-Average trend is a little bit different showing a constant value around 60 nm for the PC-S7_0.2, 3 and 5 samples; then the particles dimensions start to increase up to 62 - 64 nm indicating some agglomeration phenomena that promotes flocculation. These studies confirm the possibility to tune the stability of the commercial suspension adding a proper amount of water to it. The effect of this procedure onto the film depositions will be deeply examined in the next section.

4.2.2 Surface tension of the TiO_2 based suspensions and wettability tests

The suspension stability (or instability as expressed before) is just one of the requirements for the spray coating technique. For the deposition process, where several droplets of a suspension containing the nanoparticles are thrown onto an heated substrate, other important characteristics to be considered are, the suspensions surface tensions (generally determined using the pendant drop method) and their behavior when in contact with the substrate. The latter is normally assessed through the so-called wettability tests that consists in the deposition of a small suspension droplet onto the desire substrate and to follow its spreading on it. Prior to perform these specific tests, an empirical procedure (Figure 4.2 A) that emulates the deposition mechanism was applied to macroscopically appreciate the suspensions behaviors during deposition and drying. 5 µl drops of each diluted suspension were deposited onto an FTO glass covered with a spin-coated TiO_2-based blocking layer (BL). Then this system was gently dried and the obtained circular films were photographed (Figure 4.2 B).

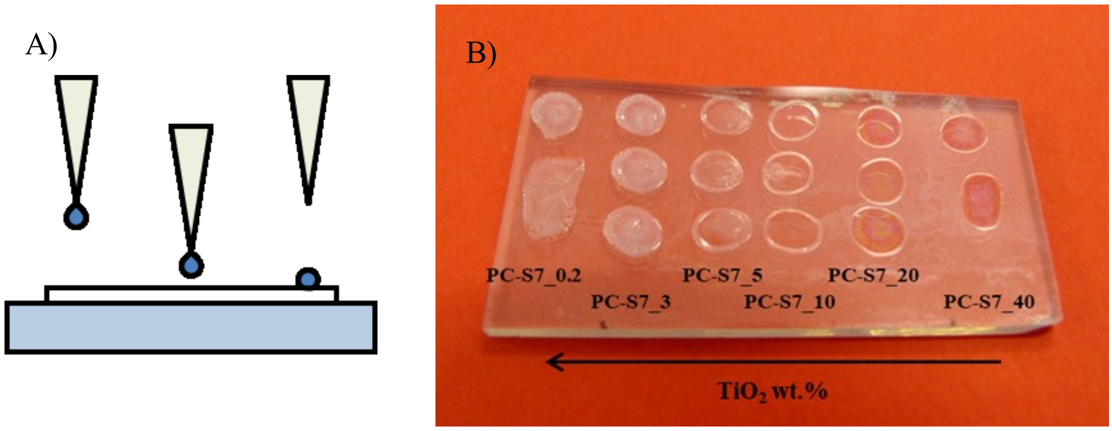

Figure 4.2. Schematization of the empirical deposition process (A) and the obtained dried drops (B)

Figure 4.2 B shows that an increase in the water content leads to a strong coffee-stain effect that is barely present in the sample PC-S7_5 and becomes clearly visible (Figure 3) for all the successive samples with a TiO_2 loading lower than 1 wt.%.

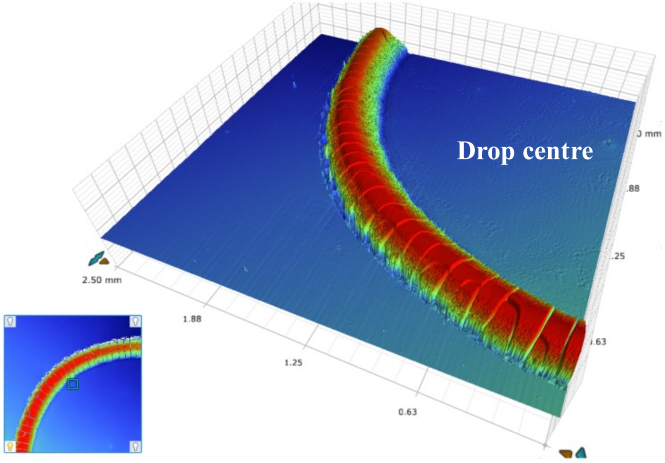

Figure 4.3. 3D image of the coffee ring phenomenon associated to the PC-S7_10 sample

This phenomenon should be carefully controlled to be used for the deposition but not too strong, not to generate irregular depositions increasing the light scattering of the layers reducing their transparency. The highest diluted samples were therefore not considered for the next characterizations. The surface tension data and the relative contact angle values of the remaining samples are summarized in Table III.

Table III. Liquid surface tensions (γ_L) and contact angles (θ) of the different diluted samples onto the FTO/BL substrate

Sample	**γ_L [mN/m]**	**Θ [°]**
PC-S7_0.2	71.71 ± 0.37	85.87 ± 3.45
PC-S7_3	72.20 ± 0.17	89.40 ± 3.69
PC-S7_5	72.92 ± 0.89	90.18 ± 3.07

The γ_L values are comparable for all the samples, indicating that this physical characteristic is less sensible to the water addition as expected by a commercial formulation that is already composed of about 90% of water. Different situation for the θ data; the sample PC.S7_0.2 containing the highest amount of titanium dioxide shows a theta value of about 86° which means a good capability to wet the FTO/BL surface.

Increasing the dilution ratio this affinity becomes lightly weaker going to values around 90°; all the considered samples are suitable for spray depositions considering that they are lying into the theoretical high wettability range of $0 < \theta < 90°$.

In conclusion, taking into account all the data collected from the diluted suspension characterizations, the PC-S7_5 was selected as the best starting system for the spray process as a consequence of the best compromise between suspension stability, homogeneous coverage of the substrate, and TiO_2 content.

4.3 Optimization of the spray depositions

As already mentioned in the previous chapters, the spray coating is a flexible automated technique that allows to deposit lot of different materials with reduced material losses as the whole solution is sprayed onto the substrate. Besides these positive features, the complexity of this technique is commonly underestimated in particular when a high added-value application is considered. The production of a semiconductor films for photo-electrochemical devices like DSCs requires a precise tailoring of the different process parameters in order to obtain an homogeneous film with relatively high thickness (between 2 and 5 μm) and good electrochemical properties. The first set of parameters (discussed in Chapter 3, section 3.4) was fixed (Table IV) considering some indications coming from literature [3-6].

Table IV. Starting set of process parameters

Area	**Nozzle Ø**	**Spray Pressure**	**Deposition velocity**	**Sample holder T°**	**Fluid flow**	**Z**	**N° of consecutive cycles**
1 cm^2	360 μm	1 bar	50 mm/s	90°C	5/24	50 mm	5

In particular, the highlighted process variables were considered as the more affecting ones in terms of deposition quality. In order to optimize the deposition for the desired application, the attention was focused on the amount of material for each spray cycle (Fluid flow), the distance between the substrate and the spray nozzle (Z) and finally the total number of consecutive depositions.

Considering the number of deposition tests done, only the most representative are here reported and discussed; the complete list is however reported in Appendix 1. The deposition trials were initially performed following the conditions in Table IV (SY-S1 sample); afterwards, the Z increase (SY-S2), the number of consecutive spray cycles growth (SY-S3) and finally the fluid flow rise (SY-S4) were investigated respectively. The structural quality of the resulting TiO_2 films was investigated by optical and electronic microscopy, profilometry and transmittance analysis (these spectra were acquired using an integrating sphere and a FTO/BL substrate as a reference).

Starting conditions

Sample	**Fluid flow**	**Z**	**N° of consecutive cycles**
SY-S1	5/24	50 mm	5

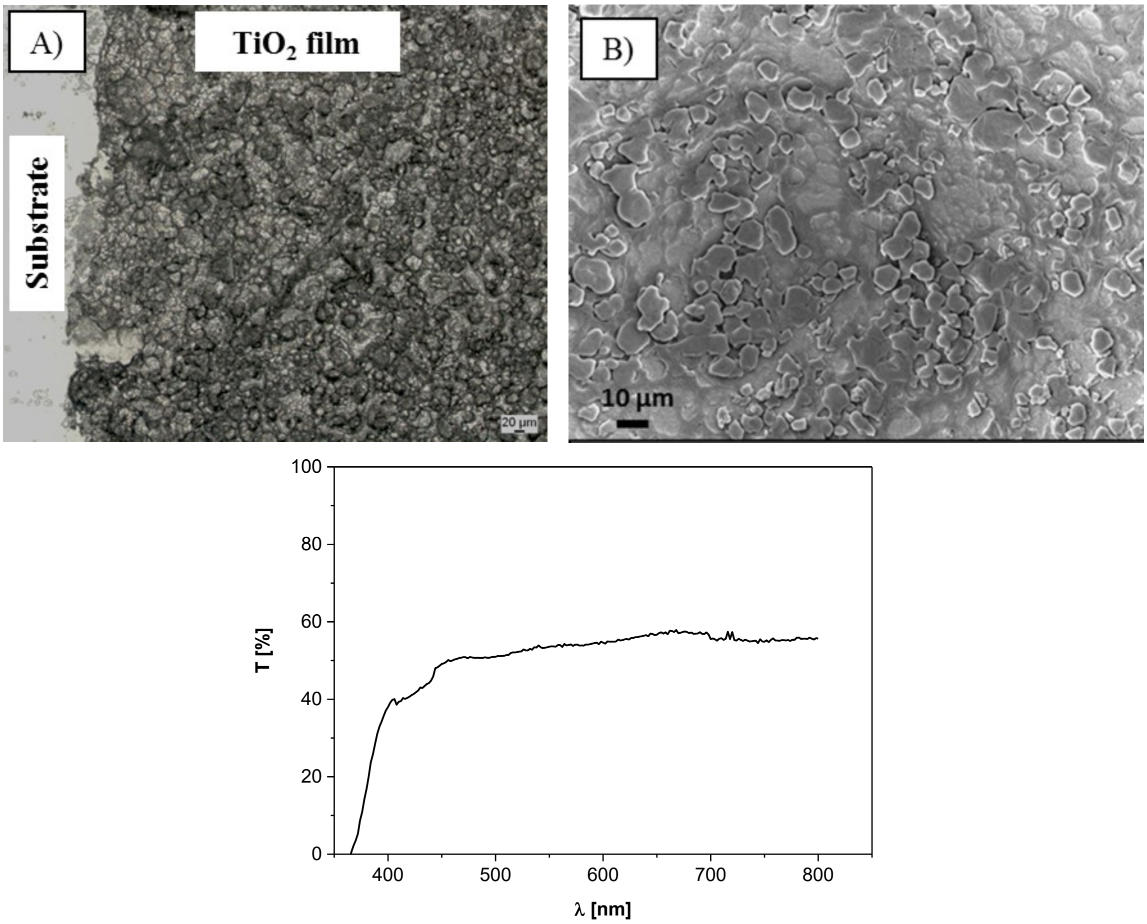

Figure 4.4. A) Optical and B) FE-SEM images of the SY-S1 sample and the relative transmittance spectrum

The obtained film showed inadequate transparency with the formation of several TiO_2 aggregates on the FTO substrate (Figure 4.4 A and B). This low-quality deposition is mainly due to the reduced Z value; it is well-known that when the spray valve is placed too close to the substrate the material bounce back increases resulting in poor finish quality. A rough surface is, therefore, showed by the sample and confirmed by the low transmittance values in the whole range of the analysis. In particular, inside the spectral region of interest, around 525 nm (wavelength corresponding to the highest amount of solar light harvested by the most common dyes (like N719, N3) used in DSCs [7]), the T% is just around 52%; this low value can be mainly ascribed to the aggregates that strongly scatter the incident light making this film completely unsuitable for DSC application.

In order to obtain a higher transparent photoanode for high efficient DSCs, the Z was increased to reduce the uncontrolled material spreading onto the substrate.

Effect of Z variation

Sample	**Fluid Flow**	**Z**	**N° of consecutive cycles**
SY-S2	5/24	75 mm	5

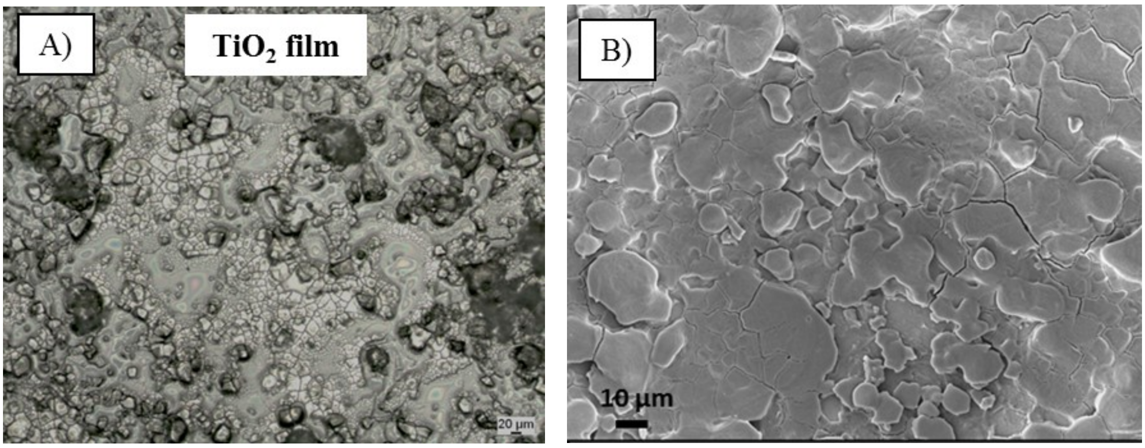

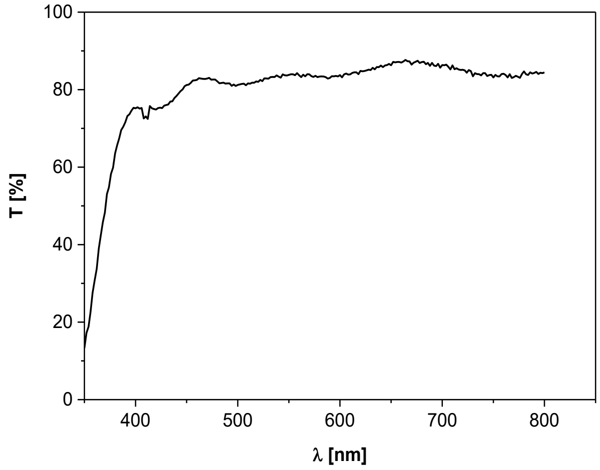

Figure 4.5. A) Optical and B) FE-SEM images of the SY-S2 sample and the relative transmittance spectrum

Even if some TiO_2 aggregates are still present and randomly located (Figure 4.5 A and B) on the surface, the value of roughness is reduced as confirmed by the Ra parameter (arithmetic average roughness) that goes from 41.5 ± 2.3 μm for the first film produced down to 30.5 ± 1.2 μm for the second. The transparency improvement is also highlighted by the considerably increase of transmittance at 525 nm, that reaches 82%. Additional trials were performed to improve the transparency of the sprayed electrode however the aggregates continue to negatively influence the film transmittance. Thus, in order to obtain a smoother surface, the number of deposition cycles was increased from 5 to 15. In this way, after each cycle, the single aggregate is going to be surrounded by fresh suspension which, by coalescence, produces a more flat and homogeneous film. In accordance with the optical and SEM images (Figure 4.6 A and B), the film shows just few aggregates and even if the amount of TiO_2 is increased due to the multiple depositions performed, the transparency is higher than before reaching 88% at 525 nm clear sign of a more homogeneous surface.

Effect of the number of spray consecutive cycles

Sample	**Fluid flow**	**Z**	**N° of consecutive cycles**
SY-S3	5/24	75 mm	15

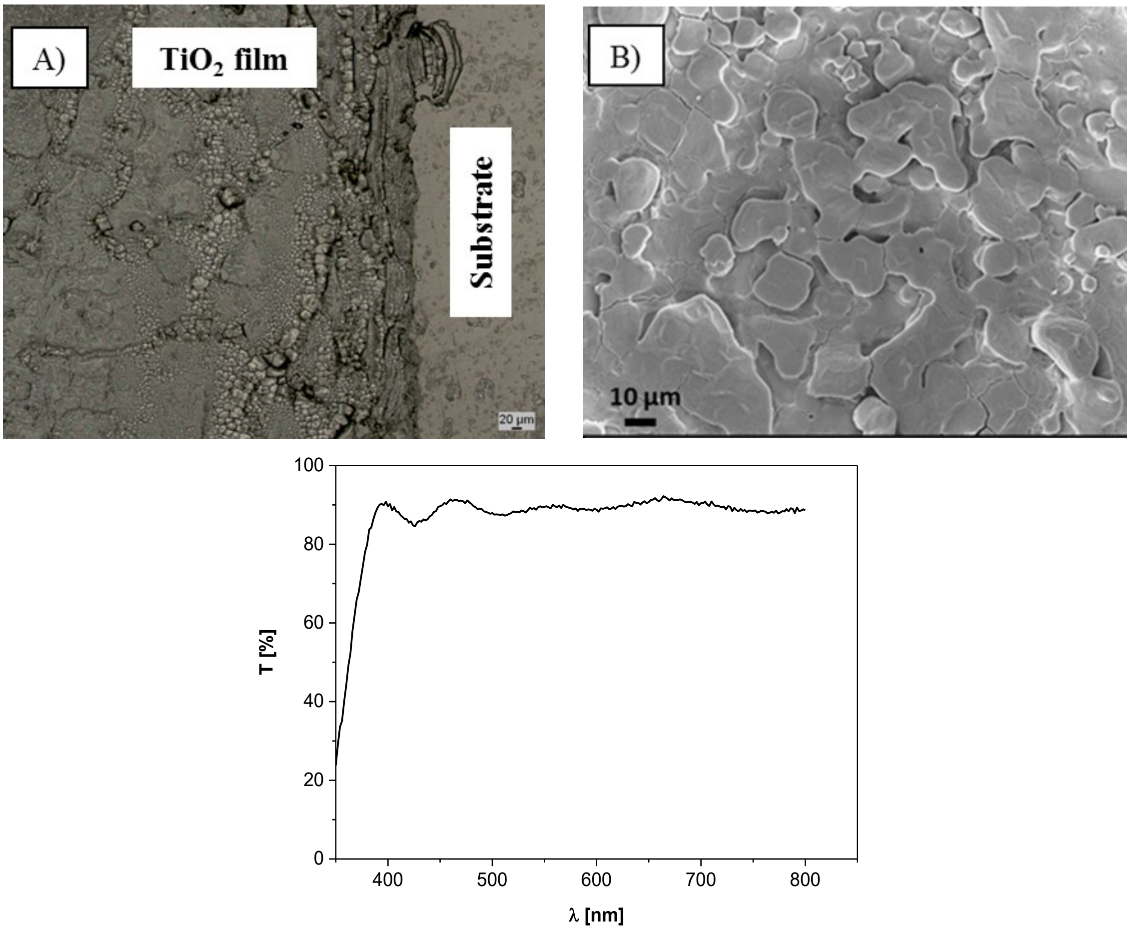

Figure 4.6. A) Optical and B) FE-SEM images of the SY-S3 sample and the relative transmittance spectrum

Finally, also the fluid flow was modified. The results obtained increasing the number of depositions, suggested that a higher number of cycle could lead to highly transparent films. Unfortunately, this approach leads to a more time-consuming procedure that conflicts with the scalability of both spray coating process and DSC devices. Thus, in order to rise the deposited material quantity, the increasing of the fluid flow for each deposition cycle was investigated.

Effect of the Fluid flow variation

Sample	Fluid flow	Z	N° of consecutive cycles
SY-S4	7/24	75 mm	15

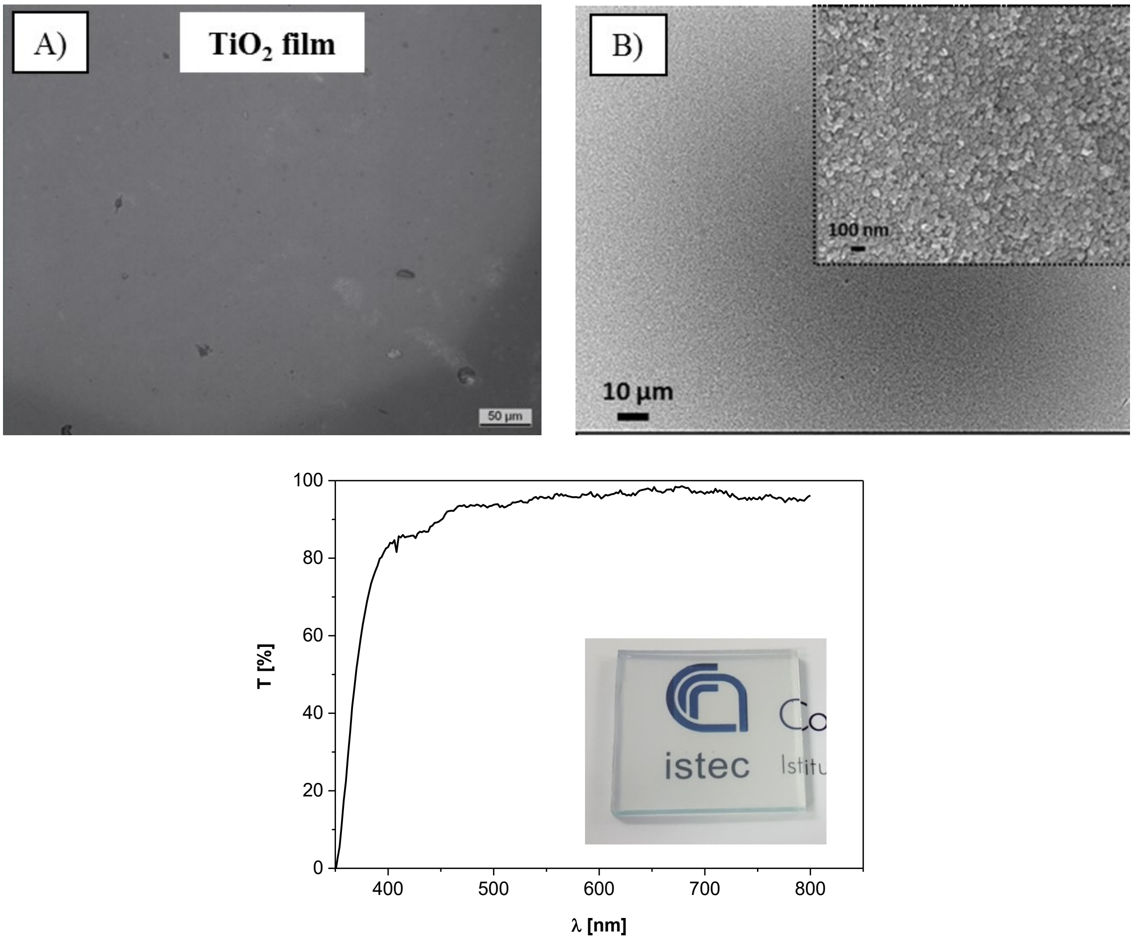

Figure 4.7. A) Optical and B) FE-SEM images of the SY-S4 sample and the relative transmittance spectrum; SY-S4 photoanode is shown in the inset image

Figure 4.7 showed a definite improving in the coverage due to the augmented amount of suspension. The Ra value is dramatically reduced to 9.4 ± 1.2 µm indicating a very smooth surface as confirmed by the optical and SEM images (Figure 4.7 A and B); very high transparency is confirmed by a T% of about 95% at 525 nm. At higher magnification, highly porous microstructure is showed with a mean pore diameter around 20 nm. This is a key property for a suitable DSC photoanode as the high transparency and the proper thickness. The latter is investigated through interferometry as shown in Figure 4.8.

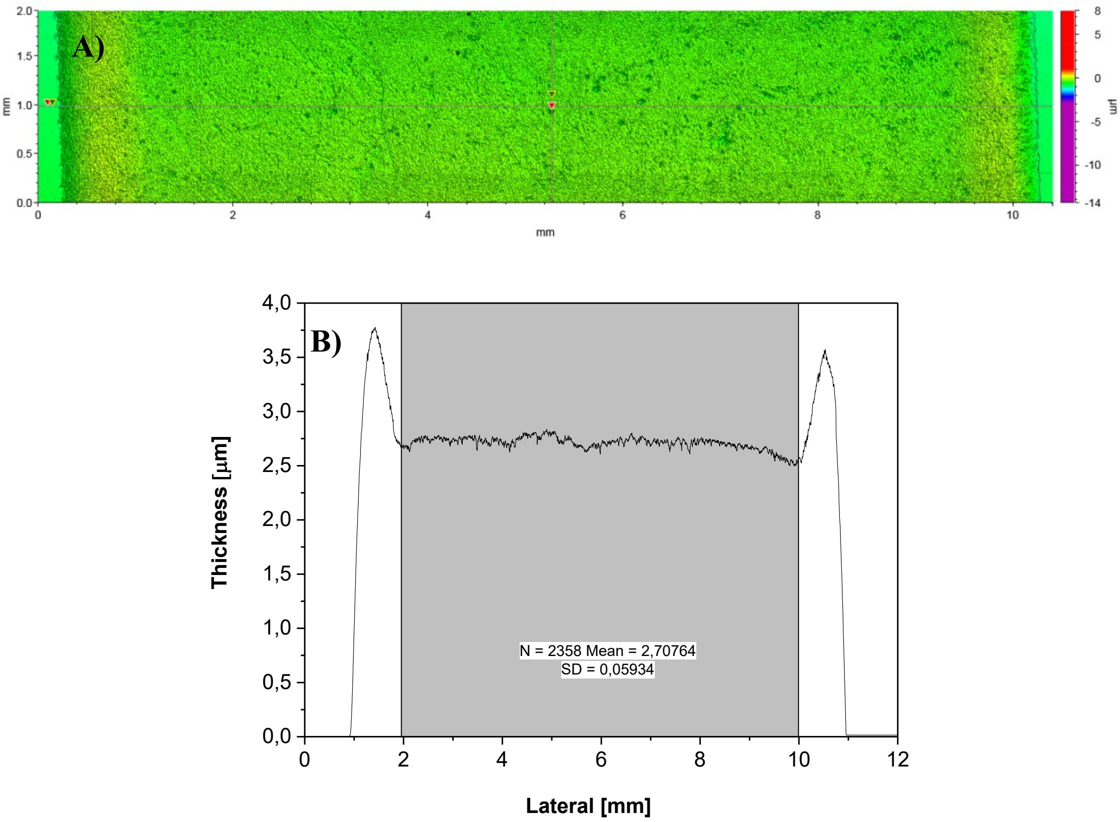

Figure 4.8. A) 2D image of the investigated area and B) X-axis profile of the sprayed film collected along the center of the deposition

The obtained profile (Figure 4.8 B) shows two sharp peaks at the deposition edge ascribed to the presence of a paper mask around the active area. During the spray, the carrier gas strongly pushes the suspension onto the substrate consequently the colloidal TiO_2 tends to flow to the edge of the deposition hitting the mask and thus creating the observed “horn-like” profile. When the edges are excluded from the measured area, the film is very homogeneous with a mean thickness of 2.71 ± 0.06 µm.

The film obtained with the highest number of deposition cycles, distance from the substrate and material flux possessed the desired microstructure, relative transparency and thickness.

4.4 Dye-adsorption tests of the optimized sprayed films

The identification of the best set of parameters to obtain the most suitable sprayed film was the first step to obtained an engineered photoanode for DSC. For the sake of comparison anyway, its dye adsorption capability was considered. This analysis is a useful “tool” to evaluate the dye-loading attitude of a semiconductor film. The capability of adsorbing high amounts of sensitizer is one of the main requisites for a semiconductor oxide layer to be used as DSC photoanode. This property was quantified sensitizing the sample for 20 hours with a 0.3 mM ethanolic solution of the N719 dye and then desorbing the latter from the film surface using a 0.1 M NaOH aqueous solution.

Figure 4.9. SY-S4 sample sensitized for 20h with a 0.3 mM alcoholic solution of N719

The sprayed film (with an active area of 1 cm^2) adsorbed a higher amount of sensitizer (Figure 4.9), 3.78(±0.011)$\times10^{-8}$ mol/cm^2, than a common screen-printed film with comparable area and thickness (2.5-2.9$\times10^{-8}$ mol/cm^2). This is probably due to the high mesoporosity (according to literature, $\varnothing_{pore}$ 2-50 nm) of the former if compared with the scree-printed film microstructure (Figure 4.10 A) that is mainly represented by big pores close to 100 nm or even more higher. On the other hand, the sprayed film (Figure 4.10 B) shows pores dimensions ranging from few nanometers up to 30 nm that are homogeneously distributed on the whole surface. Both these aspects are responsible for an improved dye loading.

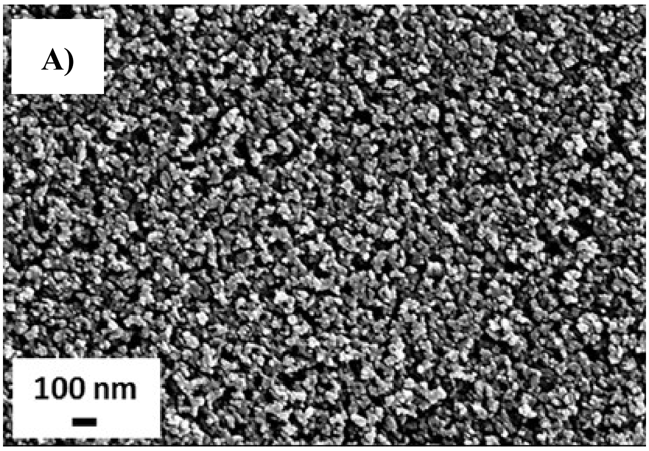

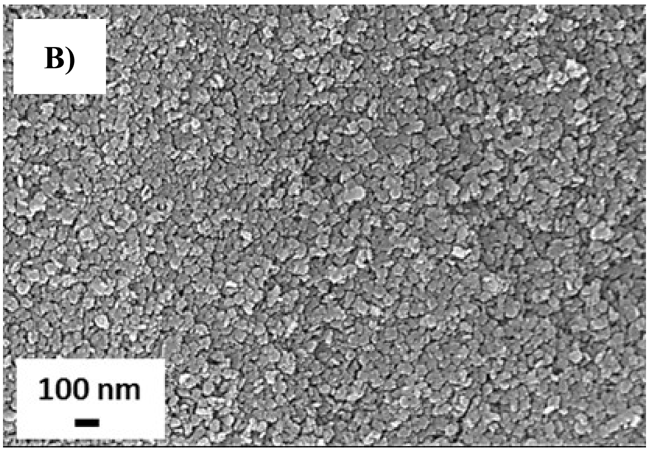

Figure 4.10. FE-SEM images of a) a common screen-printed TiO_2 film and b) the one (SY-S4 sample) produced by spray

The sensitized film (Figure 4.9) was then used to build a complete DSC device and to evaluate the relative photovoltaic parameters and IPCE. EIS analysis were also performed in order to investigate the interfacial charge transfer processes involved. All the acquired data and their discussion will be presented afterward in a dedicated paragraph at the end of the micro-extrusion part, to clearly show the influence of the 3D structures on the DSC performance.

4.5 Powder-based micro-extrusion ink formulation

As already mentioned in the thesis Introduction, the randomly porous structure of TiO_2 electrode gives rise to several undesired characteristics. These include low conductivity [8] and reduced access for the dye and electrolyte to the entire film surface [9-11]. Thus, techniques for fabricating large surface area TiO_2 electrodes with good conductivity and a higher degree of order within the porous network are of great interest to the DSC community. Tridimensional porous structures can satisfy both these requirements principally assuring high-level of order and suitable porosity; in particular, elongated structures such as columns, micro-pillars, etc., can promote the electrons flow towards the FTO substrate reducing the recombination phenomena. Thus, 3D photonoade designs based on microstructured architectures could potentially increase the electrons collection and consequently improve the DSC efficiency.

To date, in the electronics field, such architectures have been produced by conventional photolithography [12] a microfabrication process that uses light to transfer a geometric pattern from a photomask to a light-sensitive chemical phoresist on the substrate. Interesting alternatives are the additive manufacturing (AM) techiniques, like stereolitography (SLA), material jetting (based on DoD inkjet) and micro-extrusion (see Chapter 2, section 2.4); the first one allows to produce tridimensional objects with high resolution but the UV-curable resins used to create them are expansive and often toxic. Material jetting is the optimal solution to create high-aspect ratio 3D architectures thanks to an extremely accurate material deposition. However, it is a quite sensitive and complex technique (see Chapter 2, section 2.4.7) that will be later developed and discussed in a separated section of this Chapter. Micro-extrusion extrudes aqueous low-organic binder dispersion, containing up to 60 vol.% of ceramic powders; no particular conditions or equipment are needed and depending on the employed nozzle, features with good aspect ratio or micrometric details are reproduced. In this study, the production of coarse micro-pillars using micro-extrusion is investigated; due to some experimental limitations mainly connected to the gap between the smallest available nozzle (50 μm), and the target pillars dimensions (mean height 10 - 15 μm), in this phase the AM technique was used to build bigger structures than desired. The primary objective is to evaluate the influence of a well-ordered microstructure and the pillars dimensions on the electrochemical and photovoltaic properties of DSCs. The aim is to demonstrate their positive impact on the cell performance laying, in this way, the foundations for more fine 3D pillars produced using the inkjet technique (next section of "Results and discussion").

To print high-aspect ratio (h/w, where h is the height and w is the width of the pillar) electrode architectures, the composition and rheology of each ink must be optimized to ensure reliable flow through the nozzles and to provide the structural integrity needed to withstand drying and sintering without defects (e.g. cracks or delamination).

For this study, the first approach has envisaged the formulation of a semiconductor powder-based ink prepared following indications coming from previous experiences from ISTEC. In more detail, the starting composition of the first micro-extrusion ink, named ECO_1, is reported in Table V.

Table V. Starting formulation of ECO_1 ink

Material	Function	Wt.%	Vol.%
TiO_2 (P25, Degussa)	Active phase (solid fraction)	20.43	5.97
H_2O (drops of NH_4OH)	Solvent	65.85	80.32
Duramax D3005	Dispersant	0.34	0.32
Ethylene glycol	Humectant/Drying agent	13.39	13.39

As reported in the experimental section (Chapter 3, section 3.4.2) this ink was initially prepared using a mechanical stirring process (by using a vertical shovel) to break-down the particle agglomerates and obtain a well-dispersed suspension. The obtained mix showed some macro-aggregates potentially detrimental for the micro-extrusion process. It was therefore necessary to consider a different mixing technique. Among different available methodologies the attention was focused on the traditional ball milling and the ultrasonic horn.

4.5.1 Milling processes

The adopted experimental conditions for the ball milling process (BM) and the ultrasonic horn (USH) are summarized in Tale VI where the results of the relative DLS measurements are indicated as well.

Table VI. DSL data for the ECO_1 ink

Sample	Exp. conditions	Z-Ave [nm]	PDI
ECO_1	Vertical shovel, at 500 rpm for 1h	600.8 ± 5.1	0.402 ± 0.020
ECO_1 BM	Grinding media with a diameter of 1 mm, at 500 rpm for 24h	357.6 ± 7.9	0.238 ± 0.034
ECO_1 USH [13]	Frequency of 20 kHz with 40% of amplitude, cycle of 45 minutes (10 s pulse followed by a 10 s pause)	383.3 ± 9.0	0.332 ± 0.033

DLS data show that an effective reduction of the Z-Ave is reached for both the samples, going from an initial value of 600 nm for ECO_1 down to 358 nm using the ball milling process. The ultrasonic treatment seems to be less performing, however is important to consider that this treatment is applied for less than one hour in comparison to the 24 hours ball milling process. The lower treatment time is consider very important and for this reason the USH was considered as preferred milling process for the subsequent samples.

4.5.2 Binder composition and effect on the ink rheology

The ink formulation requires careful optimization of all the components to build micro-pillars. The main attention should however be devoted to the binder as it fundamental for depositions The role of the binder is to create a tridimensional polymeric network that includes the ceramic particles to form a permanent 3D solid structure.

Since the binder is the main responsible for the rheological properties of an ink, the first study regarded the use of copolymers blends prepared by solution method [14,15] and their effect on the inks viscosity and mechanical moduli. In recent years, copolymers and their blends have attracted the attention of material researchers to obtain intermediate properties (attributed to the molecular motions in their amorphous phases) with respect to homo-polymers for some specific functions.

In this work, two different celluloses, hydroxypropyl cellulose (HPC) and hydroxyethylcellulose (HEC) were mixed in different ratios. The resultant copolymers are water-soluble that thicken and exhibit pseudoplastic behavior in solution; moreover, they are low-toxic and environmental friendly. The main difference between HPC and

HEC is the absence of a methyl group in HEC. This lack allows the formation of a more rigid and tougher gel with superior compressive and flexural strengths because the cellulosic OH groups are freer to interact between each other (making O-H-O bonds) due to the lower steric hindrance of the chains.

Three alternative blends (HPC:HEC) were considered: 60:40, 50:50 and 40:60 respectively. The corresponding inks were called ECO_1_60:40, ECO_1_50:50 and ECO_1_40:60. All the new inks considered the initial formulation of ink ECO_1was kept constant while the total amount of binder was varied in the range between 3.5 and 4.1 wt.% depending on the considered mixture (Table VII).

Table VII. ECO_1 inks with different ratio of cellulosic binders

Material	**HPC:HEC 60:40**		**HPC:HEC 50:50**		**HPC:HEC 40:60**	
	Wt.%	**Vol.%**	**Wt.%**	**Vol.%**	**Wt.%**	**Vol.%**
TiO_2 (P25, Degussa)	10.74	3.01	10.74	3.01	10.74	3.01
*H_2O (drops of NH_4OH)	77.93	86.72	78.24	87.03	78.56	87.33
Duramax D3005	0.18	0.16	0.18	0.16	0.18	0.16
Ethylene glycol	7.04	6.76	7.04	6.76	7.04	6.76
*Celluloses	4.11	3.34	3.80	3.04	3.48	2.74

*The binders were added to the suspension in form of aqueous solutions of HPC 10 wt.% and HEC 6 wt.% respectively; accordingly, their overall quantity and the corresponding solvent amount slightly change.

Flow behavior and viscoelasticity of the inks were analyzed on the basis of the transient network theory (TNT) [16]. According to this model, the rheological properties of the inks are originated by the tridimensional network that is formed from the interaction between the polymeric chains of the binders and the ceramic particles, which act as cross-linkers. The flow curves of the obtained inks are compared in Figure 4.11.

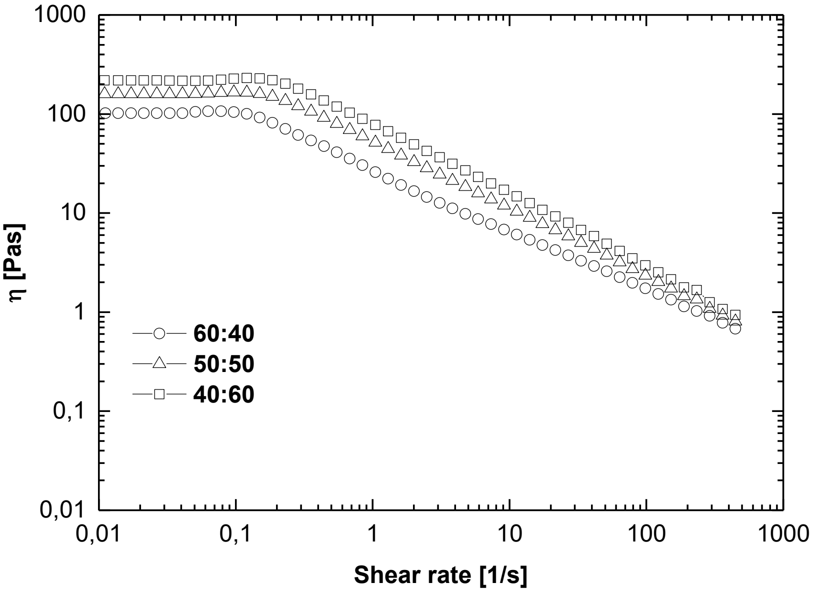

Figure 4.11. Effect of different binder blends on the viscosity of the ink ECO_1 series

The flow curves show the typical pseudoplastic behavior of the inks, with viscosity decreasing with an increasing of the shear rate. This effect ensures printability at low pressures, typical of the shear forces imparted to the ink inside of the nozzle. This comparison points out an evident difference induced by the increasing HEC concentration. The viscosity of each of the three new inks in fact does not vary significantly until a shear rate of about 0.3 s^{-1} is reached (Newtonian plateau). In addition, for all the tested formulations, the viscosities are directly proportional with the HEC concentration, in particular each increase in HEC basically corresponds to an increase of almost 100 Pas of viscosity. Moreover, they show good stability at low shear rate. According to the TNT the Newtonian plateau corresponds to the stretching of the cellulosic chains, which does not affect the value of viscosity. The transition to the pseudoplastic behaviour corresponds to the breakage of the particle agglomerates, which fractures the network and therefore reduces the viscosity. In this terms, an increased length of the Newtonian plateau, as in the case of ECO_1_40:60, may be indicative of a network that is not easily fractured or, if fractured, it could be rapidly re-formed due to the high number of possible contact points between TiO_2 and the celluloses. This behaviour suggests that the system is stable during the analyses (and the deposition), or that it can instantly recover after a fracture or a perturbation restoring the network.

Another significant difference arises from the viscoelasticity analysis of the most viscous systems, the most promising ones (50:50 and 40:60). Figure 4.12 reports the comparison between the elastic (G') and the viscous modulus (G'').

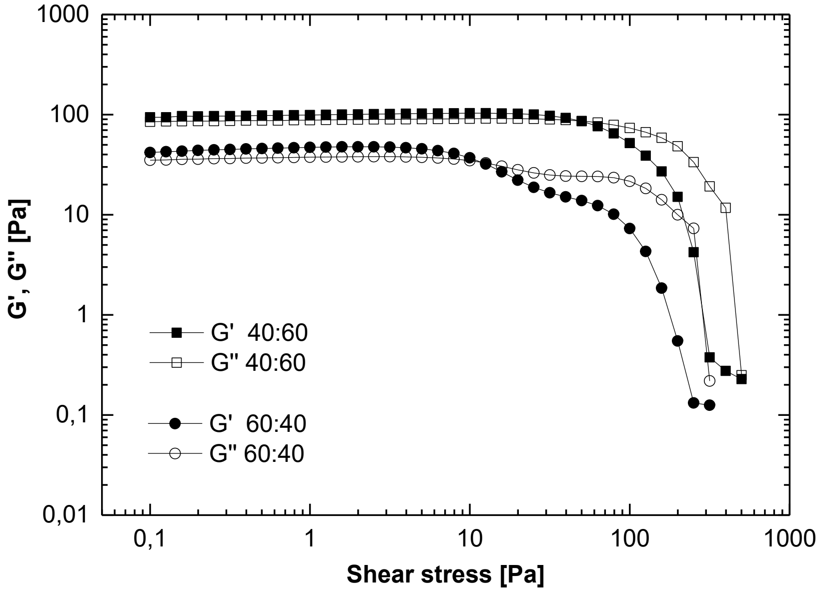

Figure 4.12. Effect of different binder blends on the viscoelasticity of the ink ECO_1 series

The viscoelasticity analyses exhibit almost superimposable curves, in which G' prevails on G'' in the whole range of shear strain investigated; this trend is typical of systems forming a well-structured 3D network. When the concentration of HEC is increased, G' prevails on G'' up to a yield stress (τ_y) value of about ~10, ~25 and ~60 Pa, for the samples ECO_1_60:40, 50:50 and 40:60 respectively. Moreover, both the moduli increase proportionally to the amount of HEC and the linearity of the curves increases. These results, as the ones obtained from the flow curves, are due to a proportional enhancement of the rigidity of the network induced by the increased amount of HEC. Finally, their rheological behavior is in good agreement with those reported for other inks designed for 3D filamentary printing technique [17]. The absolute values of viscosity of all the systems are however at least one order of magnitude lower to what needed to properly design tridimensional objects.

4.5.3 Powder loading increase

Considering the amount of organics already used for the ink ECO_1 formulations (around 11.5 wt.%), it is not recommended to increase the binder content to limit distortions or other defects during the thermal treatments. In order to reach the desired viscosity, a simultaneous increasing of the solid loading and a reduction of the solvent amount, was investigated. Thus, the semiconductor powder load was augmented up to 38 wt.%. The starting formulation of the ECO_2 ink is reported in Table VIII.

Table VIII. Starting formulation of ECO_2 ink

Material	Function	Wt.%	Vol.%
TiO_2 (P25, Degussa)	Active phase (solid fraction)	38.00	13.27
H_2O (drops of NH_4OH)	Solvent	48.15	70.21
Duramax D3005	Dispersant	0.63	0.72
Ethylene glycol	Humectant/Drying agent	13.22	15.80

Thanks to the previous experience also this sample was ultrasonically treated using the same conditions reported in Table VI. Unfortunately, in this case, due to the increased solid loading this method was totally ineffective. In this system the particles motion is in fact almost negligible while the suspension temperature is seriously augmented by the treatment creating undesired evaporation phenomena. Alternative mixing processes were then investigated, in particular using an innovative planetary centrifugal mixer (Thinky, Japan). This machine uses a mechanism where the container holding the material revolves clockwise and the container itself rotates counter-clockwise. The centrifugal force (400G) produced by the high-speed rotation and revolution depresses the material in the container, and generates vertical spiral convection. This vertical spiral convection is continuously generated to blend and disperse the materials evenly.

This apparatus is well-known in specialist literature [18] due to its capability to enable simultaneous processing of mixing, dispersion and deaeration of high-viscosity materials and therefore potentially suitable for the ECO_2 ink.

4.5.4 Thinky cycle optimization

The effect of different ratio of HPC e HEC was considered also for the ink with an higher powder loading (ECO_2) (Table IX).

Table IX. ECO_2 inks with different ratio of cellulosic binders

Material	HPC:HEC 60:40		HPC:HEC 50:50		HPC:HEC 40:60	
	Wt.%	**Vol.%**	**Wt.%**	**Vol.%**	**Wt.%**	**Vol.%**
TiO_2 (P25, Degussa)	19.99	6.11	19.99	6.10	19.99	6.10
H_2O (drops of NH_4OH)	67.99	81.94	69.41	83.46	69.89	83.94
Duramax D3005	0.33	0.33	0.33	0.33	0.33	0.33
Ethylene glycol	6.95	7.28	6.95	7.27	6.95	7.26
Celluloses	4.74	4.34	3.32	2.83	2.84	2.37

The mixing procedure was optimized on ECO_2_40:60. This is in fact the highest viscous and consequently the most difficult ink to be homogenized. All the trials to produce micro-extrusion suitable inks were therefore carried out with this system and then the ideal conditions were transferred to the other ones.

The optimization of the Thinky cycle was obtained through a step-by-step procedure that essentially consists in treating, at specific conditions, the mixture of raw materials and then checking for the presence of aggregates. Accurate rheological analysis were also used to assess the as-formulated inks. Different sets of Thinky parameters were investigated (Table X) starting from literature indications [18,19] used for inks comparable with the ECO_2_40:60 one. In particular the mixing mode, which has high speed of rotation and revolution, was firstly applied to the ink varying both its velocity and duration. Then, the deaeration step (similar to a simple centrifuge action) necessary to remove any remaining air was also introduced.

Table X. Thinky cycles applied to the ECO_2_40:60 ink

Cycle Nr.	Mixing		Deaeration		Note
	rpm	t [s]	rpm	t [s]	
1	900	30	/	/	Several big aggregates, the TiO_2 powder was not completely wetted.
2	900	90	/	/	Aggregates dimensions were slightly reduced and the semiconductor powder was wetted. Additionally, some bubbles appeared on the ink surface.
3	900	180	/	/	Doubling the mixing time, a strong decrease of the aggregates in terms of number and dimension was achieved. Coincidently, the amount of air bubbles was increased.
4	900	180	900	60	Few and tiny aggregates were still present but no more bubbles were identified
5	900	360	900	60	A very smooth high-solid loaded ink was obtained, bubbles were removed as well as the aggregates thanks to a more long-lasting mixing step that lightly increased the ink temperature.

Cycle Nr. 5 was considered the optimal one and was therefore applied to all the subsequent formulations. The application of both mixing and degassing steps lead to the best formulations regardless the cellulose blend amount.

As previously mentioned, the correct inks homogenization was also evaluated through rheological analysis. The viscosity (Figure 4.13) and viscoelasticity curves (Figure 4.14) of the obtained inks are shown below.

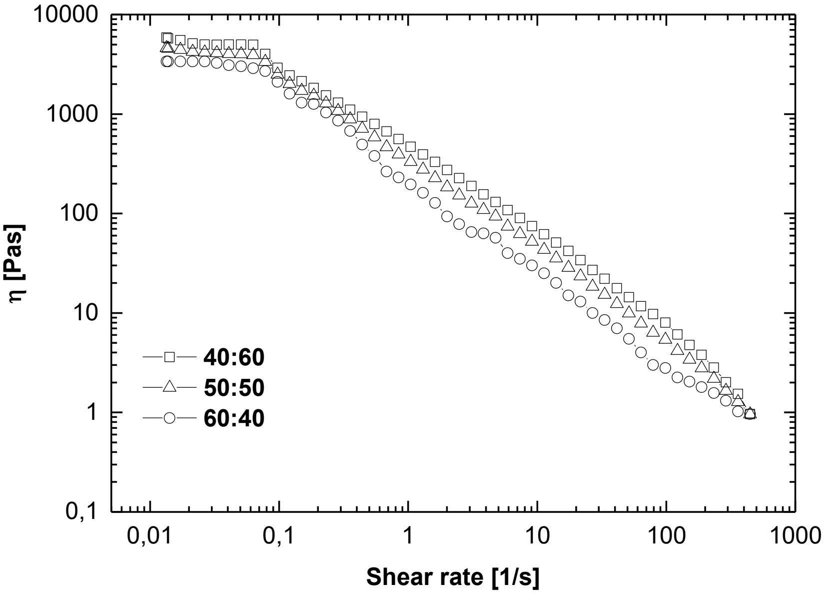

Figure 4.13. Effect of different binder blends on the viscosity of the ink ECO_2 series

The viscosities decrease with an increasing of the shear rate indicating an appropriate pseudoplastic behavior. Also in this case, the comparison highlights an evident increase of η directly proportional with the HEC concentration. In particular each increase in HEC corresponds to a viscosity growth of almost 1000 Pas reaching values up to 5000 Pas for the highest viscous system (40:60). The comparison with the equivalent ECO_1 ink (Figure 4.11) clearly shows how the increased solid loading leads to viscosities more suitable for micro-extrusion processes. Moreover, the ECO_2_50:50 and 40:60 show good stability in the whole range of shear rate investigated while the 60:40 ink exhibits a feeble instability. The length of the Newtonian plateau is similar for all the formulations suggesting stable three-dimensional networks that are not easily fractured or that they recover the structure when stressed. To further support this assumption, inks viscoelasticity curves of the most stable systems are reported in Figure 4.14.

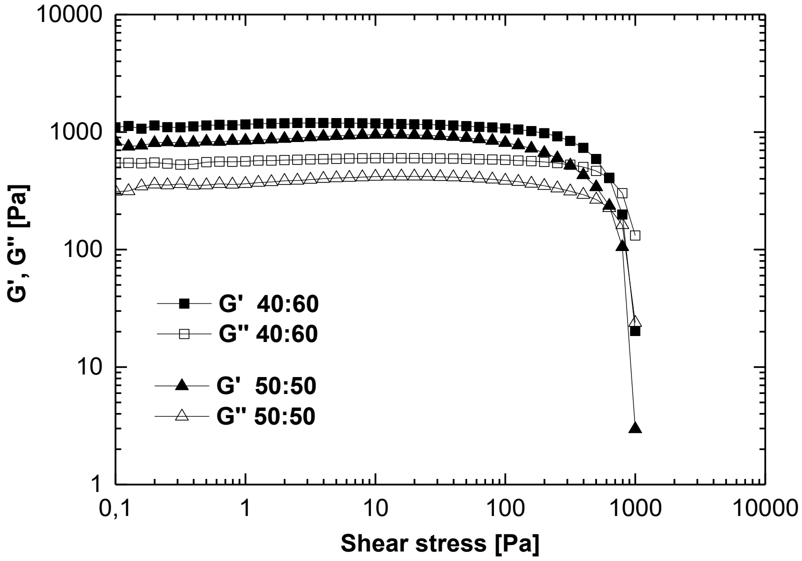

Figure 4.14. Effect of different binder blends on the viscoelasticity of the ink ECO_2 series

The viscoelasticity analyses exhibit for both the inks an elastic modulus higher than the viscous one in the whole range of shear strain investigated which is indicative of more solid-like behavior. The difference between G' and G'' is enlarged in these cases. These evidences suggest that the increased number of TiO_2 particles interacting with the binder more frequently than before, lead to a structuring and thickening of the systems, thus increasing the suspensions viscosities as well as their elasticity. Even if the concentration of HEC is increased, the τ_y values are comparable for each system around 700 Pa. This value is however, impressively higher than the one measured for ECO_1 inks (ranging between 10 to 60 Pa). In addition, both the moduli increase proportionally to the amount of HEC. This result, as the ones obtained from flow curves, is due to a proportional enhancement of the rigidity of the network induced by the increased amount of HEC that is able to create a stiff polymer network eased from an optimal arrangements of its branched chains. The rheological data therefore indicate that a Thinky cycle of strong de-agglomeration and deaeration is fundamental to obtain inks with suitable rheological characteristics for the micro-extrusion. The ECO_2_40:60 formulation was therefore chosen for preliminary deposition tests.

4.5.5 Micro-extrusion deposition tests

Generally speaking, the micro-extrusion process consists in forcing a ink through a nozzle of a defined diameter, using a rotating screw. Therefore, smooth inks composed of well-dispersed particles are mandatory to obtain high-quality depositions to avoid issues like discontinuous filament flow and even worse, the nozzle clogging. The nozzle is clearly the most sensitive part of the apparatus determining the deposition outcomes. Taking this into account, a first experimental indication of the proper extrudability of an ink is its correct flowing through the desired nozzle.

The ECO_2_60:40 was therefore directly loaded inside a syringe-like cartridge with a moveable diaphragm controlled by compressed air. Different plastic nozzles were tried to evaluate the ink flowing. A general view of the apparatus is shown in Figure 4.15.

Figure 4.15. Testing apparatus to evaluate the ECO_2_40:60 flow

The first tests were performed using a 410 and 250 μm diameter nozzles: even if these particular nozzles are too big for the application considered in this work, they were used to detect, if present, residual ink aggregates of dimensions comparable with their diameter. With both systems, a pressure of 5 bar was able to produce an extremely regular filament flow for multiple cycles. The ECO_2_60:40 formulation was then loaded in the micro-extruder for producing simple high-quality extruded structures with dimensions comparable with the nozzle diameter. Several experiments were performed trying different parameters (reported in Table XI and accurately described in Chapter 3, section 3.6) combinations to achieve the target. In particular, the attention was focused on: (i) the nozzle diameter that strongly influences the single layer quality (small diameter leads to thinner layers), (ii) the extrusion modality, selecting between the quantity program or the pulse one in order to set the ink amount per dosing or just the material flow, (iii) the deposition time and (iv) the supply advance time that is a standard procedure to homogenize the material flow avoiding discontinuities during the deposition process. The most representative depositions are shown in Figure 4.16 while all the remaining are listed in Appendix 2. The deposition quality was evaluated in terms of ink shape retaining.

Table XI. Representative micro-extrusion tests performed with ECO_2_40:60 ink to realize 3 cm length straight lines

Depos. Nr.	**Nozzle Ø [µm]**	**Extrusion mode**	**Vol. [ml]**	**Flow [ml/min]**	**Z [mm]**	**Depos. time [s]**	**Supply advance [s]**	**Deposition speed [mm/s]**
23*	1200	Quantity	0.055	1.750	0.75	2.00	0.65	15
42	410	Quantity	0.015	1.750	1	0.50	0.75	60
44	410	Pulse	/	1.700	1	0.50	0.75	60
50	410	Pulse	/	1.475	1	0.33	1.40	90

*this trial is listed in the table and shown in Figure 4.16 just to strongly emphasize the deposition process improvements and to appreciate at the macroscale level the ink/substrate interaction.

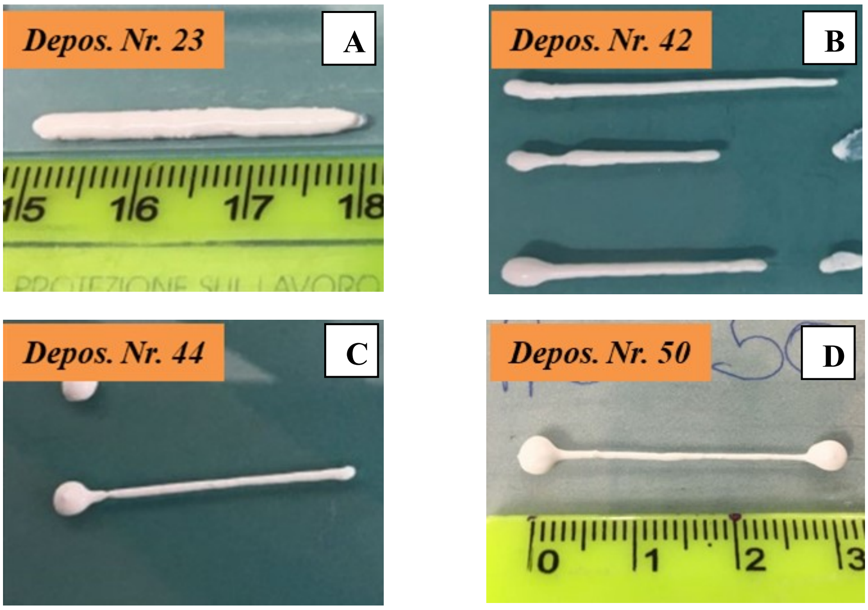

Figure 4.16. Representative micro-extrusion depositions of 3 cm length straight lines using the ECO_2_40:60 ink

The adopted strategy used to optimize the micro-extrusion process was based on flow and deposition time reductions, coupled with an increase of both the supply advance time and the deposition speed. Carefully acting on these parameters the deposition quality improves going from deposition Nr. 23 up to the 50th (as reported in Figure 4.16). The first deposition (Figure 4.16 A), showed a strong time-depending behaviour that means an unsuitable ink thixotropy. The latter represents the capability of a fluid of recovering its initial value of viscosity after the application of a shear stress. A slow recovery of viscosity in fact leads to a loss of printing definition. This specific property is ascribed to the binder system, whose polymeric chains are able to stretch with the applied shear stress, and recover the initial coiled and structured conformation after the deposition. As a consequence, the width of the line obtained with the 1200 μm nozzle was more than doubled after few minutes. The reduction of the nozzle diameter leads (Figure 4.16 B) as expected to a drastic reduction in the line width also related to a strong volume lowering and an increased deposition speed. Changing the extrusion mode to the Pulse one, more accurate because independent from the material volume, and slightly increase both the deposition and the supply advance time, straight lines (Figure 4.16 C) with width that are 190% of the nozzle diameter were produced. Finally, concretely reducing the flow and the deposition time while increasing the supply advance and the deposition speed a thin homogeneous line was obtained (Figure 4.16 D). In this case the structure was able to reasonably retain its initial dimensions (width of the deposited line 150% of the nozzle diameter). Further laboratory tests performed reducing the nozzle diameter down-to 250, 200 and 50 μm were extremely difficult and, with the smallest one, totally unfruitful. During the depositions the material flowed outside discontinuously and sometimes following random trajectories. These phenomena might be due to the presence of residual soft agglomerates of TiO_2/cellulose that partially occlude the nozzle. This behaviour is obviously detrimental for the deposition of high-aspect ratio 3D structures, especially in the case of DSCs which require accurate deposition to produce high efficiency devices. For all these reasons, it was necessary to consider new formulations with suitable rheological properties and above all, the total absence of residual agglomerates. The experience gained using colloidal suspensions in the spray coating process has been crucial at this stage: being the aqueous suspensions used for the spray already stabilized, they could be used also for the micro-extrusion process.

4.6 Colloidal TiO_2-based micro-extrusion ink formulation

Among the different available products, CristalACTiV^{TM} S5-300B was selected thanks to its TiO_2 content (18 wt.%) and pH value (~12) that reduces potential corrosion issues. Three different families of inks were prepared with growing cellulose blend content starting from 4.70 up to 6.50 wt.% with different ratio between the HPC e HEC. Each ink was homogenized using the best Thinky cycle. Such a wide spectrum of compositions allowed to identify a formulation suitable for the formation of micro-pillars by micro-extrusion. The ink with the highest celluloses amount (6.50 wt.%) was abandoned as a consequence of homogenization issues linked to the solubility limit of the binders. For this reason, this system was not further considered. The starting compositions of the new set of inks, named ECO_300B_4.70 and ECO_300B_5.60, are reported in Table XII and XIII respectively.

Table XII. ECO-300B_4.70 inks with different ratio of cellulosic binders

Material	HPC:HEC 60:40		HPC:HEC 50:50		HPC:HEC 40:60	
	Wt.%	**Vol.%**	**Wt.%**	**Vol.%**	**Wt.%**	**Vol.%**
TiO_2	16.04	4.88	16.04	4.89	16.04	4.89
H_2O	73.07	84.54	73.07	84.57	73.07	84.59
Ethylene glycol	6.19	6.46	6.19	6.46	6.19	6.46
Celluloses	4.70	4.12	4.70	4.09	4.70	4.06

Table XIII. ECO-300B_5.60 inks with different ratio of cellulosic binders

Material	HPC:HEC 60:40		HPC:HEC 50:50		HPC:HEC 40:60	
	Wt.%	**Vol.%**	**Wt.%**	**Vol.%**	**Wt.%**	**Vol.%**
TiO_2	15.88	4.84	15.88	4.84	15.88	4.85
H_2O	72.35	83.81	72.35	83.84	72.35	83.88
Ethylene glycol	6.16	6.43	6.16	6.43	6.16	6.44
Celluloses	5.60	4.91	5.60	4.88	5.60	4.84

The Thinky treatment (Table X, Cycle Nr.5) was important to obtain extremely homogeneous pastes, free from agglomerates and air bubbles. To assess their potential for filamentary deposition, these samples were characterized in terms of viscosity (Figure 4.17) and viscoelasticity (Figure 4.18).

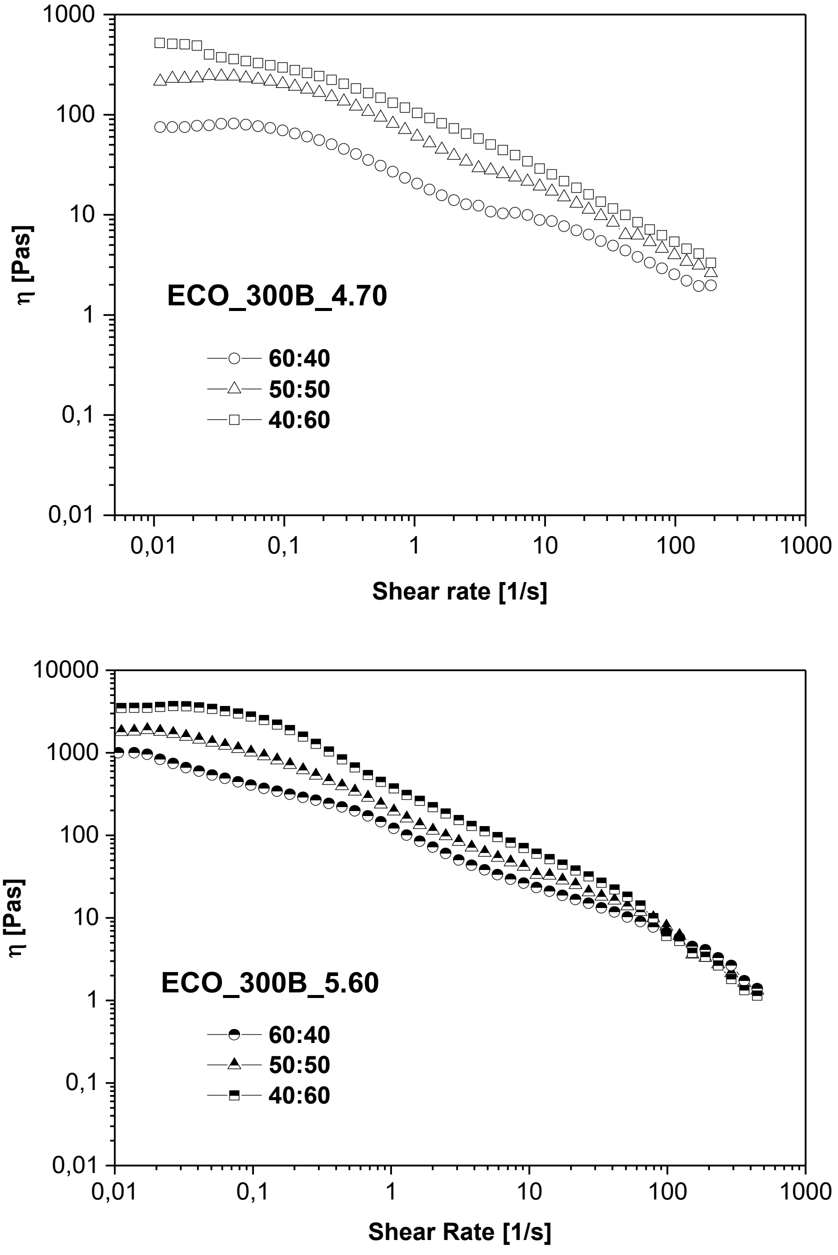

Figure 4.17. Effect of different binder blends on the viscosity of the ECO_300B_4.70 ink series and ECO_300B_5.60 ink series

All the produced inks showed a clear pseudoplastic behavior (Figure 4.17), with viscosity decreasing with an increasing of the shear rate. In the 4.70 wt.% inks series, increasing the HEC concentration causes an increase of viscosity values from 80 up to 500 Pas (40:60) with the Newtonian plateau up to about 0.2 s^{-1}. All the samples showed good stability at low shear rate indication of well-structured systems. The same trend can be observed for the 5.60 wt.% inks series. As expected, also in this series the 40:60 ink showed the widest Newtonian region confirming its higher stability to stresses.

Figure 4.18 reports the comparison between the elastic (G') and the viscous modulus (G'') for all the formulations considered. It is easy to note that, the curves of the ECO_300B_5.60 series show trends almost identical to the ones of the previous inks just shifted at higher values of G', G'' and shear stress as a consequence of the higher binder content. The viscoelasticity analyses exhibit almost superimposable curves for the 4.70 ink family with a maximum of τ_y around 100 Pa for the ink with the 40:60 HPC:HEC ratio. This is an indication of a more pronounced liquid-like ink behavior. Moreover, the linear viscoelasticity zone is more pronounced when a higher HEC content is used. This means a more structured system that is able to tolerate higher stress and is due to the HEC capability to form strong gels.

The moduli gap of the 5.60 series on the other hand, is higher. These results showed, as expected that the systems with a higher amount of binder is much more structured and behave more as a solid than the other ones. The obtained results, as the ones collected from flow curves, are due to a proportional enhancement of the rigidity of the network induced by an increased amount of celluloses in particular HEC.

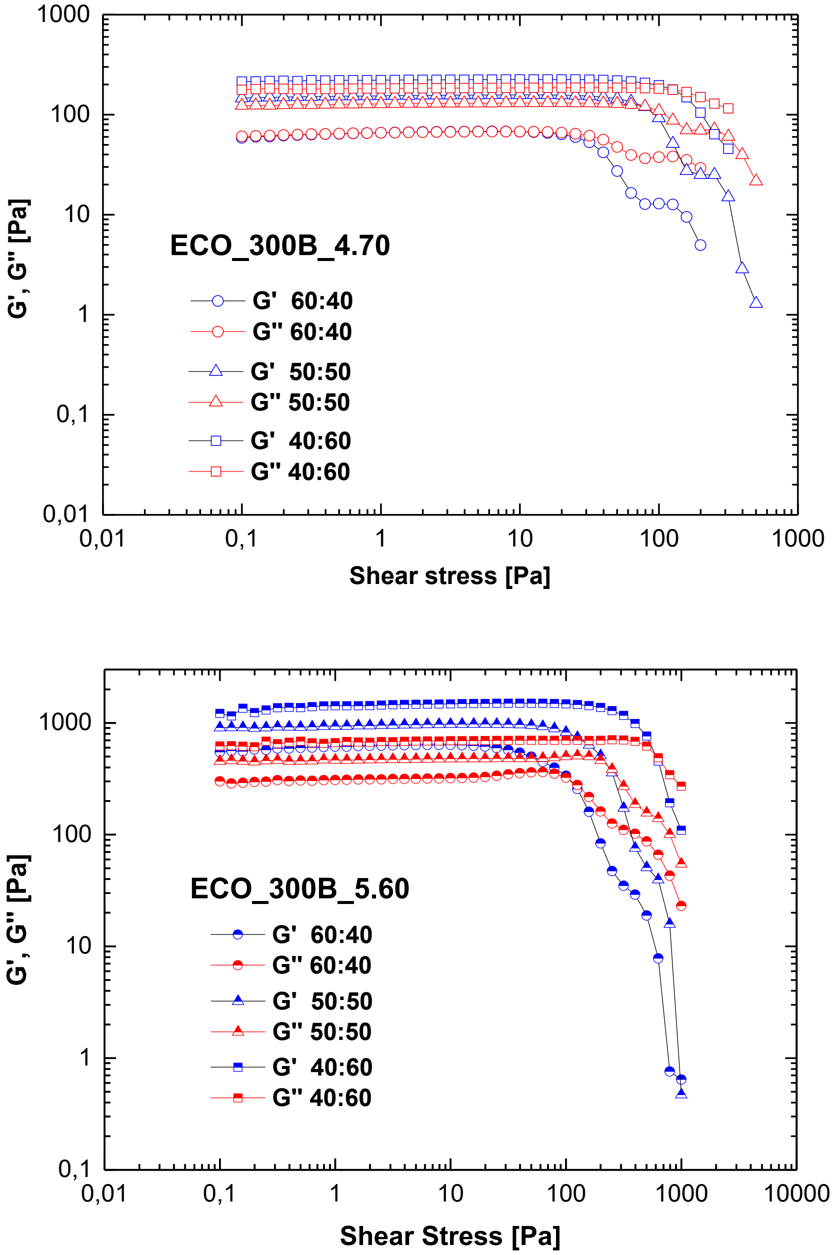

Figure 4.18. Effect of the different binder blends on the viscoelasticity of the ECO_300B_4.70 ink series and ECO_300B_5.60 ink series

In conclusion, the rheological data indicate that the ECO_300B_5.60_40:60 (starting from now indicates as ECO_300B only) ink is the most promising one for the micro-extrusion. This ink shows suitable values of viscosity and mechanical moduli, thus it is identified as optimized formulation for the next deposition tests.

4.6.1 Micro-extrusion deposition tests

As reported before, the syringe-like cartridge (Figure 4.15) was filled with ECO_300B and the ink flow through different plastic nozzles was evaluated. The tests were performed using 250, 200 and 50 µm diameter nozzles obtaining in each case a regular and constant flow. Also with the tiniest nozzle the ink is able to flow freely outside thus, these positive results suggest the possibility to load the ink into the micro-extruder for the deposition process optimization.

The investigated process parameters combinations are reported in Table XIV while the corresponding deposition pictures are collected in Figure 4.19. All the remaining trials and images are listed in Appendix 2. As already described before, the depositions quality was evaluated in terms of the ability to retain the deposition features.

Table XIV. Representative micro-extrusion tests performed with ECO_300B ink to realize 3 cm length straight lines

Depos. Nr.	Nozzle Ø [µm]	Extrusion modality	Vol. [ml]	Flow [ml/min]	Z [mm]	Depos. time [s]	Supply advance [s]	Deposition speed [mm/s]
59	200	Pulse	/	0.950	1	0.50	1.30	60
60	200	Pulse	/	1.500	0.25	0.33	2.00	90
61	250	Pulse	/	1.500	1	0.33	2.00	90

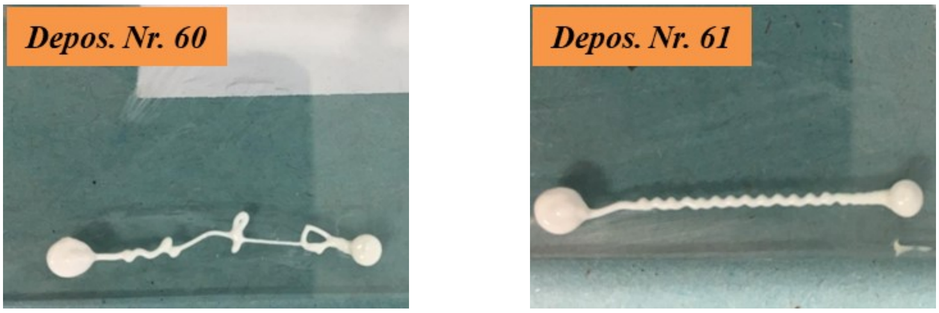

Figure 4.19. Representative micro-extrusion depositions of 3 cm length straight lines using the ECO_300B ink

Figure 4.19 shows two features representative of the all the trials done that are clearly unsatisfactory. They differ just for the value of Z. These results are very different from the samples presented in Figure 4.16. While in the syringe used there, the ink is directly pushed towards the nozzle by compressed air, in the microextruder the material flow is regulated by a rotating screw. The different process of feeding the material to the nozzle plays an important role in the case of ink at high viscosity: in this condition, the rotation screw is not able to correctly transport the ECO_300B ink up to the nozzle tip, probably for irregular sliding effect of the ink on the screw walls and/or values of shear that are not achievable with the available instrumentation. Therefore, instead of using this system, the depositions of TiO_2 pillars were performed with an home-made deposition apparatus (Figure 4.20 A), similar to the one reported in Figure 4.15, in which the syringe-piston system is mounted on a z-axis motion stage while the substrate on a moving x-y stage. The pressure can be fixed and carefully applied to the piston for few seconds to reach a constant ink flow.

The FE-SEM micrographs (Figure 4.20 B and C) of the depositions obtained using the 50 µm nozzle show micro-pillars composed of well-balanced mix of dispersed TiO_2 nanoparticles and pores of about 10-20 nm (Figure 4.20 C), i.e. a microstructure similar to the one of the optimized sprayed films (Figure 4.10). Micro-pillars are formed by (Figure 4.20 B) 300 µm circular bases affected by some peripheral cracks. These are due to a non-optimized drying step after deposition; the phenomenon was eliminated reducing the rate of drying before sintering (Figure 4.20 B).

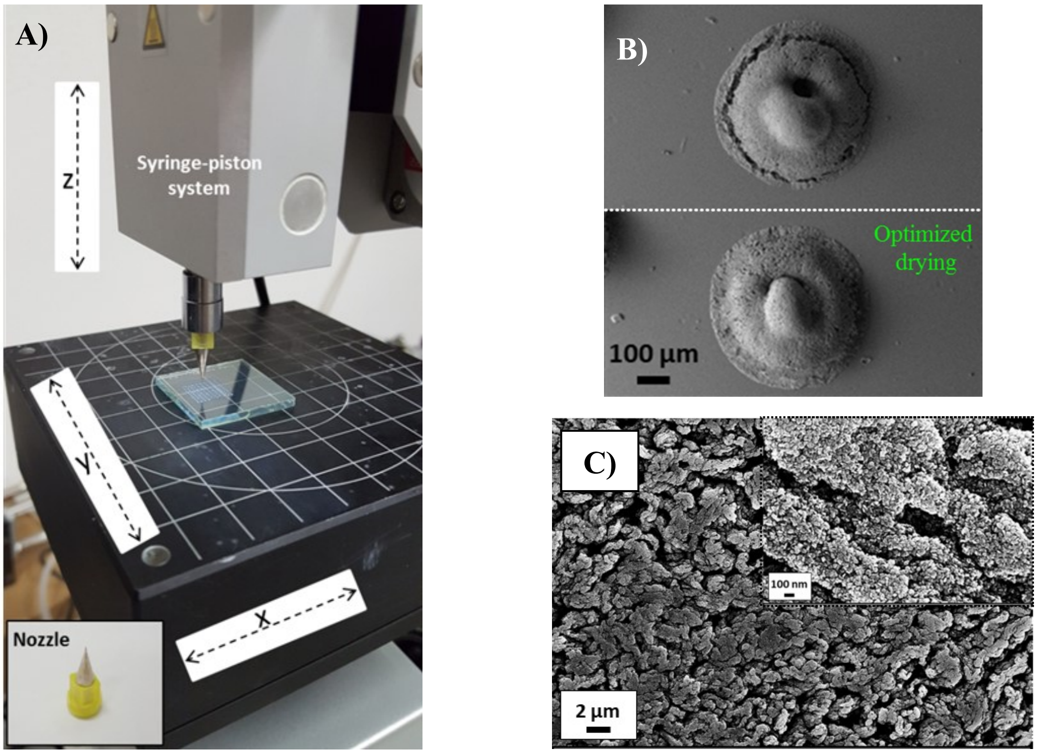

Figure 4.20. A) Home-made deposition apparatus B,C) FE-SEM surface micrographs of the 50 µm nozzle deposited micro-pillars at different magnifications

The 3D images of the optimized micro-pillars, before and after sintering, obtained using both the 200 and 50 µm nozzle are reported in Figure 4.21.

Figure 4.21 A clearly shows a micro-pillar surrounded by some particles that create a ring path. The latter is probably caused by a structure collapse; the solvent separates a bit and tends to drag down some particles forming that kind of “collar” at the pillar base. The as-produced 3D pillars were measured to calculate the relative aspect ratios (Figure 4.22).

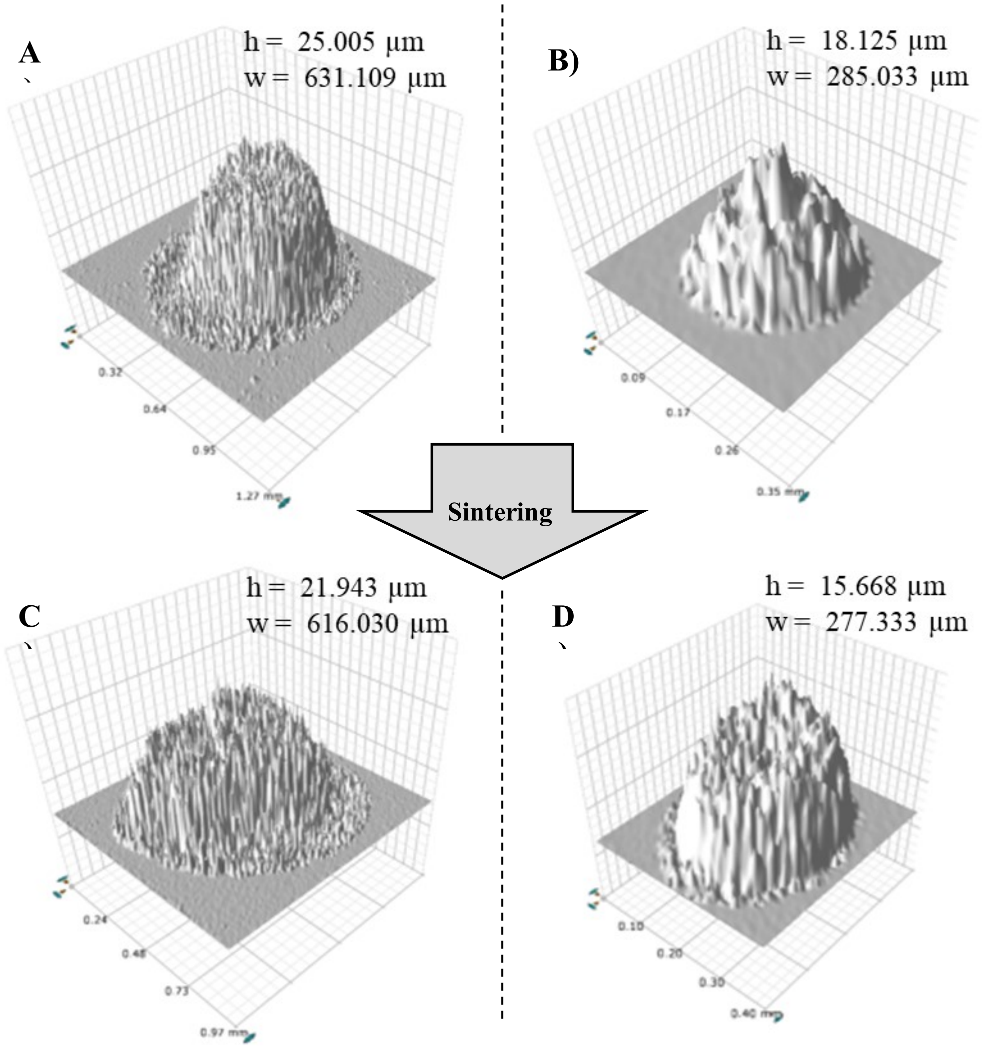

Figure 4.21. 3D reconstructions of the micro-pillars deposited using (A) the 200 and (B) 50 µm before and after the sintering (C and D)

The dimension of each micro-pillars are reported in Figure 4.21. Going from the 200 µm down to the 50 µm nozzle, there is a clear decrease in the width of the pillar while its height remains quite constant. As a consequence of a reduced width the pillars produced with the 50 micron pillars show a higher aspect ratio as reported in Figure 4.22.

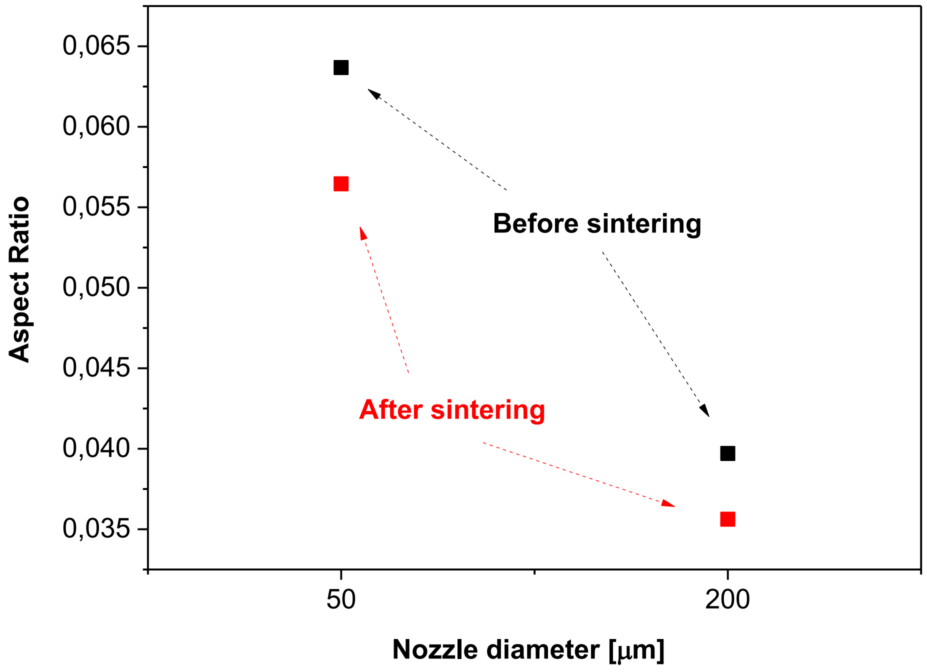

Figure 4.22. Aspect ratio of the produced micro-pillars before and after sintering

The aspect ratio values decrease for both the considered systems; the thermal treatment generates pillar volume contractions. However, along the x and y axes are very limited (almost preserving the pillar widths) due to the high contact surface between each single 3D structure and the underlying mesoporous film. The latter constrains the shrinkage of the pillars that can freely move only along the z axis so predominantly reducing their heights.

Even if the aspect ratio values are lower than the ones commonly reported in literature for high-aspect ratios structures (ranging between 5 and 10) [22] it is important to remember that these results have been obtained deposing one single "dot" of ink on the substrate and slowly moving the nozzle far away from it. This methodology was however considered to prove the effect of a pillar structure (even a coarse one) on the properties of a DSC building the periodic structure represented in Figure 4.23 A e B. The engineered photoanodes (called SY-S4-P50) were therefore used to realize a DSC device.

4.6.2 Photoanodes transmittance and dye-adsorption tests

The engineered photoanode (Figure 4.23 A) transparency was determined and compared with the one of the previously obtained sprayed film.

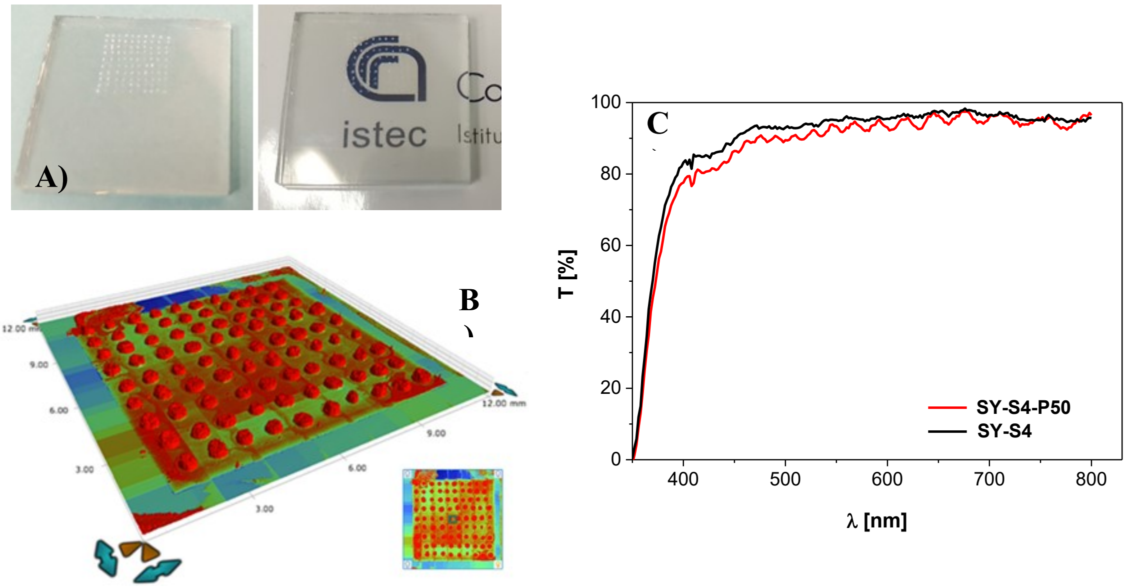

Figure 4.23. A) Images of the SY-S4-P50 photoanode and B) its 3D reconstruction; C) SY-S4 and SY-S4-P50 transmittance spectra comparison

Although the SY-S4-P50 sample is composed by high-thickness 3D structures (Figure 4.23 B) that also means higher amount of semiconductor, the transmittance curves (Figure 4.23 C) show just a slight decrease (about 5% in the visible range) of the overall photoanode transparency indicating low intensity scattering effects due to the presence of micro-pillars. Thus, also from this point of view the developed ink is suitable for their deposition containing well-dispersed particles that faintly interact with the incident radiation. The characteristic shape of the red curve, due to interference fringes presence, is ascribed to the incident radiation/pillar interaction; when the light hits a pillar it finds a greater volume of material to be crossed and consequently its intensity at the detector decreases. This phenomenon take place every time a pillar is hit generating periodically T% decreases during the analysis.

The SY-S4-P50 photoanode was then sensitizied (Figure 4.24) with a 0.3 mM solution of N719 in abs. ethanol. The sensitizer was then desorbed by the semiconductor surface using a 0.1 M NaOH aqueous solution. A dye loading capability of 9.733 (± 0.014) x 10^{-8} mol/cm^2 was found for the engineered sample.

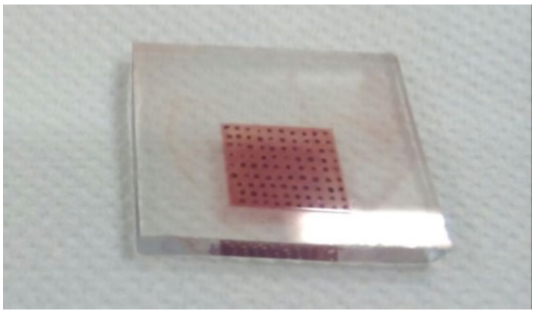

Figure 4.24. SY-S4-P50 photoanode sensitized for 20h with a 0.3 mM alcoholic solution of N719

This value is three times higher than the one of the 1 cm^2 sprayed film alone (3.78 x 10^{-8} mol/cm^2); considering that the total area of the micro-pillars is equal to 8.78 x 10^{-4} cm^2 which is extremely lower than the spray one, these 3D structures show outstanding dye adsorption capability.

The obtained data are an indication about the extremely fine and homogeneously distributed mesoporosity of the micro-pillars obtained by micro-extrusion that greatly enhanced the surface area of the semiconductor structure. To clearly show the influence of the 3D structures on the DSC properties, the next paragraph is devoted to the measurement of the photovoltaic parameters, IPCE curves and also the EIS analysis of both the sprayed films and the complete engineered photoanodes.

4.7 Functional characterizations of the DSC prototypes

In this paragraph the results of the photo-electrochemical characterizations, performed on the cells obtained with just the sprayed layer or with the engineered photoanode, are reported. The J-V curves collected for DSC prototypes just based on sprayed photoanodes (DSC-S) and the ones related to the engineered photoanodes (DSC-P) are reported in Figure 4.25 and Figure 4.26 respectively.

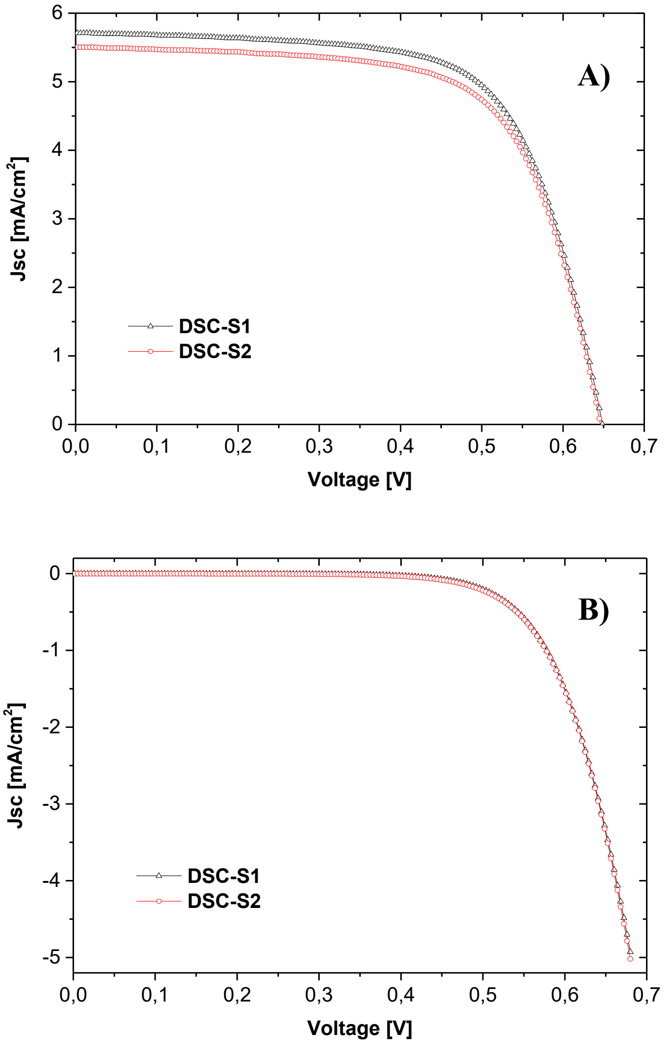

Figure 4.25. J-V curves of DSC-S prototypes based on sprayed semiconductor films A) under 1 sun illumination and B) in dark conditions

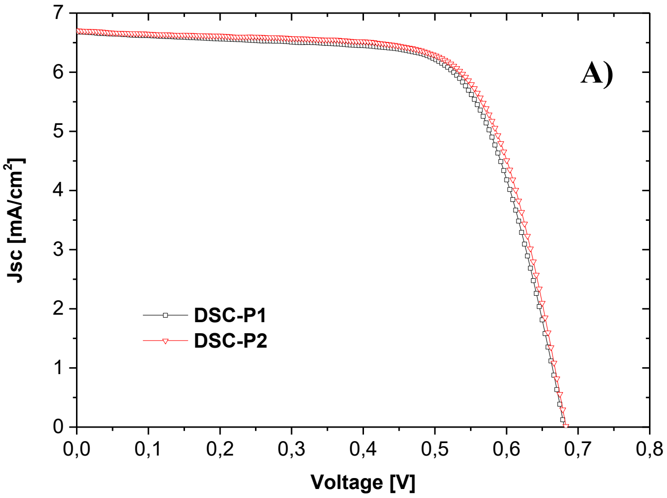

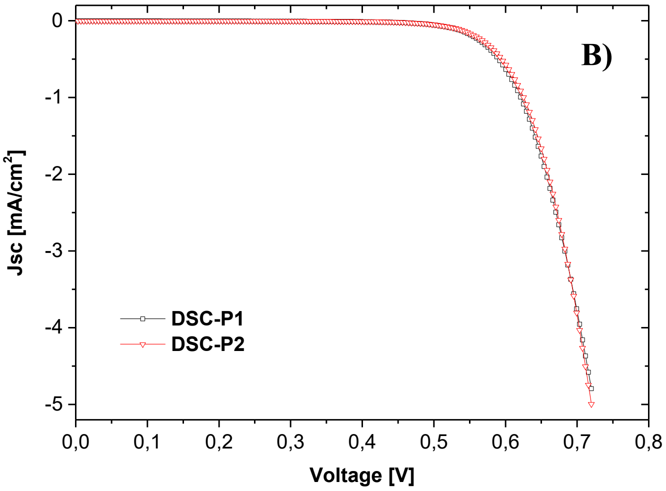

Figure 4.26. J-V curves of DSC-P prototypes based on 3D engineered semiconductor films A) under 1 sun illumination and B) in dark conditions

For each type of DSCs (Figure 4.27) two different prototypes were tested. The curves strongly overlapped clearly indicating accurate depositions of the semiconductor material using both the spray coating technique and the micro-extrusion and an optimized prototypes assembly procedure.

J-V curves are compared and shown in Figure 4.28 while all the resulting devices performance, included the ones coming from traditional scree-printed DSCs (DSC-ScPr series produced and measured for comparison), are collected in Table XV.

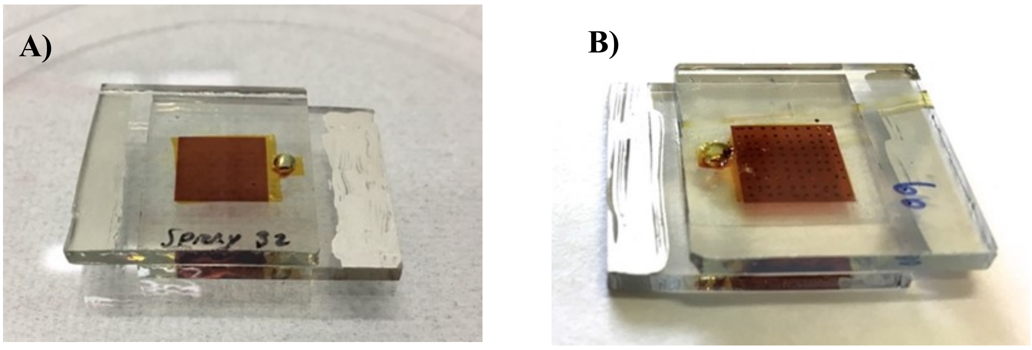

Figure 4.27. DSC prototypes based on (A) sprayed and (B) engineered TiO_2 photoanode

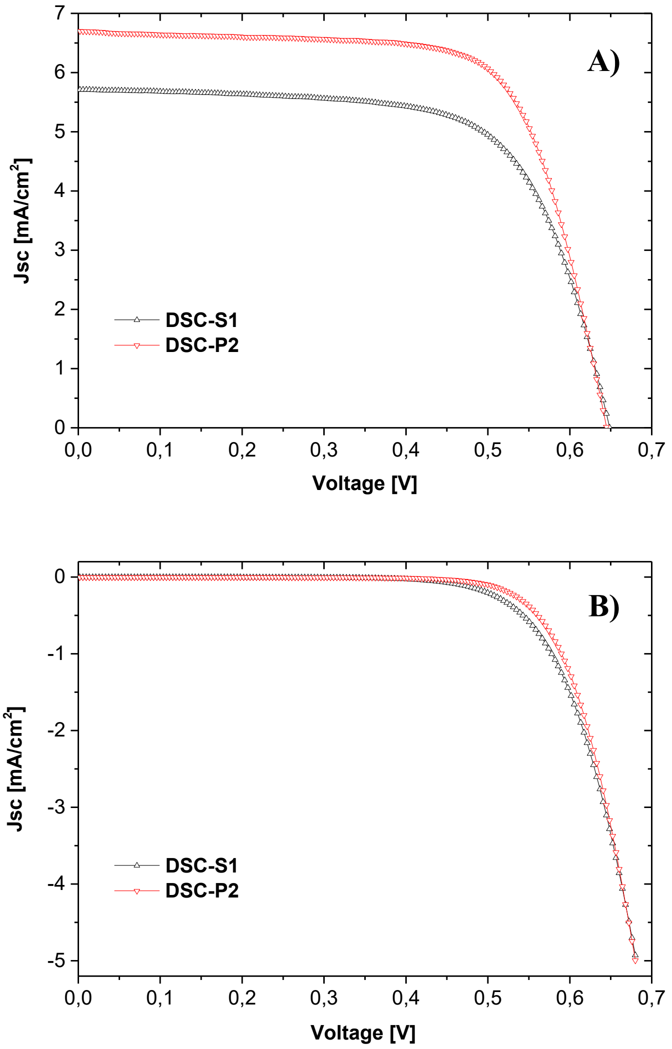

Figure 4.28. J-V curves of DSC-S1 and DSC-P2 A) under 1 sun illumination and B) in dark conditions

Table XV. Performance of the produced DSC prototypes

Prototype	Voc [V]	Jsc [mA/cm^2]	FF [%]	η [%]
DSC-ScPr1	0.655 ± 0.004	4.98 ± 0.02	67 ± 1	2.19 ± 0.03
DSC-ScPr2	0.653 ± 0.003	5.01 ± 0.05	68 ± 1	2.22 ± 0.07
DSC-S1	0.648 ± 0.005	5.72 ± 0.05	67 ± 1	2.47 ± 0.02
DSC-S2	0.646 ± 0.006	5.52 ± 0.07	66 ± 1	2.37 ± 0.05
DSC-P1	0.681 ± 0.004	6.71 ± 0.02	69 ± 1	3.16 ± 0.02
DSC-P2	0.683 ± 0.005	6.75 ± 0.06	70 ± 1	3.22 ± 0.04

All the DSC-S and DSC-P samples present improved performance in respect to the standard screen-printed cells (DSC-ScPr series) with same active area and TiO_2 film thickness. In particular, the Jsc increments (due to higher amount of adsorbed N719 dye) lead to an increase of the final conversion efficiency of about 11% clearly demonstrate that the obtained sprayed films can overcome the screen-printed ones in terms of photovoltaic performance.

The mean efficiency value for the DSC-S devices is around 2.4% while it exceeds 3.0 % for the ones with 3D structures, in accordance with the literature data for similar devices but different semiconductor [23]. The augmented performance are due to a progressive increase in both the current density (Jsc) and open circuit voltage (Voc). The higher photogenerated current is most likely due to the synergy between the high dye adsorption (consequence of the augmented porosity presented by the tridimensional structures) and the scattering effect ascribed to the specific morphology of the pillars. The DSC-P2 efficiency of 3.22 ± 0.04% corresponds to an increase of about the 30% in respect to the DSC-S series. The Voc improvements indicate a lower number of recombination phenomena as confirmed by the respective dark curve that shows a positive shift in the breakdown voltage for the DSC-P2 sample (Figure 4.28 B). In monolithic and mesoporous semiconductor films [20,21], the Voc decreases for film with thickness higher than 10-12 μm due to an increase in the recombination phenomena. In the engineered photoanodes on the other hand, the voltage increases, clear indication of the effectiveness of the micro-pillars to properly drive the electrons towards the DSC anode.

Incident-photon-to-current conversion efficiency (IPCE) is commonly used to express the capability of the cell of converting the absorbed photons into electrons. This parameter is mainly determined by the light absorption efficiency of the dye and the electronic properties of the photoanode, which are strongly affected by its morphology [24]. These measurement for DSC-S1 and DSC-P2 are reported in Figure 4.29.

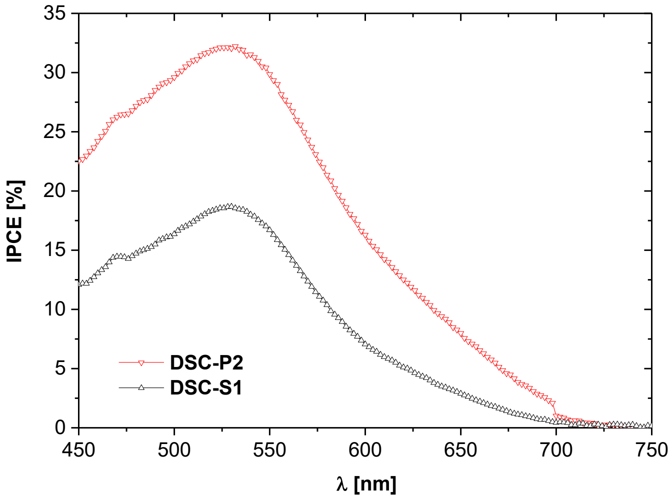

Figure 4.29. IPCE spectra of the best DSC prototypes

The maximum conversion efficiency for the DSC-S1 is close to 20% at a characteristic wavelength of 530 nm, while at the same λ, the prototype with the engineered photoanode shows an increased ability to convert photons into electrons, with an IPCE% value higher than 30%. This improvement is mainly ascribed to the perfected properties of the electrode containing the micro-pillars and, secondly, to the higher dye loading.

Electrochemical impedance spectroscopy (EIS) was then used to investigate the interfacial charge transfer processes of the devices, in particular at the N719 coated TiO_2 photoanode/electrolyte interface. EIS spectra were registered in the frequency range from 0.05 to 10^5 Hz, with an amplitude of 10 mV, under illumination (1000 W/m^2) and open circuit conditions. Figure 4.30 reports the Nyquist plots of the high-performing devices; the data fitting was performed using the equivalent circuit in the inset and the derived parameters are listed in Table XVI.

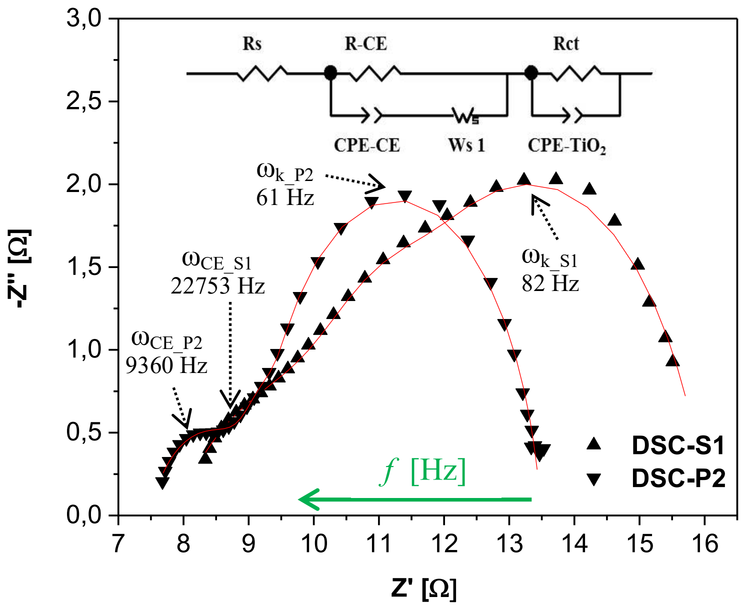

Figure 4.30. Nyquist plots of the best DSC prototypes, the equivalent circuit used for the fitting is reported in the inset. Symbols: experimental data. Continuous lines: curves fitting.

Table XVI. EIS parameters derived from the fitting of the experimental data.

Circuit element	DSC-S1	DSC-P2
R_S [Ω]	7.865 ± 0.052	7.467 ± 0.027
R-CE [Ω]	2.895 ± 0.200	1.577 ± 0.047
CPE-CE (Q)	$3.7722\text{x}10^{-7} \pm 2.8192\text{x}10^{-7}$	$1.5742\text{x}10^{-8} \pm 1.1044\text{x}10^{-8}$
CPE-CE (n)	1.584 ± 0.083	1.931 ± 0.078
Rct [Ω]	5.282 ± 0.199	4.445 ± 0.040
CPE-TiO_2 (Q)	$129.96\text{x}10^{-5} \pm 7.47\text{x}10^{-5}$	$98.141\text{x}10^{-5} \pm 3.337\text{x}10^{-5}$
CPE-TiO_2 (n)	0.81155 ± 0.01899	0.90147 ± 0.00750

All the experimental data were interpolated using the equivalent circuit reported above; it was able to fit all the spectra giving χ^2 values of the order of 10^{-4} therefore a good fitting parameter. In order of decreasing *f*, the characteristic frequencies ω_{CE} and ω_k correspond to the charge transfer processes at the Pt/electrolyte interface (counter electrode) and the electron transfer and recombination at the TiO_2/dye/electrolyte interface (photoanode), respectively [25].

Focusing on the latter, it is possible to observe that the amplitude of the semicircle is significantly reduced for DSC-P2. This means a reduced charge transfer resistance, induced by the peculiar morphology and the higher dye loading. This observation is confirmed by the parameters reported in Table XVI. Rct, which indicates the charge transfer resistance at the TiO_2/dye/electrolyte interface, is in fact equal to 5.282 Ω for DSC-S1 while it decreases down to 4.445 Ω for DSC-P2. Although being beneficial for the charge transport and then for the generated photocurrent, a reduction of the charge transfer resistance may enhance the recombination dynamics. It was in fact demonstrated that an increase in the charge transfer resistance at the TiO_2/dye/electrolyte interface could suppress charge recombination [26]. In order to have a deeper insight on this aspect, the electron lifetime in the different photoanodes was quantified using the equation $\tau_n = [Rct*CPE\text{-}TiO_2(Q)]^{1/CPE\text{-}TiO2(n)}$. The resulting electron lifetime for DSC-S1 is 21.60 ms while the value for DSC-P2 is 24.08 ms. These data are comparable with the ones of similar system sensitized with N719 dye [27,28] and give the final confirmation that the recombination processes are reduced by the presence of 3D microstructures, thus increasing both the Voc and Jsc. Finally, to complete the functional characterizations, the photoanodes capacitances were calculated using the equation $C\mu = \tau_n / Rct$. The resulting electric capacitances for the prototypes are 4.895×10^{-4} and 6.587×10^{-4} F for DSC-S1 and DSC-P2 respectively. The performance improvements, recorded for the DSC containing micro-pillars are even more confirmed by these capacitance values that indicate a beneficial effect in terms of photoanode capability to host an higher amount of electrons.

4.8 Introduction to inkjet printing of micro-pillars

While the work on micro-extrusion described previously prove the beneficial effect of pillars on the photovoltaic performances of a DSC cell, it is obvious that this technique allows to build structures of dimension in the order of tens of micron. For the sake of pushing the performance is therefore important consider other possible ceramic techniques able to give structures of smaller dimensions. In this context, an alternative deposition method is the material jetting technique (based on the inkjet printing technology), one of the most exploited technique in the field of flexible electronics field to produce 3D ordered patterns. As already describe in Chapter 2 (section 2.4.7), this technique can be considered as an additive manufacturing method for the fabrication of 3D features by repeated printing of particulate suspensions. It is an extremely accurate deposition technique that allows to carefully design both the location of each ink droplets and their volumes/dimensions, assuring the production of extremely fine features. All these characteristics perfectly match the requirements of the PhD thesis. For this reasons, part of the thesis work was dedicated to explore the possibility to use this technique to enhance the TiO_2 micro-pillars aspect ratio on the optimized sprayed films.

Inkjet printing is a very powerful deposition technique but it requires a high level of control as it is based on several number of variable that have to be mastered especially for the production of 3D high aspect ratio structures of functional materials (as in this case with TiO_2). One of the most important role is played by the ink. The ink should meet requirements mainly related to jetting performance, wetting and adhesion on substrate. Due to these very challenging requisites, the production of such inks is often demanding. For example, each print head has a specific window of surface tension and viscosity range which enables proper jetting. Piezoelectric print heads for e.g. (like the one used in this work) usually function within a viscosity range of 8 – 15 cP. The use of specific printing system therefore, dictates the physicochemical properties of the inks like the selection of the components of the formulation, etc. Thus, while formulating new inkjet inks, the effect of each component on the overall ink performance, from its storage, through jetting, to its behavior on the substrate and its effect on health and the environment must be taken into account. Such considerations are valid for all types of inkjet inks (solvent and water-based, etc.) becoming even more important for functional inks based on ceramic materials, which should meet the usual inkjet ink requirements but, as in this specific case, in addition should provide good electrical conductivity. Several difficulties are connected with the composition and application of ceramic inks. The first is the rheology of ceramic suspensions. The viscosity of these suspensions in general shows a shear dependency on the volume fraction of solids, the interparticles forces, the particles size and shape. During the printing process high shear rates are exerted on the ink, so the shear dependent viscosity of it may strongly influence the inkjet pumping mechanism. Secondly, due to the high density of ceramics, the chemical stability of the ink is a critical issue. The sedimentation of solids within the print head in fact, can lead to easy clogging of the nozzles.

This chapter starts by describing the development of a ceramic aqueous ink, which is composed by TiO_2 powder, water (with the control of the pH), dispersant and surfactant. pH and dispersant were used to stabilized of the suspension while the surfactant was used to tune the ink surface tension. The use of a binder is finally considered to promote the retention of the shape of the single droplet during the building of the micro-pillars.

4.9 Inkjet ink formulation

In this paragraph, the work done to formulate a suspension suitable for the deposition process is reported. The aim was to formulate an aqueous ink with TiO_2 content at least equal to 2 vol.% (considered quite high for the inkjet process) suitable for the formation of micro-pillars. The stability of the suspension in term of pH and dispersant amount was investigated. Attention was then paid on the milling treatment and on the use of other additives such as surfactants and binders needed to retain the 3D structure.

4.9.1 Characterization of the starting powder

The formulation of an ink for the inkjet process starts from the choice of the proper raw material that must have dimensions compatible with the nozzle dimension (50 μm) to avoid clogging. For this reason the TiO_2 powder chosen was thoroughly analyzed. The starting material chosen was a pure anatase TiO_2 powder (99.8% trace metal basis) purchased by Sigma-Aldrich with density equal to 3.90 g/cm^3 and specific surface area, (measured by BET analysis) of 10.91 m^2/g. From the latter, assuming spherical and homogeneous primary particles [29] and using the equation:

$$D = \frac{6}{(SA * \rho)} . 1000$$

where D is the mean particle size (nm), SA is the surface area from BET data (m^2/g) and ρ is density (g/cm^3) is possible to derive the mean particle size. For the abovementioned system the calculated mean particle size was found to be equal to 140 nm.

DLS analyses were carried out to experimentally verify this value. To obtain reliable results from this technique, is however necessary to derive the suitable particle concentration to be used for the measure. For doing so, samples with concentrations equal to 10, 1, 0.1 and 0.01 wt.% of TiO_2 in water were considered. The DLS measurements, in terms of particles dimensions, stability and polydispersion, indicated the latest as the most suitable concentration. Thus, the subsequent studies were performed on 0.01 wt.% TiO_2 suspension (called St_TiO_2). The intensity vs particle size graph is shown in Figure 4.31 while Table XVII collects St_TiO_2 size and ζ-potential values.

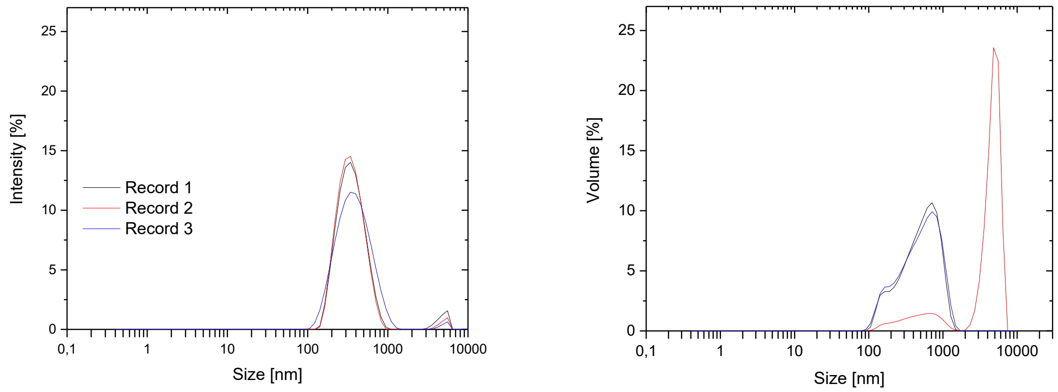

Figure 4.31. St_TiO_2 sample size distribution by intensity and volume (3 records were performed for a sake of accuracy)

Table XVII. DLS data of the St_TiO_2 sample

Z-average [nm]	PDI	ζ-potential [mV]
343.0 ± 9.2	0.205 ± 0.015	-32.1 ± 0.4

The DLS intensity graph (Figure 4.31) shows two distinct peaks: the highest at around 330 nm with a maximum intensity value of 12-14 % and the second one at 4.5 μm with an intensity of 1-2 %. The suspension polydispersion is highlighted by the PdI value which is equal to 0.205. Considering that the intensity is not proportional to the diameter of the particles but to 10^6 diameter, even if the big agglomerates are very few in number they have a significant contribution in term of intensity. Moreover, talking about their volume percent (Figure 4.31), the big agglomerates influence is even more important since they represent more than half of the volume of the suspended particles. The suspension ζ-potential is negative and equal to -32.1 ± 0.4 mV typical of a suspension with a sufficient stability [30].

The SEM images confirm the presence of some micronic aggregates formed by primary particles of about 140 nm (Figure 4.32). The dimensions shown in the micrographs are in full accordance with either the BET and the DLS analyses.

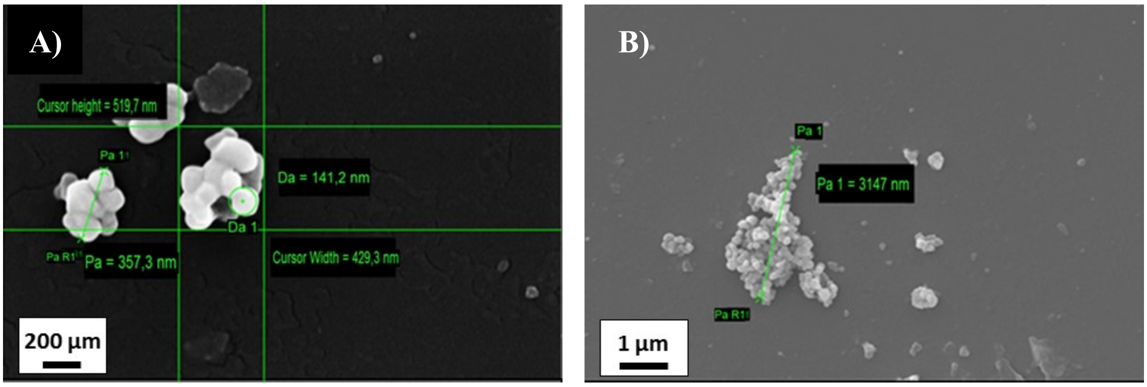

Figure 4.32. SEM images of the Aldrich powder at different magnification

To conclude, even if the ζ-potential value is typical of suspension with a good degree of stability, DLS analysis shows a polydispersed powder containing micrometer agglomerates (of about 3 µm) unsuitable for the inkjet nozzle (empirical rules report that the particle dimension should be 50-100 times lower than the nozzle diameter to avoid the nozzle clogging). These micrometer aggregates are attributed to an agglomeration tendency of the primary particles with time. For these reasons, the activities were focused on increase the stability of the suspension modifying the pH, the dispersant amount and finally, the TiO_2 suspension ionic strength.

4.9.2 Stability investigations in terms of pH, dispersant and ionic strength

Influence of the pH

The influence of the pH on the St_TiO$_2$ ζ-potential is reported in Figure 4.33. The pH was tuned adding aqueous solutions of HCl 0.1 M and KOH 0.1 M respectively.

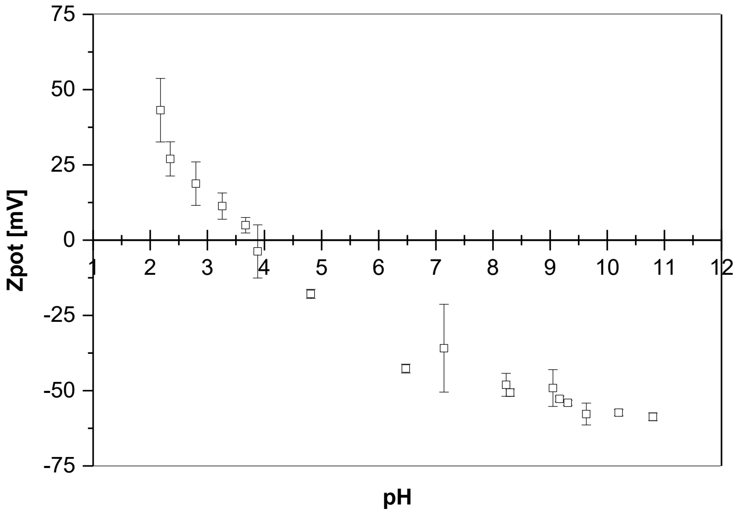

Figure 4.33. ζ-potential distribution of the TiO$_2$ suspension as a function of pH

The ζ-potential pass from positive (43 mV) to negative values for an increase of pH reaching a plateau around -55 mV above pH 8. An important parameter to be considered in this kind of analysis is the position of the isoelectric point (IEP). The isoelectric point is the pH value at which the ζ-potential is zero [31] therefore it represents the maximum instability of the suspension. The change of the ζ-potential sign is due to the mechanism of protonation/deprotonation on the particles surface. In an acidic environment, the reaction between the metal oxide surface and the proton ($M\text{-}OH + H^+ = M\text{-}OH^{2+}$) leads to a positive value of ζ-potential. In basic media on the other hand, the negative ζ-potential value is due to the different interaction with the surface through the reaction $M\text{-}OH = H^+ + M\text{-}O^-$. Several authors report for an aqueous-based TiO$_2$ suspension, a IEP in the range of pH 5-7 [32], whereas in this experiment is equal to 3.8. This phenomenon could be linked to the size of the TiO$_2$ primary particles; Suttiponparnit et al. [33] found in fact a clear dependence of the IEP of anatase TiO$_2$ from its particle size. In their work, they report that when primary particle size increases from 6 to 104 nm, the IEP decreased from pH 6.0 to 3.8, the same value observed in the present work. As the absolute value of ζ-potential has to be the highest to assure an high suspension stability, the previous analysis suggested the need to operate at pH higher than 8.

The value of zeta potential can be strongly correlated to the particles size in suspension.

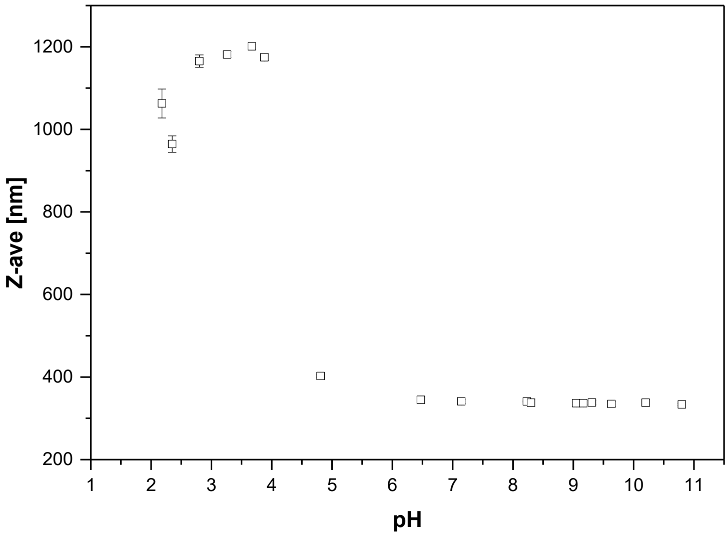

Figure 4.34. Size distribution of the TiO_2 suspension as a function of pH

Figure 4.34 shows that for pH up to 4 (i.e. near the isoelectric point), the agglomerates have a micrometer size as a consequence of the particles agglomeration in the very unstable suspension. When the pH is increased however, the size decreases significantly reaching a plateau around 340 nm at pH around 7. Matching the results from the zeta potential and the dimension in suspension, is obvious that the system should be kept at pH in the range between 7 and 11 to assure the highest stability and the lowest particle dimensions.

At this point is important to remember that the zeta potential analyses are done in very diluted suspensions that help in investigating the systems but that do not represent the system in real conditions. Therefore in order to assure a reduction of the presence of aggregates in the suspension and therefore prevent clogging of the nozzle, the system usually undergoes a milling treatment. Kuscer et al. [18] however, noticed that the pH of a TiO_2 suspension decreases when the powder is milled. This phenomenon is due to an increase of the surface area during the treatment: higher the surface area more hydroxyl group are exposed (Ti + H_2O -> Ti-OH + H^+) and able to free H^+ in solution. This effect leads to a substantial decrease in the pH value [34]. To balance between this phenomenon and the fact that the pH should not be too high to avoid any damage of the inkjet head, the pH was set at 9 stabilizing it with a buffer solution of ammonium hydroxide as already mentioned for a wide range of other applications [29]. As already mentioned finally, DLS measurements are commonly performed on diluted systems so the relative results could be hardly transferable to higher concentrated samples. This issue was studied by Wang et al. [34]. The ζ-potential can be affected at low concentration because of the non-negligible effect of the dissolve CO_2; this concentration dependence is however strong between pH 3 and 8 but does not affect the ζ-potential in an important way for higher pH. In this sense, the results here reported at high pH can be considered valid also for high solid loaded systems.

Influence of the dispersant amount

A ceramic suspension, it is not normally stabilized just tuning the pH but also with the addition of a specific dispersant that help in improving the stability of the high density ceramic particles in suspension. A pH 9 buffered TiO_2 suspension was prepared through a 3 hours ball milling treatment applied to avoid big aggregates; the dispersant added to the as-prepared suspension was Duramax D-3005. The latter is an ammonium salt of poly(acrylic acid) that combines the electrostatic action with the steric one. Its amount was varied from 0 to 2 wt.% (in respect to the TiO_2 mass).

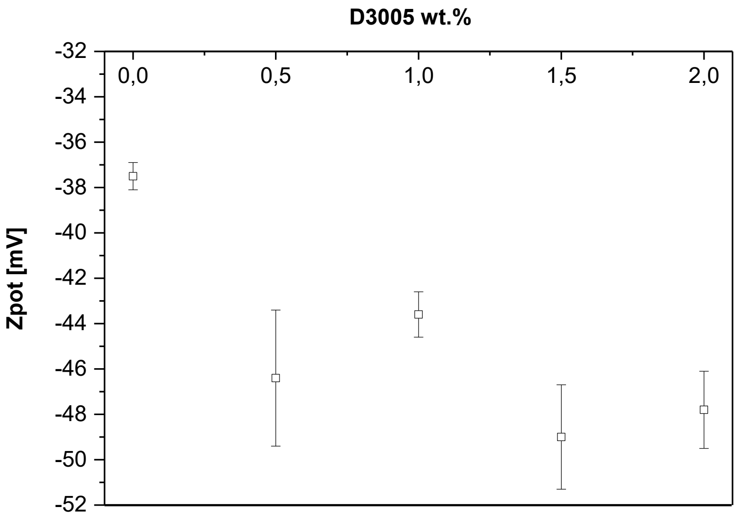

Figure 4.35. ζ-potential trend of the TiO_2 suspension as a function of dispersant amount

The ζ-potential of the starting ball-milled suspension starts from -37 mV as consequence of the milling treatment but then decreases more than 10 mV when the D-3005 was added (Figure 4.35) with final values between -45 and -50 mV. The optimal dispersant amount was chosen considering the correspondent particle size (Figure 4.36 and Table XVIII).

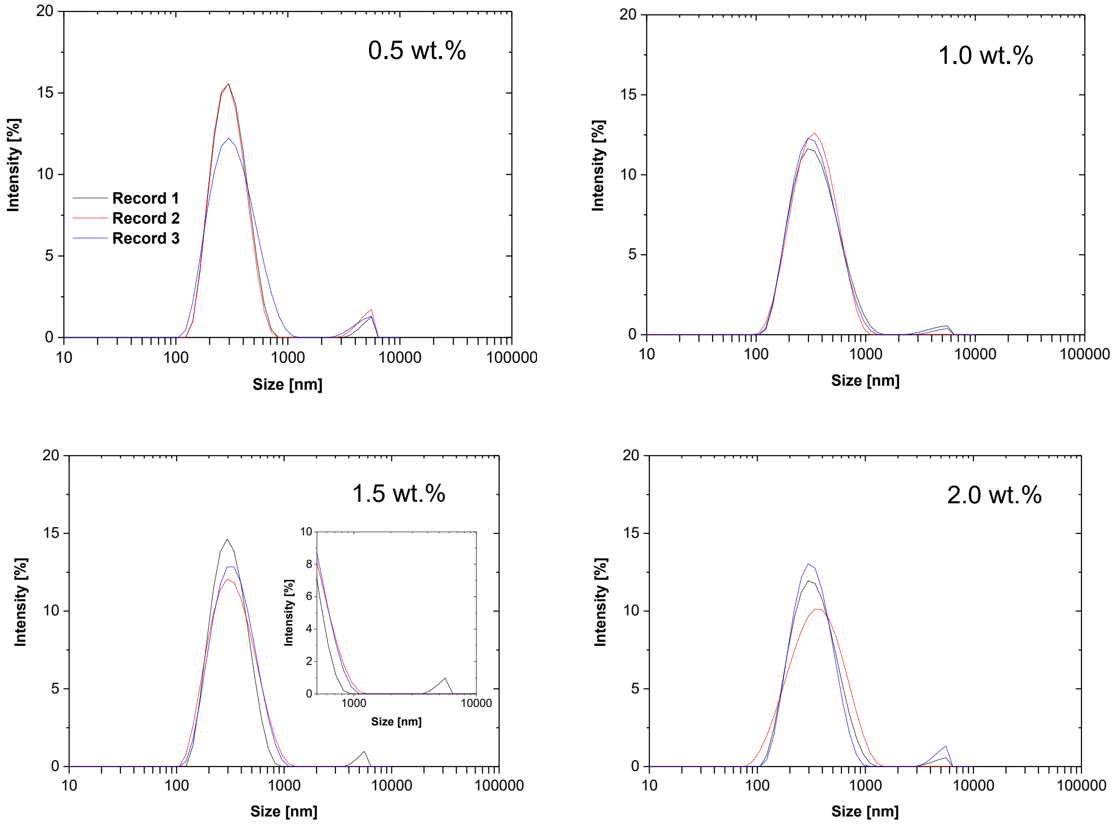

Figure 4.36. Size distribution of the TiO_2 suspension as a function of dispersant amount

Table XVIII. Size and PDI distribution of the TiO_2 suspension as a function of dispersant amount

	0.5 wt.%	**1.0 wt.%**	**1.5 wt.%**	**2.0 wt.%**
Z-Average [nm]	307.3 ± 7.2	316.1 ± 3.3	307.2 ± 4.3	310.1 ± 3.7
PDI	0.213 ± 0.017	0.183 ± 0.011	0.177 ± 0.006	0.205 ± 0.015

The Z-Average values are comparable for each concentration and the intensity graphs show that some micrometric agglomerates remain in the suspension for all the tested dispersant concentrations. However, the sample containing 1.5 wt.% of D-3005 exhibits big agglomerates just for one of the three recorded curves as shown in the inset graph and moreover, it shows the lowest PDI value indicating a monodisperse suspension.

Taking into consideration all these different results, 1.5 wt.% concentration was considered as the optimal dispersant amount. However previous analyses have shown that as results of the milling process needed to reduce the bigger aggregates, the overall powder surface area was increased of about 10%. Considering that the dispersant acts on the particles surfaces, this effect was taken in account increasing the D-3005 amount up to 1.65 wt.%, in respect of the TiO_2 mass.

Ionic strength calculation

The ionic strength of the suspension is strictly related to its stability. If it is too high, the double layer thickness around the particle is reduced and the electrostatic repulsions are lowered. Energetically, the barrier to be overcome to form agglomerates is lower thus the agglomerates formation is easier and the system is destabilized. According to [33], an ionic strength of 0.001 mol/L is the maximum value acceptable for a stable TiO_2 dispersion.

The ionic strength is dependent from the buffer ammonium solution and the ions coming from the dispersant. The ammonium concentration in the buffer solution is 8 x 10^{-4} mol/L while the concentration of dispersant is 1.8 x 10^{-4} mol/L (see calculation in Appendix 3). The ionic strength is calculated following the formula: $I = \frac{1}{2}\sum C(i)z(i)^2$ where C(i) is the molar concentration and z(i) is the charge of the ion. The result of the calculation is I = 9.8 x 10^{-4} mol/L, which almost exactly corresponds to the maximum value previously reported. In the chosen conditions, therefore, the TiO_2 suspension stability is not affected by the ionic strength.

4.9.3 Study of the milling methods

As already anticipated, in order to avoid micrometric aggregates a strong mechanical disaggregation treatment of the TiO_2 suspension was considered necessary. Three different milling methods were compared: ball milling, planetary milling and ultrasonication. Batches of the starting suspension composed by 0.01 wt.% of TiO_2, 1.65 wt.% of Duramax D-3005 and the buffer solution with a pH of 9.5 underwent the different milling treatments and the results obtained are reported, in Table XIX. The conditions applied for each treatment were:

Ball milling (BM) [35]: the suspension and the milling media were placed in a cylindrical flask rotating along its long axis. The particle size reduction is due to the impacts between the media and the particle of the powder. The treatment lasted three hours with ZrO_2 milling media of 300 µm and 3 mm.

Planetary ball milling (PBM): the suspension and the milling media were put into a grinding jar. The jar moves at the same time along its own axis and on a circular orbit. The movement of the media and the frictional forces due to the movement of the jar contribute to the particle size reduction. The suspension was milled for 3 hours using cycles composed of 20 minutes of milling and 10 minutes of pause.

Ultrasonication (US): it consists in applying sound energy to break the agglomerates. The milling was done using a wave of 20 kHz, with an amplitude of 40% in cycles of 10 seconds pulse followed by 10 seconds pause [13] for a total treatment of 90 minutes.

Table XIX. Influence of milling treatments on the pH, Z-average and PDI of the TiO_2 suspension

Sample	pH	Z-Ave [nm]	PDI
Starting suspension	9.60	307.2 ± 3.3	0.177 ± 0.006
BM	9.35	322.7 ± 3.1	0.166 ± 0.016
PBM	9.20	347.3 ± 2.6	0.193 ± 0.021
US	8.36	294.5 ± 5.2	0.236 ± 0.006

Each milling method induces a pH decrease, clear sign of powder de-agglomeration and consequent increase of specific surface area. The most pronounced decrease is obtained applying the US treatment to which correspond the highest particles dimension decrease. In this case however the US sample presents an higher PDI value and moreover, it shows the presence of a black sediments at the bottom of the beaker, already reported in other papers and ascribed to the erosion of the ultrasonic horn [36]. On the other hand, the other two processes showed Z-Average values higher than the respective value before the treatment. Thus, the milling processes initially break the agglomerates but afterwards due to the impact with the milling beads, induce particles re-agglomeration. The US treatment is therefore the best to reduce the aggregates dimension in suspension as shown by the higher decrease of pH and Z-Average and it is also the less time consuming method. As consequence, this process was chosen for the subsequent work even if none of the abovementioned process was able to completely eliminate some micrometer agglomerates, impeding the actual use in the ink jet process (see DLS graphs in Appendix 4). The results reported up to now showed that the Aldrich powder is not suitable for the DoD process, for this reason it was substituted with another TiO_2 powder possessing higher surface area (P25 Aeroxide).

4.9.4 Study of the P25 Aeroxide

The P25 Aeroxide powder (Evonik) is a mix of anatase and rutile phases in ratio 80/20 wt.%. The primary particle size is of 25 nm, with specific surface area of 57.4 m^2/g. Although this powder is not formed by purely anatase and therefore could exhibit a slightly lower photovoltaic performances, its primary particle is more compatible with the deposition process enhancing the suspension stability [37].

This powder is well known in literature; according to Brayner et al. [38], the IEP of P25 is 6.25 while Leroy et al. [39] reports that the ζ-potential is close to its highest absolute value above pH 8 (Figure 4.37).

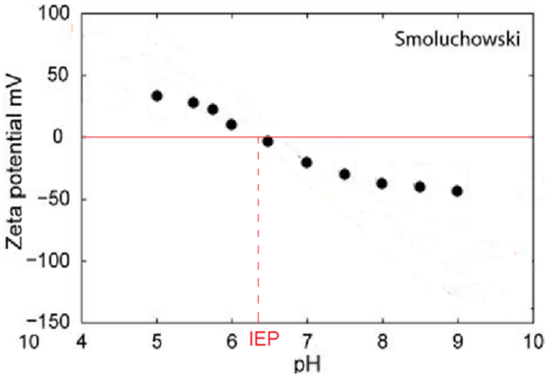

Figure 4.37. P25 Zeta potential evolution as a function of the pH [36]

The amount of dispersant was preliminarily kept at the same value that (1.65 wt.%) found previously. A 0.01 wt.% P25 suspension containing 1.65 wt.% of D-3005 (in respect of TiO_2 mass) with a pH value of 9.5 was ultrasonically treated using the same conditions described in the previous paragraph. As the ultrasonication causes black sediments at the bottom of the beaker, the sample was filtered two times, using a 5 µm filter. To evaluate the stability of the TiO_2 suspension, two consecutive DLS analyses were carried out, one just after filtration (Figure 4.38) and the other one after 3 hours (Figure 4.39).

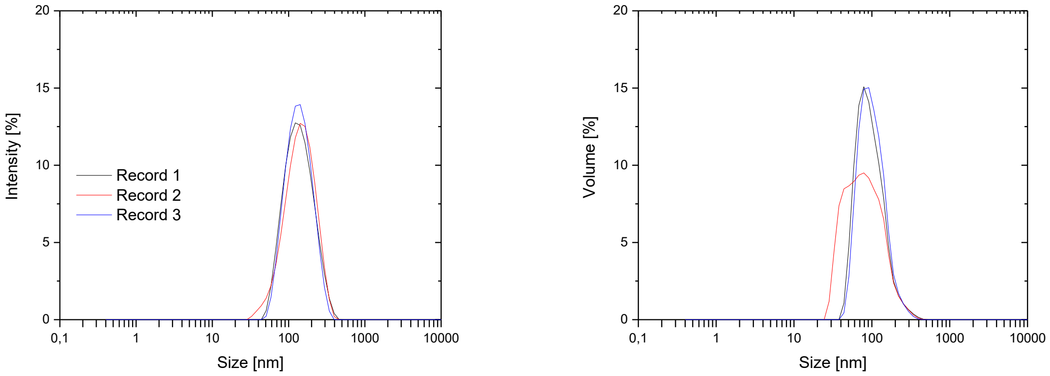

pH = 7.93 Z-Pot. = -42.4± 0.9 mV Z-Ave = 125.1 ± 0.8 nm PDI = 0.149 ± 0.021

Figure 4.38. P25 suspension (0.01 wt.%) size distribution by intensity and volume just after filtration

Figure 4.38 shows only one peak for both the graphs. The particles size is in the range of 40-150 nm with a Z-Average around 130 nm, half of the value obtained with the Aldrich powder.

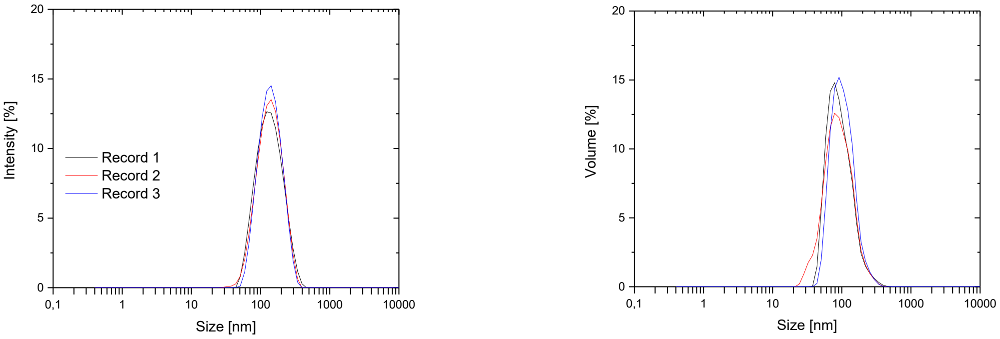

pH = 7.80 Z-Pot. = -41.6 ± 0.7 mV Z-Ave = 131.2 ± 1.0 nm PDI = 0.140 ± 0.017

Figure 4.39. P25 suspension (0.01 wt.%) size distribution by intensity and volume 3 h after filtration

The ζ-potential values indicate a good stability of the suspension which, in fact, does not present big agglomerates even after 3 hours of aging (Figure 4.39). The time-depending pH decrease is ascribed to the atmospheric CO_2 dissolution in the suspension. This decrease might be also the cause of the slight ζ-potential decrease. The P25 powder ultrasonically treated, appears as a suitable starting point to formulate the desired inkjet ink.

4.9.5 P25 TiO_2 powder content increase and influence of the milling time

To check the behavior of a suspension suitable for the ink jet process, a 2 vol.% suspension containing 1.65 wt.% of D-3005 at pH 9.6 was ultrasonically mixed for different times. The DLS analyses were performed just after the treatment, after 3 h and one day of aging; a filtration step was introduced before each analysis. The results are summarized in Table XX (DLS graphs are presented in Appendix 5). To perform reliable DLS analysis, the suspensions were diluted 1:500.

Table XX. DLS results of a P25 TiO_2 suspension (2 vol.%) at different time of ultrasonication

Time	pH	Z-Ave [nm]		PDI		ζ-potential [mV]	
		No aging	aged	No aging	aged	No aging	aged
10’	9.35	137.9 ± 1.2	133 ± 1.0	0.147 ± 0.002	0.132 ± 0.019	-49.1 ± 0.5	-49.8 ± 0.4
30’	9.20	128.8 ± 0.4	126 ± 0.4	0.151± 0.013	0.148 ± 0.014	-49.7 ± 1.2	-48.0 ± 1.0
50’	8.36	121.0 ± 0.9	118 ± 0.4	0.147± 0.006	0.141 ± 0.016	-52.5 ± 3.4	-50.1 ± 0.5

As expected the pH and the Z-Ave values decrease when the treatment is applied for a longer time, the more the treatment lasts, the more the ζ-potential slightly increases (in absolute value). After the aging, the results are almost identical; small Z-Average reductions might be due just to the filtration step. Unfortunately, as direct consequence of more intense ultrasonic treatments, the quantity of black sediment was increased (Figure 4.40).

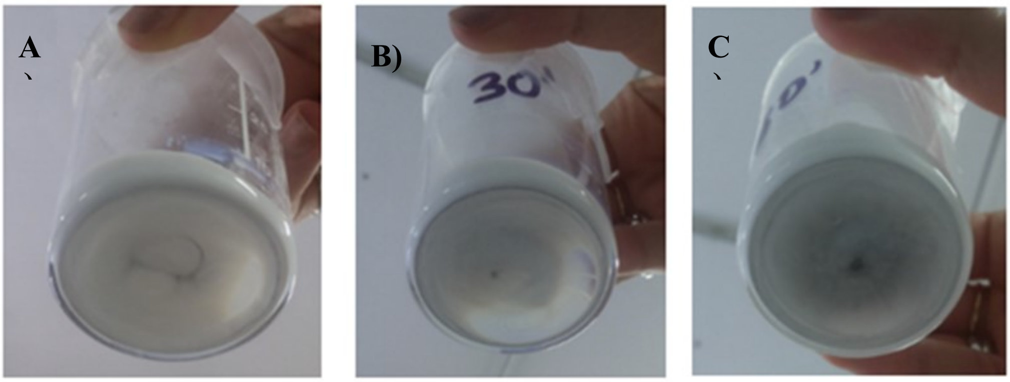

Figure 4.40. Proportional black sediment increase after (A) 10, (B) 30 and (C) 50 minutes of ultrasonication

No significant differences raise from different milling times therefore, to minimize the black sediment phenomenon and concurrently perform a suitable disaggregation treatment, 15 minutes was selected as proper milling time. The suspension viscosity (Figure 4.41) and surface tension for this sample were 6.5 ± 0.2 mPas and 48.77 ± 0.34 mN/m respectively.

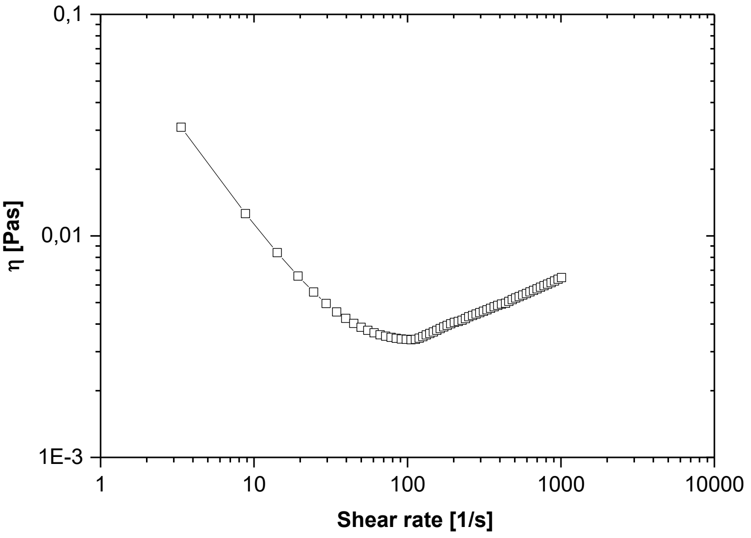

Figure 4.41. Viscosity of the P25 TiO_2 suspension (2 vol.%) ultrasonically treated for 15 minutes

As already discussed in Chapter 2 (section 2.5) during the fire pulses, high shear rates (about $\gamma = 10^4 - 10^6$ 1/s) are exerted on the ink. It is difficult to conduct representative viscosity experiments at such high values, so the studies on the suspension viscosities have been commonly obtained at lower shear rates using traditional rheometers. In this case in fact, the viscosity was evaluated at the highest shear rate value equal to 10^3 1/s and the obtained result lays in the optimal range for the printing head. Unfortunately, the value of surface tension is not inside the optimal range for the process (20-45 mN/m) [40]: to tune the latter, the formulation was modified adding a binder and a surfactant.

4.9.6 Addition of binder and surfactant

The binder selection was mainly oriented by its solubility in aqueous environments. Two different binders were then identified and tested: polyvinyl alcohol (PVA) and a commercial polymer emulsion (Duramax B-1000). The surfactant chosen was Triton X-100, a non-ionic surfactant that is able to lower the surface tension of the suspension

[41]. Its content was fixed at 1 wt.% of the total suspension mass (0.93 vol.%) as indicated in literature [42].

Polyvinyl alcohol (PVA)

PVA is a well-known synthetic polymer, it is non-toxic and fully biodegradable. An high molecular weight (85000-124000) polyvinyl alcohol was used.

The reagent was slowly dissolved in the buffer solution in order to produce a suspension 12.4 vol.%. The content of PVA in the initial formulation was fixed at 3 vol.%, concentration usually considered for printing three-dimensional structures [43,44]. The PVA-based ink composition is reported in Table XXI.

Table XXI. PVA-based ink formulation

Material	Function	Vol.%
TiO_2 (P25, Degussa)	Active phase (solid fraction)	2.00
Buffer solution	Solvent	88.72
Duramax D3005	Dispersant	5.40
PVA	Binder	2.95
Triton X-100	Surfactant	0.93

Rheological analyses were done on the ink to assess its suitability for the deposition process (Figure 4.42).

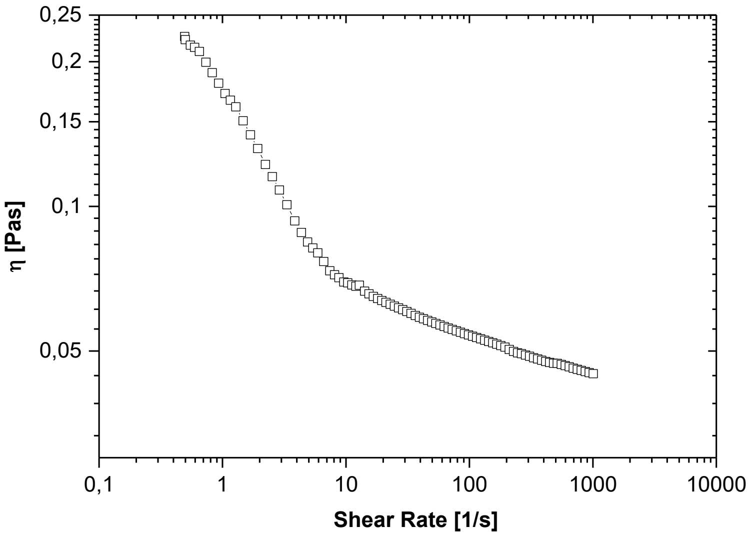

Figure 4.42. Flow curve of the PVA-based ink determined with C25

Figure 4.42 reports the flow curve obtained with the coaxial cylinders (C25) geometry. The fluid exhibits a shear-thinning behavior with a viscosity value much higher than the one recommended for the inkjet device (0.4 – 20 mPas). At 1000 s^{-1}, in fact, it is equal to 44.8 ± 2.2 mPas that is clearly incompatible with the printhead requirements. Moreover, during the raw materials mixing step, a pronounced foaming phenomenon was observed even with lower PVA concentrations (1 – 2 vol.%).

Concluding this polymer was not selected as suitable binder; the 3 vol.% PVA-based ink demonstrated too high viscosity and in addition, the binder triggered foaming phenomena (also at lower concentrations) that can be detrimental for the correct printhead functioning.

Duramax B-1000

This binder is an acrylic latex emulsion [44], i.e. a stable colloidal dispersion of an ammonium salt of acrylic homopolymer in an aqueous medium [45]. Latexes binders are often used in aqueous suspension for their high drying rate and their high polymer content at low viscosity [46] that enable high binder loading while keeping low the viscosity of the suspension. A first binder concentration value was derived from the previous work of Lejeune et al. [47], that used binders to build 3D structures for piezoelectric and photocatalytic applications. In their paper a binder content between 25 and 40 vol.% was used for a corresponding powder loading of 10 vol.%. Assuming a linear relation between the powder content and binder concentration (as indicated in the article) the B-1000 amount for the suspension used in this work (2 vol.% powder loading) was fixed at 9.4 vol.%. Taking into consideration that the Duramax B-1000 presents a polymer solid percentage of 55 % and that the information available do not specify if the suitable concentration for the process is of active molecules or microemulsion, two different quantities were investigated for the production of the inks: 9.4 and 18 vol.% (Table XXII).

Table XXII. B1000-based ink formulations

Material	Function	Vol.%	Vol.%
TiO_2 (P25, Degussa)	Active phase (solid fraction)	2.00	2.00
Buffer solution	Solvent	82.17	73.57
Duramax D3005	Dispersant	5.50	5.50
Duramax B-1000	Binder	9.40	18.00
Triton X-100	Surfactant	0.93	0.93

The viscosity tests performed using the C25 geometry are reported in Figure 4.43.

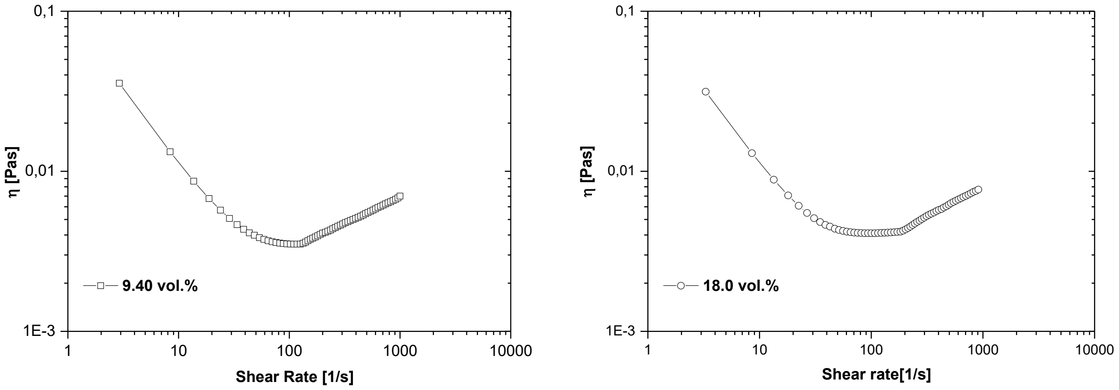

Figure 4.43. Flow curves of the B1000-based inks (9.40 and 18.00 vol.%) determined with C25 geometry

The viscosity comparison shows that doubling the content of B-1000 does not strongly influence the ink viscosity as expected by the properties just mentioned above. As it is important to reduce as much as possible the amount of binder to reduce the shrinkage of the pillars after firing, the suspension containing the 9.4 vol.% of binder (called P25_B1000 sample) was considered for the further studies. Surface tension measurements were carried out and the relative results are reported in Table XXIII; the obtained value is in the theoretical best range for the inkjet printing technique (30-33 mN/m) [48].

Table XXIII. P25_B1000 surface tension; (*without binder and surfactant)

Sample	Surface Tension [mN/m]
Base suspension*	48.77 ± 0.34
P25_B1000	30.91 ± 0.23

The suspension was then filtered through a 5 µm filter and aged for 3 hours to mimic the process set before printing. After that, DLS analysis were performed diluting the ink 500 times (Figure 4.44) to assess their stability.

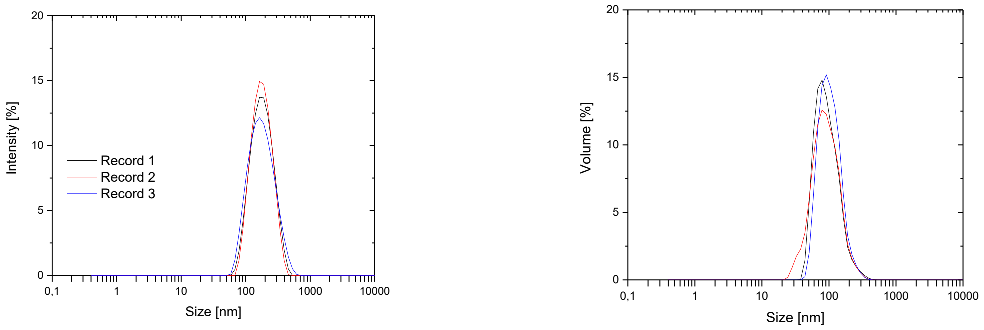

Z-Pot. = -51.1 ± 0.6 mV   Z-Ave = 160.9 ± 1.4 nm   PDI = 0.145 ± 0.017

Figure 4.44. P25_B1000 suspension size distribution by intensity and volume after 3 h of aging

The analysis showed a good stability of the ink with no micrometer agglomerates; the Z-Ave was found to be in the range 50 - 600 nm fully compatible with the instrument nozzle. Also the ζ-potential value confirms the stability of the system.

4.9.7 Ohnesorge number calculation

The Ohnesorge number (Oh), calculated using the following equation, gives an indication of the printability of the ink [49].

$$Oh = \frac{\sqrt{We}}{Re} = \frac{\eta}{\sqrt{\sigma\rho d}}$$

Reis et al. [50] showed that the stable interval of droplet formation stability is comprised in the range $1 < Z\ (= 1/Oh) < 10$. If $Z < 1$, viscous dissipation prevents the drop ejection from the nozzle while if $Z > 10$, unwanted satellite drops are formed.
For the P25_B1000, the experimental data used for the Oh calculation were:
Viscosity (η) = 6.9 mPas (at 1000 1/s)
Surface tension (σ) = 30.9 mN/m
Characteristic length (d) = 50 µm
The ink density, 1.06 g/cm^3, was approximated using the formula $\rho = \sum \rho i . \frac{Vi}{Vtot}$ and hypothesizing that no contraction, dilatation or reaction occur in the media.

The obtained Oh is equal to 0.171 that corresponds to a Z value of 5.85. The ink is therefore definitely inside the aforementioned printability limits [51].

4.10 Inkjet printing process

Considering the rheological and stability properties and the relative good value of Oh, the P25_B1000 was considered for some printing trials using the MD-K-130 printhead. In this device, the voltage pattern is a single pulse (Figure 4.45) divided in three steps: the time to rise from 0 to the desired voltage V (t_{rise}), the time during which the voltage V is maintained (t_{dwell}) and the time to decrease from V to 0 (t_{fall}) [52].

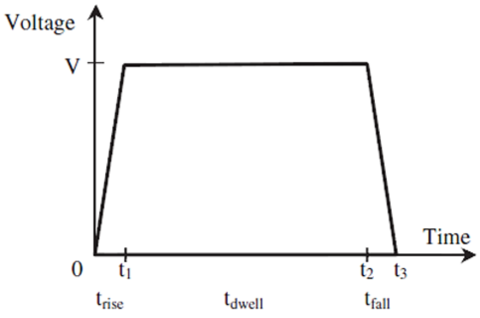

Figure 4.45. Pattern of a single pulse [50]

The first increase in voltage creates a negative pressure in the liquid (Figure 4.46 A) that is represented in this scheme, below the horizontal line while a positive one is illustrated above the line. This negative pressure is split in two parts and each part propagates in opposite directions with the same amplitude equal to the half of the initial pressure (Figure 4.46 B). The ink reservoir acts as an open end and the acoustic wave return as a positive pressure wave whereas the end of the nozzle acts as a close end and the acoustic wave returns as a negative pressure wave (Figure 4.46 C). When the voltage falls from V to 0, a positive pressure is generated (Figure 4.46 D). So, the positive wave pressure returning from the open end (liquid reservoir) is doubled and the negative pressure coming from the close end is annihilated. Thus, it remains a positive wave pressure which ejects the fluid outside the nozzle (Figure 4.46 E) [52,53].

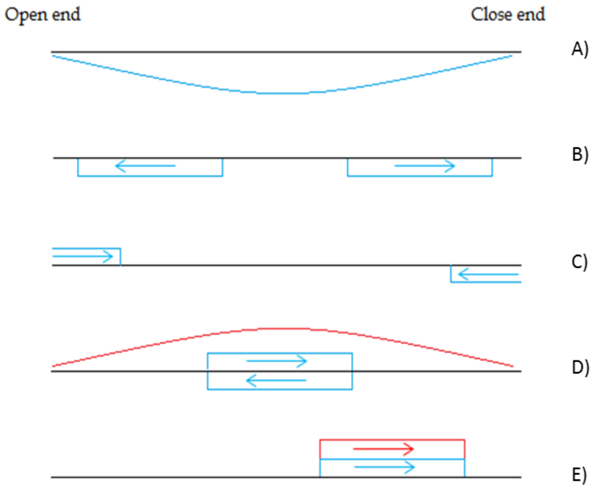

Figure 4.46. Draw of acoustic wave in a microchannel adapted from [49,50]

The different controllable printing parameters of the MD-K-130 are the pulse duration, the pulse voltage and the frequency. The set of these parameters, particularly the pulse duration, is closely linked to the mechanism described in Figure 45. Indeed, the velocity of the acoustic wave is a property of each ink. Thus, there is an optimal value for the pulse duration, where the generated positive pressure wave coincided with the arrival of the two initial pressure waves (Figure 4.46 D). Figure 4.46 D exhibits the optimal configuration which enables to achieve the maximum jetting efficiency. In this case, the pulse voltage can be minimized. If the optimal pulse is not achieved, the pulse voltage has to be increased to enable the jetting of the ink. Finally, the frequency is the number of voltage pulse per second [52,53].

The printing parameters were firstly set in order to obtain well-defined single droplets using deionized (DI) water and then ethanol. In Figure 4.47, some test images are reported and then discussed (all the trials and the corresponding parameters are in Appendix 6).

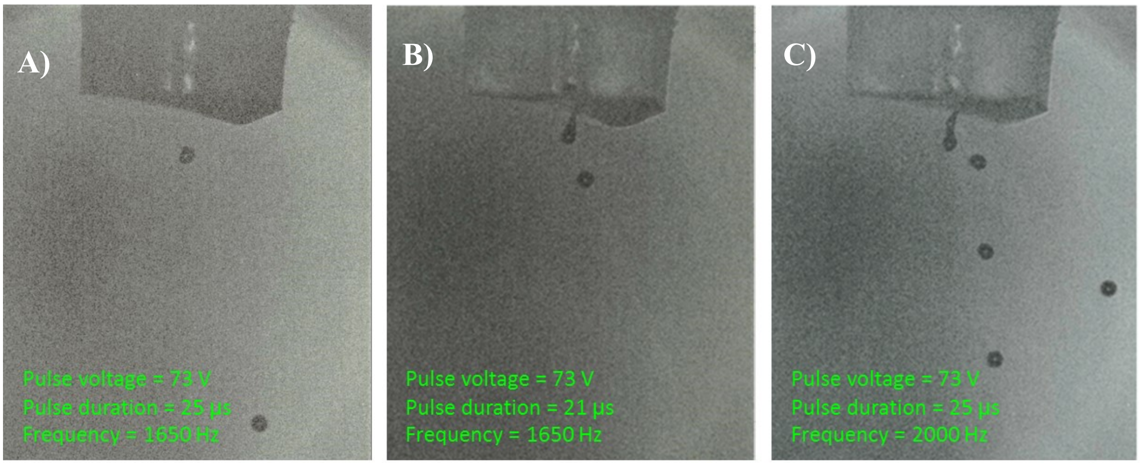

Figure 4.47. DI water droplets ejections obtained varying some process parameters; A) suitable conditions, B) and C) non-optimized ones

Single droplets of water can be ejected by nozzle; the best parameters combination is a pulse voltage of 73 V, with a duration of 25 µs and frequency of 1650 Hz (Figure 4.47 A). The last two photos show the ejection in non-optimized conditions. Figure 4.47 B shows the DI water ejection for a pulse duration that is too low; the liquid filament does not lead to a single drop but is divided in two droplets. A frequency too high on the other hand (Figure 4.47 C), causes the formation of satellite drops (that are additional drops typically smaller than the intended ones, resulting from the collapse of the liquid column) and several water jets with chaotic directions.

It is interesting to notice that DI water is characterized by an Oh number (calculated considering viscosity, surface tension, density and characteristic length equal to 1 mPas, 72 mN/m, 1 g/cm^3 and 50 µm respectively) of 0.017 (Z = 59) which is much higher than the theoretical value of 0.1 (Z = 10) considered suitable for printing. This behavior is due to the difficulty of linking the printability of an ink to strict theoretical parameters for the high number of variable influencing the process. The same sort of uncertainty is reflected on variability of results found in literature for similar systems. [51,52]. Thus, even if the Oh value can give an indication of the system processability, its actual printability is not so easily predictable. Additionally, the results coming from literature are not easily transferable as the process strongly depend on the nature of the print head used; with different printing heads, different setting parameters are required.

4.10.1 Inkjet depositions using P25_B1000 ink

The ink was loaded in the ink reservoir just after its formulation and a double filtration step using 5 and 0.8 µm filters. This step of the process is commonly introduce even commercially to reduce the risk of nozzle clogging. DLS analyses (Figure 4.48) were then performed (diluting 500 times the ink) on the system.

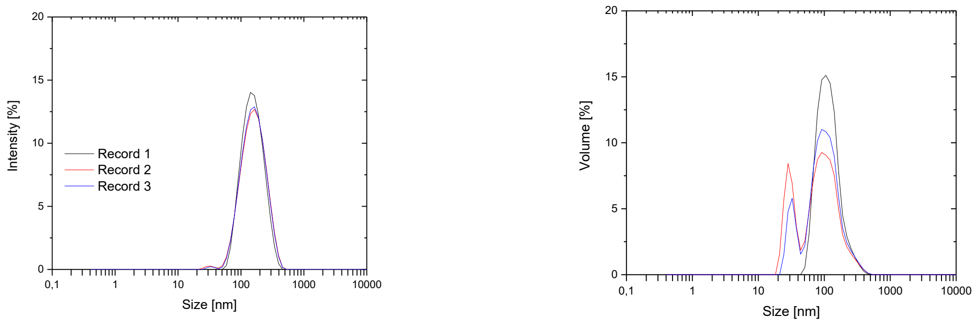

Z-Ave = 142.1 ± 0.9 nm PDI = 0.163 ± 0.012

Figure 4.48. P25_B1000 suspension size distribution by intensity and volume just before the jetting

According to the previous DLS analysis, no micrometer sized agglomerates are present and the range of particles size is between 20 to 500 nm, therefore suitable for the process. The ink was then employed to deposit some droplet using the same parameter set with water as first trial. As partially expected, these parameters were not suitable for the process. Different combinations of parameters were unsuccessfully tested as a consequence of nozzle clogging. A couple of procedures were implemented trying to fix this issue: (i) inkjet loop washing with fresh solvents, mainly warm water and ethanol (ii) forcing some air, using a syringe, from the nozzle tip towards the ink tank aiming at push back the agglomerates, but both were ineffective. Various phenomena can be responsible for the clogging even with stable ink formed by particles and aggregates well below the nozzle dimension. The ink behaviour inside a micro-channel is difficult to anticipate because the conditions really differ in respect to the ones inside the reservoir. Firstly, the shear rate during the ejection is very high: according to Wang et al., [54] it is on the order of 10^5 s^{-1} for the first few microseconds but then quickly drops to 10^4 s^{-1} after about 15 µs. This high shear rates can induce gelation in colloidal system especially the one based on titanium oxide quite well known for its peptization attitude. The energetic barrier preventing the agglomeration can be lower at high shear rates. The critical shear rate at which this barrier is overcomes marks the transition from a slow agglomeration regime to a fast one [55,56]. In these conditions, colloidal systems that are well stabilized by electrostatic repulsive forces can collapse and transformed into solid-like gels. Another phenomenon that can clog the nozzle is called hydrodynamic bridging and it is due by the simultaneous arrival of stable and suitable sized particles at the nozzle. If the velocity is high enough, particles-particles interactions can be overcome resulting in formation of a particle bridge across the entrance [57]. However, this phenomenon might lead to reversible nozzle blocking that can be restore using some unblocking procedures, while in our system the nozzle was irreversibly stacked. Another possible reason for the clogging could be linked to the high evaporation rate of the ink in the nozzle tip that lead to its partial drying and consequent blocking of the deposition system [58]. Finally, Lee et al. [59] reported an effect of heterocoagulation of nanoparticles with larger ones; the latter act as nuclei for the agglomeration leading to systems that could reach dimensions critical for the inkjet nozzle.

All these possible effects are linked to the aqueous media and the electrostatic interaction between the particles in this media. For these reasons, an attempt to disperse the TiO_2 powder in an organic media was made.

4.11 Organic solvent-based inkjet ink for micro-pillars deposition

The activities reported in this chapter are related to the work done in collaboration with a company expert in ink formulation and interested in developing 3D structures. The work previously presented on water-based system was considered by the company as a starting point for a collaboration on the subject.

For this reason, the knowledge acquired before was matched with the company expertise to jointly start the activity on the organic-based system. A new formulation based on coconut oil (viscosity of about 4 - 5 mPas at 25°C) was therefore designed. The dispersant, here indicated as FJ5, is an ad-hoc product used from this company to disperse ceramic particles in organic solvent. The ink composition is reported in Table XXIV.

Table XXIV. Ink VC_0 formulation

Material	Function	Vol.%
TiO_2 (P25, Degussa)	Active phase (solid fraction)	11.74
IBC	Solvent	84.28
FJ5	Dispersant	3.98

The suspension obtained after mixing under magnetic stirring (at 250 rpm for 15 minutes) the dispersant and the TiO_2 showed sedimentation just after 10 minutes suggesting the presence of big powder agglomerates. This assumption was confirmed by particle size analyses (Table XXV) performed with the company Mastersizer 3000 (Malvern, UK).

Table XXV. Ink VC_0 particles size as a function of the milling treatment

Sample	Dv(10) [µm]	*Dv(50) [µm]	Dv(90) [µm]
Ink VC_0	0.146	1.97	19.6
Ink VC_0_BM30’	0.145	1.53	7.24
Ink VC_0_BM60’	0.134	1.11	4.44
Ink VC_0_GM60’	0.031	0.064	0.123

* Mastersizer Dv50 parameter is nearly equivalent to the DLS Z-Ave one

The Ink VC_0 sample shows a Dv(50) (which signifies the point in the size distribution, up to and including which, 50% of the total volume of material in the sample is contained) equal to 2 µm that is completely unsuitable for the target application. Therefore, the grinding protocol commonly considered by the company to prepare their formulations (constituted by a ball-milling (BM) process of 1h then followed by 1h powerful treatment (1,5 kW/h) in a grinding mill (LabStar, NETZSCH-Feinmahltechnik GmbH, Germany) was applied to this ink. The particles distribution reported in Table XXV is enormously reduced clear confirmation of the process efficiency; the Dv(50) (64 nm) is closed to the particle size reported by the powder supplier (25 nm). The system stability was even more confirmed by the size distribution values that remained unchanged after 3 hours.

The depositions with this ink were not done using the previous printhead, but an industrial one in which is also possible to control the nozzle temperature. For this reason, measurement of viscosity as a function of the temperature were also performed (Figure 4.49).

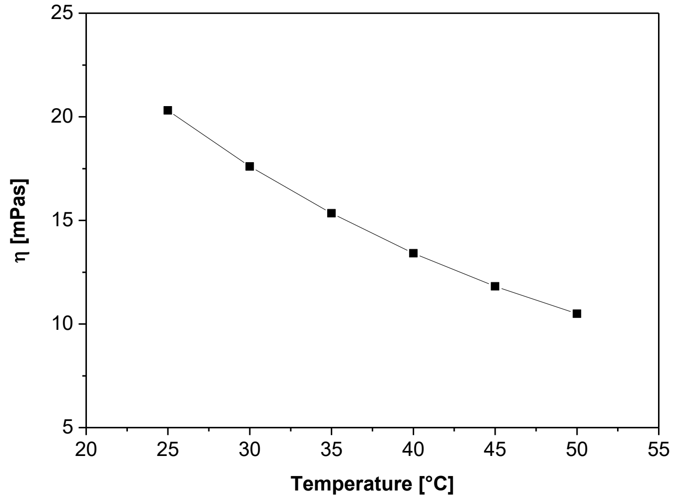

Figure 4.49. Ink VC_0 viscosity vs temperature

This analysis was carried out imposing a shear rate of 50 s^{-1} (using the CP 2/60 geometry with a 72 μm gap between the plates). The recommended range of suitable viscosities of the considered printhead is between 10 and 14 mPas, therefore, the lowest temperature to be set is equal to 40°C. Although higher temperatures lead to less viscous systems, mild conditions are suggested to preserve the equipment and reduce the process costs. Table XXVI reports the main characteristics of the industrial inkjet printhead (StarFire SG1024/MC, Fujifilm, Dimatix) used to deposit the Ink VC_0.

Table XXVI. StarFire SG1024/MC printhead main characteristics

Characteristic	**Value / Description**
Number of nozzle	1024
Ink operating temperature range	Up to 60°C
Viscosity range (at jetting T°)	8 - 20 mPas (10 - 14 recommended)
Compatible jetting fluids	Oil based ceramic inks
Drop size	26 – 65 pl
RediJet™ technology	Continuous ink recirculation

If compared with the previous printhead (MD-K-130), the StarFire one shows three interesting advantages: (i) the number of available nozzles is enough to cover wide substrates with a single deposition step (ii) the nozzle can be heated up to 60°C allowing the formulation of high-viscous inks (and consequently high-solid loaded systems) that can be printed when they reach the suitable viscosity just after heating (iii) the continuous ink recirculation guarantees ink printability for extended periods of time, greatly reducing the particles sedimentation phenomena and hence the possibility of nozzle failure.

At this stage of the work, a simple deposition pattern was designed; it is represented by a full-area printing pattern in order to check the concrete ink printability. The as-produced deposition on FTO glass was then sintered at 450°C for 30 minutes in order to consolidate the deposition and analyse the microstructure (Figure 4.50).

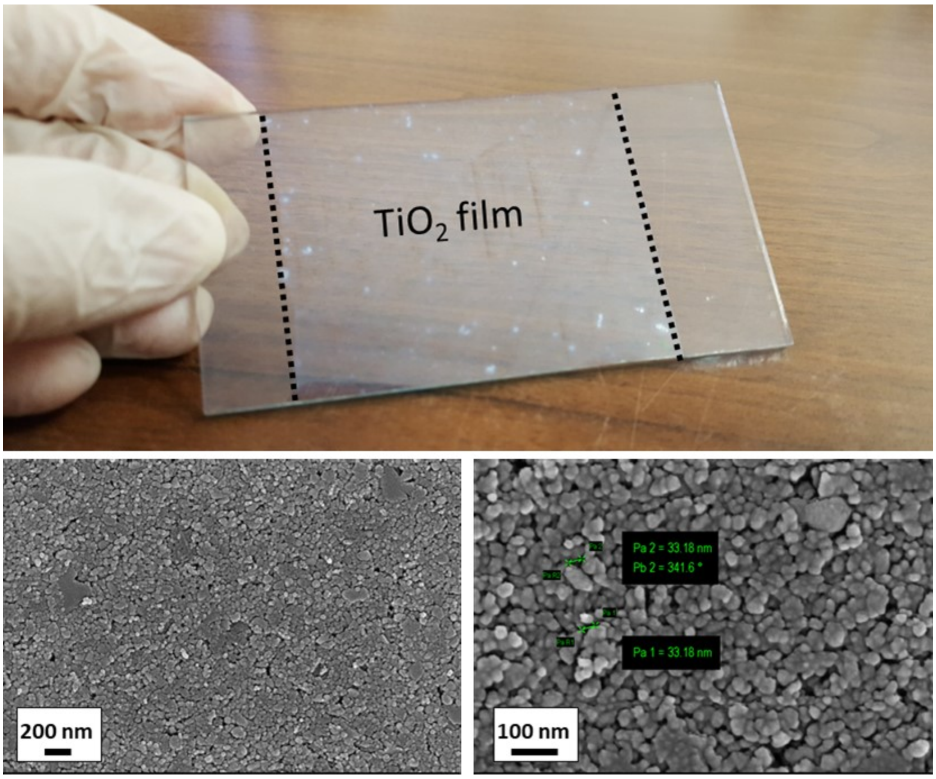

Figure 4.50. Sintered inkjet deposition of Ink VC_0 on a FTO glass and relative micrographs at different magnifications

Figure 4.50 shows a quite transparent film (notable macroscopic defects are formed by dust) were P25 nanoparticles are well dispersed and the porosity is homogeneously distributed; the mean pore dimensions, evaluated at the highest magnification, are around 30 nm that is quite similar to ones obtained for sprayed films (Figure 4.10 B).

The solvent-based formulation has proven to have the right requirements to be applied by inkjet. Although more work must be done to reach the envisaged 3D structures, these primary results are very encouraging: the obtained deposition shows an appropriate microstructure for the desired application while the ink used is stable for the process duration. To obtain 3D structures, a binder must be added to the formulation to assure high aspect ratio structures and proper additives, to increase the ink wettability onto the substrate, will be considered.

References

[1] R. D. Deegan, O. Bakajin, T. F. Dupont, G. Huber, S. R. Nagel, T. A. Witten, *Capillary flow as the cause of ring stains from dried liquid drops*, Nature, 1997, 389, 827-829.

[2] P. J. Yunker, T. Still, M. A. Lohr, A. G. Yodh, *Suppression of the coffee-ring effect by shape-dependent capillary interactions*, Nature, 2011, 476, 308-311.

[3] J. Vermant, *Fluid mechanics: When shape matters*, Nature, 2011, 476, 286-287.

[4] L. Zhao, *Manufacture and characterization of composite graded filter membranes for microfiltration*, PhD thesis, 2003, Forschungszentrum Jülich reports, JüL-4079.

[5] L. Lopez, W. A. daoud, D. Dutta, *Preparation of large scale photocatalytic* TiO_2 *films by the sol-gel process*, Surface & Coatings Technology, 2010, 205, 251-257.

[6] J. Halme, J. Saarinen, P. Lund, *Spray deposition and compression of* TiO_2 *nanoparticle films for dye-sensitized solar cells on plastic substrates*, Solar Energy Materials & Solar Cells, 2006, 90, 887-899.

[7] M. K. Nazeeruddin, A. Kay, I. Rodicio, R. H. Baker, E. Müller, P. Liska, N. Vlachopoulos, M. Grätzel, *Conversion of light to electricity by cis-Ruthenium on nanocristalline* TiO_2 *electrodes*, Journal of the America Chemical Society, 1993, 115, 6382-6390.

[8] M. Grätzel, *Perspectives for dye-sensitized nanocrystalline solar cells*, Progress in Photovoltaics: Research and Applications, 2000, 8, 171-185.

[9] B. O’Regan, M. Grätzel, *A low-cost, high-efficiency solar cell based on dye-sensitized colloidal* TiO_2 *films,* Nature, 1991, 353, 737-740.

[10] A. Hagfeldt, M. Grätzel, *Molecular Photovoltaics*, Accounts of chemical research, 2000, 33, 269-277.

[11] A. Fillinger, B. A. Parkinson, *The Adsorption Behavior of a Ruthenium-Based Sensitizing Dye to Nanocrystalline TiO2 - Coverage Effects on the External and Internal Sensitization Quantum Yields*, Journal of the Electrochemical Society, 1999, 146, 4559-4564.

[12] T. H. Meen, C. J. Huang, Y. W. Chen, L. W. Ji, C. C. Diao, H. H. Chung, *Study of Different* TiO_2 *Electrode Structures on Dye-Sensitized Solar Cell,* Key Engineering Materials, 2008, 368-372, 1716-1719.

[13] K. Sato, J. G. Li, H. Kamiya, T. Ishigaki, *Ultrasonic dispersion of* TiO_2 *nanoparticles in aqueous suspension*, Journal of the American Ceramic Society, 2008, 91, 2481-2487.

[14] N. A. El-Zaher, W. G. Osiris, *Thermal and structural properties of poly(vinyl alcohol) doped with hydroxypropyl cellulose*, Journal of Applied Polymer Science, 2005, 96, 1914-1923.

[15] W. G. Osiris, M. T. H. Moselhey, *Optical study of poly(vinyl alcohol)/hydroxypropyl methylcellulose blends*, Journal of Materials Science, 2011, 46, 5775-5789.

[16] A. Sanson, D. Gardini, G. Montanari, C. Galassi, E. Roncari, *Key role of milling in the optimization of* TiO_2 *nanoinks*, Journal of Materials Research, 2006, 21, 1561-1569.

[17] C. Zhu, J. E. Smay, *Thixotropic rheology of concentrated alumina colloidal gels for solid freeform fabrication*, Journal of Rheology, 2011, 55, 655-672.

[18] C. Zhu, T. Y. J. Han, E. B. Duoss, A. M. Golobic, J. D. Kuntz, C. M. Spadaccini, M. A. Worsley, *Highly compressible 3D periodic graphene aerogel microlattices,* DOI: 10.1038/ncomms7962.

[19] W. D. A. Rickard, A. van Riessen, P. Walls, *Thermal Character of Geopolymers Synthesized from Class F Fly Ash Containing High Concentrations of Iron and α-Quartz*, International Journal of Applied Ceramic Technology, 2010, 7, 1, 81–88.

[20] K. Sun, T. S. Wei, B. Y. Ahn, J. Y. Seo, S. J. Dillon, J. A. Lewis, *3D Printing of Interdigitated Li-Ion Microbattery Architectures*, Advanced Materials, 2013, 25, 4539-4543.

[21] T. P. Chou, Q. Zhang, G. E. Fryxell, G. Z. Cao, *Hierarchically Structured ZnO Film for Dye-Sensitized Solar Cells with Enhanced Energy Conversion Efficiency,* Advanced Materials, 2007, 19, 2588-2592.

[22] S. Ngamsinlapasathian, T. Sreethawong, Y. Suzuki, S. Yoshikawa, *Single- and double-layered mesoporous* TiO_2*/P25* TiO_2 *electrode for dye-sensitized solar cell*, Solar Energy Materials & Solar Cells, 2005, 86, 269–282.

[23] S. Ito, S. M. Zakeeruddin, R. Humphry-Baker, P. Liska, R. Charvet, P. Comte, M. K. Nazeeruddin, P. Péchy, M. Takata, H. Miura, S. Uchida, M. Grätzel, *High-Efficiency Organic-Dye-Sensitized Solar Cells Controlled by Nanocrystalline-*TiO_2 *Electrode Thickness*, Advanced Materials, 2006, 18, 1202-1205.

[24] M. K. Nazeeruddin., A. Kay, I. Rodicio, R. Humphry-Baker, E. Mueller, P. Liska, N. Vlachopoulos, M. Gräzel, *Conversion of light to electricity by cis-X2bis(2,2'-bipyridyl-4,4'dicarboxylate) ruthenium(II) charge-transfer sensitizers (X = Cl-, Br-, I-, CN- and SCN-) on nanocrystalline titanium dioxide electrodes*, Journal of the American Chemical Society, 1993, 115, 6382-6390.

[25] S. Sarker, A. J. Saleh Ahmmad, H. W. Seo, D. M. Kim, *Electrochemical impedance spectra of Dye-sensitized Solar Cells: fundamentals and spreadsheet calculation*, International Journal of Photoenergy, 2014.

[26] X. Lu, X. Mou, J. Wu, D. Zhang, L. Zhang, F. Huang , F. Xu, S. Huang, *Improved-performance dye-sensitized solar cells using Nb-doped TiO_2 electrodes: efficient electron injection and transfer*, Advanced Functional Materials, 2010, 20, 509-515.

[27] B. Hu, Q. Tang, B. He, L. Lin, H. Chen, *Mesoporous TiO_2 anodes for efficient dye-sensitized solar cells: an efficiency of 9.86% under one sun illumination*, Journal of Power Sources, 2014, 267, 445-451.

[28] A. Reynal, A. Fornelli, E. Palomares, *Dye structure-charge transfer process relationship in efficient ruthenium-dye based dye sensitized solar cells*, Energy & Environmental Science, 2010, 6, 805-812.

[29] S. H. Othman, S. A. Rashid, T. I. M. Ghazi, N. Abdullah, *Dispersion and stabilization of photocatalytic TiO_2 nanoparticles in aqueous suspension for coatings applications,* Journal of Nanomaterials, 2012, 2012, 1-10.

[30] C. Jacobs, O. Kayser, R. H. Müller, *Nanosuspensions as a new approach for the formulation for the poorly soluble drug tarazepide,* International Journal of Pharmaceutics, 2000, 196, 161-164.

[31] A.D. McNaught, A. Wilkinson, *IUPAC: Compendium of Chemical Terminology*, 2nd ed. Oxford, Blackwell Scientific Publications, 1997.

[32] S. Fazio, J. Guzman, M. T. Colomer, A. Salomoni, R. Moreno, *Colloidal stability of nanosized titania aqueous suspensions*, Journal of the European Ceramic Society, 2008, 28, 2171-2176.

[33] K. Suttiponparnit, J. Jiang, M. Sahu, S. Suvachittanont, T. Charinpanitkul, P. Biswas, *Role of surface area, primary particle size, and crystal phase on titanium dioxide nanoparticle dispersion properties,* Nanoscale Research Letters, 2010, 6, 1.

[34] N. Wang, C. Hsu, L. Zhu, S. Tseng, J. P. Hsu, *Influence of metal oxide nanoparticles concentration on their zeta potential*, Journal of colloid and interface science, 2013, 407, 22-28.

[35] A. Gajović, K. Furic, S. Music, *Ball milling of TiO_2 and ZrO_2*, Progress in Advanced Materials Science through Electron Microscopy, Berlin: s.n., 2002.

[36] N. Mandzy, E. Grulke, T. Druffel, *Breakage of TiO_2 agglomerates in electrostatically stabilized aqueous dispersions*, Powder technology, 2005, 160, 121-126.

[37] S. Sen, V. Govindarajan, C. J. Pelliccione, J. Wang, D. J. Miller, E. V. Timofeeva, *Surface Modification Approach to TiO_2 Nanofluids with High Particle Concentration, Low Viscosity, and Electrochemical Activity*, ACS applied materials & interfaces, 2015, 7, 20538-20547.

[38] F. Fiévet,, R. Brayner, *Nanomaterials: a danger or a promise? A chemical and biological perspective*, London: Springer, 2013.

[39] P. Leroy, C. Tournassat, M. Bizi, *Influence of surface conductivity on the apparent zeta potential of TiO_2 nanoparticles*, Journal of Colloid and Interface Science, 2011, 356, 442-453.

[40] G. L. Güngör, A. Kara, D. Gardini, M. Blosi, M. Dondi, C. Zanelli, *Ink-jet printability of aqueous ceramic inks for digital decoration of ceramic tiles*, Dyes and Pigments, 2016, 127, 148-154.

[41] A. Karagunduz, K. D. Pennell, M. H. Young, *Influence of a nonionic surfactant on the water retention properties of unsaturated soils*, Soil Science Society of America Journal, 2001, 65, 1392-1399.

[42] D. Kuscer, G. Stavber, G. Trefalt, M. Kosec, *Formulation of an Aqueous Titania Suspension and its Patterning with Ink-Jet Printing Technology*, Journal of the American Ceramic Society, 2012, 95, 487-493.

[43] J. R. Evans, M. J. Edirisinghe, J. H. Song, *Direct Ink-Jet Printing of Vertical Walls*, Journal of the American Ceramic Society, 2002, 85, 2113-2115.

[44] M. P. Albano, L. A. Genova, L. B. Garrido, K. Plucknett, *Processing of porous yttria-stabilized zirconia by tape-casting*, Ceramics International, 2008, 34, 1983-1988.

[45] H. F. Mark, N. M. Bikales, C. G. Overberger, G. Menges, J. I. Kroschwitz, *Encyclopedia of Polymer Science and Engineering*, Vol 8, 2nd edn, New York: John Wiley & Sons Inc, 1985-1987.

[46] A. Kristoffersson, E. Roncari, C. Galassi, *Comparison of different binders for water-based tape casting of alumina*, Journal of the European Ceramic Society, 1998, 18, 2123-2131.

[47] M. Lejeune, T. Chartier, C. Dossou-Yovo, R. Noguera, *Ink-jet printing of ceramic micro-pillar arrays*, Journal of the European Ceramic Society, 2009, 29, 905-911.

[48] I. Bernacka-Wojcik, P. J. Wojcik, H. Aguas, E. Fortunato, R. Martins, *Inkjet-printed highly porous TiO_2 films for improved electrical properties of photoanode,* Journal of colloid and interface science, 2016, 465, 208-214.

[49] M. Mikolajek, A. Friedrich, W. Bauer, J. R. Binder, *Requirements to ceramic suspensions for inkjet printing*, Ceramic Forum International, 2015, 92 (3), E25-29.

[50] N. Reis, B. Derby, *Inkjet deposition of ceramic suspensions: Modeling and experiments of droplet formation,* MRS proceedings, Cambridge University Press., 2000, 625, 117.

[51] J. Tai, H. Y. Gan, Y. N. Liang, B. K. Lok, *Control of droplet formation in inkjet printing using Ohnesorge number category: materials and processes*, In Electronics Packaging Technology Conference, 2008, 761-766.

[52] H. C. Wu, T. R. Shan, W. S. Hwang, H. J. Lin, *Study of micro-droplet behaviour for a piezoelectric inkjet printing device using a single pulse voltage pattern,* Materials transactions, 2004, 45, 1794-1801.

[53] H. Wijshoff, *Manipulating drop formation in piezo acoustic inkjet*, NIP 22: 22nd International Conference on Digital Printing Technologies, Society for Imaging Science and Technology, 2006, 79-82.

[54] X. Wang, W. W. Carr, D. G. Bucknall, J. F. Morris, *Drop-on-demand drop formation of colloidal suspensions*, International Journal of Multiphase Flow, 2012, 38, 17-26.

[55] A. Zaccone, H. Wu, D. Gentili, M. Morbidelli, *Theory of activated-rate processes under shear with application to shear-induced aggregation of colloids,* Physical Review E, 2009, 80, 051404.

[56] D. Xie, H. Wu, A. Zaccone, L. Braun, H. Chen, M. Morbidelli, *Criticality for shear-induced gelation of charge-stabilized colloids*, Soft Matter, 2010, 6, 2692-2698.

[57] V. Ramachandran, H. S. Fogler, *Plugging by hydrodynamic bridging during flow of stable colloidal particles within cylindrical pores*, Journal of Fluid Mechanics, 1999, 385, 129-156.

[58] D. M. Nikipanchuk, Z. M. Yaremko, L. B. Fedushinskaya, *Interparticle interactions in titanium dioxide dispersions*, Colloid journal of the Russian Academy of Sciences, 1997, 59, 324-328.

[59] A. Lee, K. Sudau, K. H. Ahn, S. J. Lee, N. Willenbacher, *Optimization of experimental parameters to suppress nozzle clogging in inkjet printing,* Industrial & Engineering Chemistry Research, 2012, 51, 13195-13204.

Chapter 5

Conclusions and future works

An important contribution to the improvement of current energy and environmental issues could derive from the sun. The latter can be concretely exploited for a “green” energy production, through photovoltaic devices. This was the field of main interest for the activities carried out during this PhD program.

More in detail, the attention was focused on Dye-sensitized Solar Cells (DSCs) which have attracted a considerable interest in the last decades as a cost-effective, environmental-friendly and highly versatile technology, complementary to traditional silicon-based photovoltaics. TiO_2 is largely known to be the most suitable semiconductor for this application, thus it was considered as model material for this study. It was deposited in the form of both supported nanocrystalline mesoporous layer and micro-pillars by a combination of fully-automated innovative deposition technologies (WPS and micro-extrusion/inkjet printing), were coupled allowing the production of 3D engineered DSC photoanodes with improved performance. The latter were mainly ascribed to the increased photoanode surface area and therefore, higher availability for the dye adsorption and electrolyte penetration, and, to the presence of preferential tracks (micro-pillars) for the electrons towards the electrode.

The following results were obtained during this PhD thesis:

- High-transparent mesoporous TiO_2 films were obtained through WPS technique. The target was properly pursued firstly optimizing, in terms of stability and substrate/suspension interactions, a modified commercial aqueous-based colloidal TiO_2 suspension; after that, the main deposition process parameters were properly set. In detail, the suspension stability was investigated through DLS and ζ potential analysis during the addition of different amounts of pure water. The diluted system (PC-S7_5) was selected as WPS suspension as a consequence of the best compromise between stability (suitable Z-Ave, PDI and ζ potential values), homogeneous substrate coverage (strong “coffee stain” effect avoided) and TiO_2 content. The impact of the main process parameters (fluid flow, Z and the number of consecutive depositions) on the film quality was investigated by optical and electronic microscopy, interferometry and transmittance analysis. The most performing TiO_2 mesoporous sprayed layer showed definite improving in the substrate coverage. The low Ra (roughness parameter) indicated a very smooth surface also confirmed by the optical and SEM images. A highly mesoporous microstructure was observed and its great transparency was confirmed by a T% of about 95%. The film thickness was estimated around 3 µm while its tendency to host sensitizer molecules was determined through adsorption capability tests. The sprayed TiO_2 film showed an improved dye adsorption capability and photovoltaic performances than a common screen-printed film having same area and thickness.

- 3D coarse micro-pillars were deposited on the optimized WPS film using the micro-extrusion technique. The ink formulation was optimized considering (i) high concentrated TiO_2 powder-based inks and (ii) TiO_2 colloidal suspension-based inks, then, the main deposition process parameters were adequately set.

  Powder-based inks: the initial TiO_2 content was set at 6 vol.%. Different milling processes were investigated in order to produce well-dispersed systems avoiding powder agglomerates as well as different cellulose (HEC, HPC) blends to tune their rheology. In particular the ultrasonic horn technique (USH) was proved to be the most effective one, also confirmed by DLS measurements (Z-Ave and PDI). The rheological properties of the obtained inks indicated that, the higher viscous system was the one containing higher amount of HEC; the latter also showed suitable G' and G'' indicating a well-structured ink. However, the viscosity absolute values were at least one order of magnitude lower than what needed to properly design tridimensional objects. The TiO_2 amount was, therefore, augmented up to 13 vol.%.

  A planetary centrifugal mixer (Thinky) allowed to obtain an ink with suitable rheology and therefore used for micro-extrusion trials. However reducing the nozzle diameters down-to 250, 200 and 50 µm, the material flowed outside discontinuously due to the presence of TiO_2 powder/cellulose indissoluble soft agglomerates that partially occlude the nozzle. To overcome this issue, a TiO_2 colloidal suspensions was considered.
- _Colloidal suspension-based inks:_ the initial TiO_2 content was set at 5 vol.% and two different amounts (4.70 and 5.60 wt.%) of cellulosic blend were investigated. Among all these inks, the one containing the HEC-enriched blend showed the best rheological characteristics (highest viscosity with pronounced pseudoplastic behavior and G' > G'') due to a proportional enhancement of the network rigidity induced by an increased amount of HEC. Micro-pillars, with a highly porous microstructure and a mean aspect ratio of about 0.060 were obtained using an home-made deposition apparatus. Consequently DSC prototypes, constituted by 3D engineered photonoades were built and characterized.

- The mean DSCs efficiency value with sprayed films was around 2.4% while it exceeded 3.0 % for the ones with 3D structures. The augmented performances were due to a progressive increase in both the current density and open circuit voltage (Voc). The Voc improvements indicated a lower number of recombination phenomena as confirmed by the respective dark curve analysis. Regarding the IPCE measurements of the prototype with the engineered photoanode, the maximum conversion efficiency was about 30%. This improvement was mainly ascribed to the perfected properties of the electrode containing the micro-pillars and, secondly, to its higher dye loading capability. Electrochemical Impedance Spectroscopy (EIS) was then used and the obtained results, particularly the reduced charge transfer resistance (Rct), indicated an improvement of the charge transport and then of the generated photocurrent. Finally, from EIS data, the photoanode capacitance was calculated showing values that suggested a beneficial effect in terms of photoanode capability to host an higher amount of electrons.
- For the sake of pushing the performance it was important to consider other possible ceramic techniques able to give higher aspect ratio structures of smaller dimensions. In this context, the MJ (based on DoD Inkjet) technique was investigated. The development of a ceramic aqueous-based ink, which was composed by pure anatase TiO_2 powder, water (with controlled pH), dispersant and surfactant, was carried out. pH and dispersant were used to effectively stabilized the suspension as confirmed by DLS analysis. However, some micrometric aggregates were still present even if a ultrasonication treatment was applied. For this reason, another TiO_2 powder possessing higher surface area (P25, Degussa) was investigated. The obtained formulation (TiO_2 2 Vol.%) showed a suitable viscosity but with a surface tension unsuitable for inkjet process (typically 20 - 45 mN/m). A non-ionic surfactant, able to lower the surface tension, was added and, at the same time, an acrylic latex binder emulsion was mixed with the ink. After having determined the proper amount of the latter, a suitable ink was definitely obtained (P25_B1000). It showed suitable viscosity, surface tension and moreover, its calculated Ohnesorge number (Oh) given promising indication about the printability. Once the P25_B1000 ink was loaded in the printhead, different combinations of parameters were unsuccessfully tested as a consequence of nozzle clogging. Various phenomena were identified as possible responsible: (i) induced gelation of the colloidal system, (ii) particles hydrodynamic

bridging, (iii) solvent high evaporation rate and (iv) nanoparticles heterocoagulation. All these effects were linked to the aqueous media and the electrostatic interaction between the immersed nanoparticles. For these reasons, an attempt to disperse the TiO_2 powder in an organic media was made.

An high-loaded preliminary P25 ink (12 Vol.%) was produced (Ink VC_0) in collaboration with a company. An optimal powder dispersion was achieved also thanks to a stronger grinding protocol composed of ball-milling and grinding mill processes and a proper dispersant. The adopted procedure enormously reduced the particles size, clear confirmation of the process efficiency. Using an industrial printhead specifically design to deposit ceramic inks, the VC_0 ink was easily ejected realizing a full-area printing pattern that, after sintering, showed well dispersed P25 nanoparticles and an homogeneously distributed porosity. The mean pore dimensions were around 30 nm that was quite similar to ones obtained for sprayed films. This microstructure was considered appropriate for the desired applications and is a first positive collaboration outcome in the view of building high aspect ratio 3D objects.

The future activities will be devoted to deeply understanding the micro-extrusion process aiming at producing reliable high aspect ratio 3D structures using a fully automated machine. Then, the effects of different micro-pillars sizes and their reciprocal spacing on the DSCs performance will be evaluated. The aqueous inkjet ink formulations will be reconsidered in a view of a more eco-friendly deposition process. Small amount of additives or a different binder system will be introduced trying to better match the printhead requirements. Finally, the high content TiO_2 organic-based ink will be further investigated. Nowadays it possesses interesting characteristics and it is easily printable but in order to produce the envisaged 3D structures, binders must be added to the formulation to assure high aspect ratio structures. Recently, in printed electronics field, UV-curable functional inks are extremely of interest and extensively studied thus, the usage of UV-curable polymers as binder will be take into consideration. Moreover, proper additives to improve the ink wettability onto the substrate will be considered.

Acknowledgments

First of all I would like to thank Dr. Anna Tampieri for having given me the opportunity to carry out the activity at ISTEC-CNR, I would also like to thank Prof. Enrico Dalcanale for having let me attend the PhD program.

The deepest gratitude goes to my group at ISTEC-CNR, starting form Dr. Alessandra Sanson, for her support and for everything that helped me in reaching this important objective.

Thanks to Nicola (Big) and Riccardo (Ing.), with whom I shared this experience from the beginning; all this would not have been possible without you. Together we spent some great moments, laughter never missed and this is worth much more than anything else.

Thanks also to Angela, my good friend, often my confidant and personal secretary. My PhD course has also started thanks to your insistence, thank you.

Thanks to Elisa (Bradipo), Paola (P), Aurora and Daniel (Sgù), you are a great “team” and very nice persons. Your help and support was fundamental to complete this path.

My gratitude goes to all of you for your unique contribution to this experience, but most of all for having let me feel part of something more than a work team.

I would like also to thank the ISTEC staff. In particular, Daniele Dalle Fabbriche (Vecchio) and Cesare Melandri (Ciccio), with whom every morning I have breakfast discussing sports and saying bulls***s. Thank you guys. I would like to thank Dr. Elena Landi for her constant support. I know how much you “fight” for me, I am grateful to you. Finally, thank you Davide Gardini (Guru) for the useful discussion about rheology.

Giusi, Floriano, Pina and Giuliana, my family, you never stopped believing in me, no words could be enough to say thank you.

Andrea, Vincenzo, Samuele, you are brothers more than friends. Forever four knights in Malta! Ermes, you are the little one! The esquire.

The last words are for the two most important persons. For those I love and who represent “ALL”. Thank you Linda (Tes) and Amy (CuCù), for everything. I love you!

Appendixes

APPENDIX 1: WPS tests performed to realize 1 cm^2 active area depositions

Depos. Nr.	Nozzle Ø	Spray Pressure	Deposition velocity	Sample holder T°	Fluid flow (Feed rate)	Z	N° of consecutive cycles
1*	360 µm	1 bar	50 mm/s	90°C	5/24	50 mm	5
2	360 µm	1 bar	50 mm/s	90°C	5/24	60 mm	5
3	360 µm	1 bar	50 mm/s	90°C	5/24	70 mm	5
4*	360 µm	1 bar	50 mm/s	90°C	5/24	75 mm	5
5	360 µm	1 bar	50 mm/s	90°C	5/24	75 mm	8
6	360 µm	1 bar	50 mm/s	90°C	5/24	75 mm	10
7*	360 µm	1 bar	50 mm/s	90°C	5/24	75 mm	15
8	360 µm	1 bar	50 mm/s	90°C	6/24	75 mm	15
9	360 µm	1 bar	50 mm/s	90°C	6.5/24	75 mm	15
10*	360 µm	1 bar	50 mm/s	90°C	7/24	75 mm	15

*depositions discussed in Chapter 4, section 4.3

APPENDIX 2: Micro-extrusion tests performed to realize 3 cm length straight lines

Depos. Nr.	**Ink**	**Nozzle Ø [µm]**	**Extrusion modality**	**Vol. [ml]**	**Flow [ml/min]**	**Z [mm]**	**Depos. time [s]**	**Supply advance [s]**	**Deposition speed [mm/s]**
1	ECO_2_40:60	250	Quantity	1.000	3.000	0.50	10.00	0.20	1.0
2	ECO_2_40:60	250	Quantity	0.100	0.300	0.50	20.00	0.20	0.5
3	ECO_2_40:60	250	Quantity	0.100	1.000	0.50	6.00	0.20	1.7
4	ECO_2_40:60	250	Quantity	0.010	1.000	0.50	6.00	0.20	1.7
5	ECO_2_40:60	250	Quantity	0.005	1.000	0.50	6.00	0.20	1.7
6	ECO_2_40:60	250	Quantity	0.005	1.000	0.50	18.00	0.20	1.7
7	ECO_2_40:60	250	Quantity	0.005	1.000	0.50	2.00	0.20	15
8	ECO_2_40:60	250	Quantity	0.005	1.000	0.50	2.00	0.20	15
9	ECO_2_40:60	250	Quantity	0.005	1.000	0.50	2.00	1.50	15
10	ECO_2_40:60	250	Quantity	0.005	1.000	0.75	2.00	1.50	15
11	ECO_2_40:60	410	Quantity	0.005	1.000	0.75	2.00	1.50	15
12	ECO_2_40:60	410	Quantity	0.005	1.000	0.75	2.00	0.50	15
13	ECO_2_40:60	410	Quantity	0.005	1.000	0.75	2.00	1.00	15
14	ECO_2_40:60	410	Quantity	0.010	2.000	0.75	2.00	0.20	15
15	ECO_2_40:60	410	Quantity	0.010	0.100	0.75	2.00	0.20	15
16	ECO_2_40:60	410	Quantity	0.010	1.750	0.75	2.00	0.20	15
17	ECO_2_40:60	1200	Quantity	0.010	1.750	0.75	2.00	0.20	15
18	ECO_2_40:60	1200	Quantity	0.010	1.750	0.75	2.00	0.50	15

19	ECO_2_40:60	1200	Quantity	0.050	1.750	0.75	2.00	0.50	15
20	ECO_2_40:60	1200	Quantity	0.050	1.750	0.75	2.00	0.50	15
21	ECO_2_40:60	1200	Quantity	0.050	1.750	0.75	2.00	0.75	15
22	ECO_2_40:60	1200	Quantity	0.050	1.750	0.75	2.00	0.65	15
23	ECO_2_40:60	1200	Quantity	0.055	1.750	0.75	2.00	0.65	15
24	ECO_2_40:60	640	Quantity	0.055	1.750	0.75	2.00	0.65	15
25	ECO_2_40:60	640	Quantity	0.027	1.750	0.75	2.00	0.65	15
26	ECO_2_40:60	640	Quantity	0.055	1.750	0.75	2.00	0.75	15
27	ECO_2_40:60	640	Quantity	0.055	1.750	0.75	2.00	1.00	15
28	ECO_2_40:60	640	Quantity	0.055	1.750	0.75	2.00	0.75	15
29	ECO_2_40:60	640	Quantity	0.060	1.750	0.75	2.00	0.75	15
30	ECO_2_40:60	640	Quantity	0.065	1.750	0.75	2.00	0.75	15
31	ECO_2_40:60	640	Quantity	0.062	1.750	0.75	2.00	0.75	15
32	ECO_2_40:60	410	Quantity	0.062	1.750	0.75	2.00	0.75	15
33	ECO_2_40:60	410	Quantity	0.060	1.750	0.75	2.00	0.75	15
33b	ECO_2_40:60	410	Quantity	0.061	1.750	0.75	2.00	0.75	15
34	ECO_2_40:60	410	Quantity	0.062	1.750	1.00	2.00	0.75	15
35	ECO_2_40:60	410	Quantity	0.055	1.750	1.00	2.00	0.75	15
36	ECO_2_40:60	410	Quantity	0.058	1.750	1.00	2.00	0.75	15
37	ECO_2_40:60	410	Quantity	0.060	1.750	1.00	2.00	0.75	15
38	ECO_2_40:60	410	Quantity	0.030	1.750	1.00	2.00	0.75	15
39	ECO_2_40:60	410	Quantity	0.030	1.750	1.00	1.00	0.75	30

40	ECO_2_40:60	410	Quantity	0.015	1.750	1.00	1.00	0.75	30
41	ECO_2_40:60	410	Quantity	0.015	1.750	1.00	0.67	0.75	45
42	ECO_2_40:60	410	Quantity	0.015	1.750	1.00	0.50	0.75	60
43	ECO_2_40:60	410	Pulse	/	1.750	1.00	0.50	0.75	60
44	ECO_2_40:60	410	Pulse	/	1.700	1.00	0.50	0.75	60
45	ECO_2_40:60	410	Pulse	/	1.650	1.00	0.50	0.75	60
45b	ECO_2_40:60	410	Pulse	/	1.600	1.00	0.50	0.75	60
46	ECO_2_40:60	410	Pulse	/	1.600	1.00	0.50	1.00	60
47	ECO_2_40:60	410	Pulse	/	1.700	1.00	0.33	1.00	90
48	ECO_2_40:60	410	Pulse	/	1.600	1.00	0.33	1.00	90
49	ECO_2_40:60	410	Pulse	/	1.500	1.00	0.33	1.20	90
50	ECO_2_40:60	410	Pulse	/	1.475	1.00	0.33	1.40	90
51	ECO_300B	410	Pulse	/	1.650	1.00	0.50	0.75	60
52	ECO_300B	250	Pulse	/	1.650	1.00	0.50	0.75	60
53	ECO_300B	250	Pulse	/	1.500	1.00	0.50	0.75	60
54	ECO_300B	50	Pulse	/	1.500	1.00	0.50	0.75	60
55	ECO_300B	250	Pulse	/	1.500	1.00	0.50	1.00	60
56	ECO_300B	250	Pulse	/	1.000	1.00	0.50	1.30	60
57	ECO_300B	200	Pulse	/	1.000	1.00	0.50	1.30	60
58	ECO_300B	200	Pulse	/	0.950	1.00	0.50	1.30	60
59	ECO_300B	200	Pulse	/	0.950	1.00	0.50	1.30	60
60	ECO_300B	200	Pulse	/	1.500	0.25	0.33	2.00	90

61	ECO_300B	250	Pulse	/	1.500	1.00	0.33	2.00	90

Deposition Nr. 16

Deposition Nr. 18

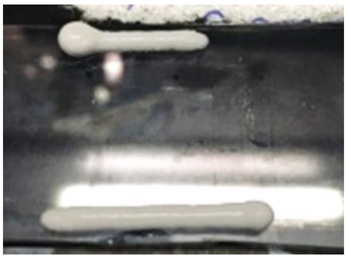

Deposition Nr. 23

Deposition Nr. 24

Deposition Nr. 31

Deposition Nr. 39

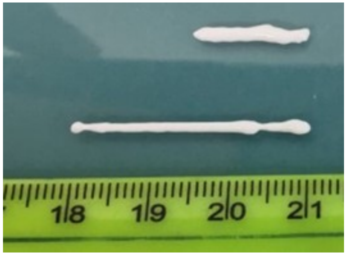

Deposition Nr. 42

Deposition Nr. 44

Deposition Nr. 46

Deposition Nr. 48

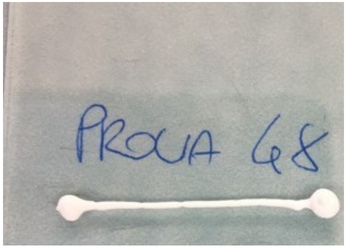

Deposition Nr. 49

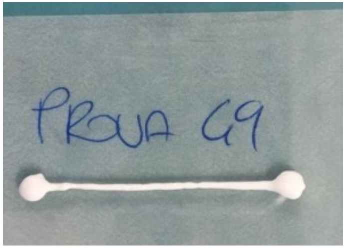

Deposition Nr. 50

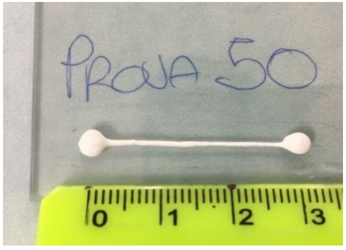

Deposition Nr. 52

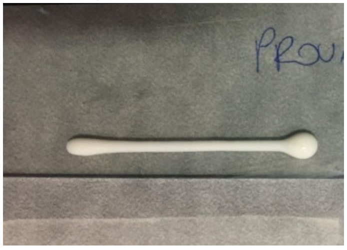

Deposition Nr. 53

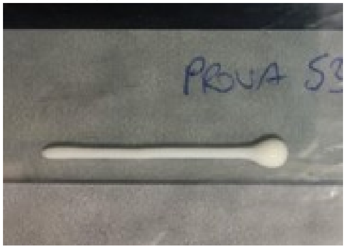

Deposition Nr. 56

Deposition Nr. 57

Deposition Nr. 58

Deposition Nr. 60

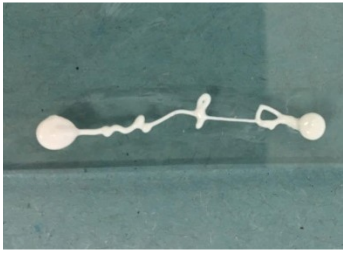

Deposition Nr. 61

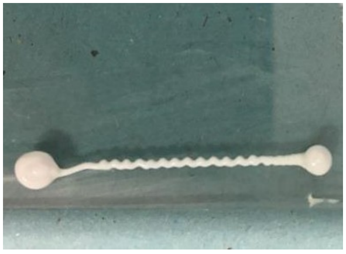

Figure APP1. Micro-extrusion deposition tests performed to realize 3 cm length straight line

APPENDIX 3: Ionic strength calculations

Influence of the ammonium added to adjust the pH

The initial solution of ammonium is at 28 wt.%. The fraction of ammonium in the suspension is equal to 0.28 and is noted F(NH4OH)

$$\mathrm{F(NH4OH)} = \frac{m(Nh4OH)}{Mtot}$$

Mtot = Vtot because the density of the solution is 1.

So,

$$\mathrm{F(NH4OH)} = \frac{n(NH4OH).M(Nh4OH)}{Vtot} = C(NH4OH).M(NH4OH)$$

With n(NH4Oh) in mol/L and M(NH4OH) in Kg/mol.

This formula gives C(NH4OH) = 8 mol/L with wt.% = 28 and M(NH4OH) = 35,04 x 10^{-3} Kg/mol. The buffer solution corresponds to the dilution at 10^{-4} of this solution. Thus, the concentration of NH4OH in the suspension is 8 x 10^{-4} mol/L.

Influence of the dispersant

The content of Duramax D3005 is equal to 1.65 wt.% in respect of the TiO_2 mass. To convert this wt.% in vol.%, the employed formula is:

$$vol\% = \frac{\rho(TiO2)}{\rho(D3005)}.wt\%$$

Thus, the content of Duramax D-3005 is equal to 5.4 vol.% in respect to the TiO_2 volume. As TiO2 represents 2 vol.%, the amount of dispersant represents 0.11 vol.% of the total suspension volume. The fraction of the total volume of TiO_2 is named F(D3005) for the next calculations.

$$F(3005) = \frac{V(D3005)}{V(total)} = \frac{1}{V(total)}.\frac{n(D3005).M(D3005)}{\rho(D3005)} = C(D3005).\frac{M(D3005)}{\rho(D3005)}$$

With C(D3005) in mol/L, M(D3005) in Kg/mol and ρ(D3005) in Kg/L.

Taking as values F(D3005) = 0.0011; M(D3005) = 2400 x 10^{-3} Kg/mol and ρ(D3005) = 1.16 Kg/L, the concentration of Duramax D-3005 is equal to 5.2 x 10^{-4} mol/L. In the D-3005 commercial solution, the polyelectrolyte content is 35 %, thus the concentration of ions in the suspension is 1,8.10-4 mol/L.

Calculation of the ionic strength

$$I = \frac{1}{2}\sum C(i)z(i)^2$$

where C(i) is the molar concentration and z(i) is the charge of the ion i. In this case, the dispersant and the buffer solution are constituted of ammonium salt. One ion is NH_4^+ and the other is a counter ion of a negative charge equal to -1. The concentration of ammonium in the buffer solution is 8 x 10^{-4} mol.L^{-1} so each type of ion has a concentration of 8 x 10^{-4} mol/L. The concentration of dispersant, which is an ammonium salt, is 1.8 x 10^{-4} mol/L so each ion of the dispersant solution is at the concentration 1.8 x 10^{-4} mol/L. Concluding, I = 9.8 x 10^{-4} mol/L.

APPENDIX 4: DLS analysis of the 0.01 wt.% TiO_2 (Aldrich) suspension as function of the milling methods

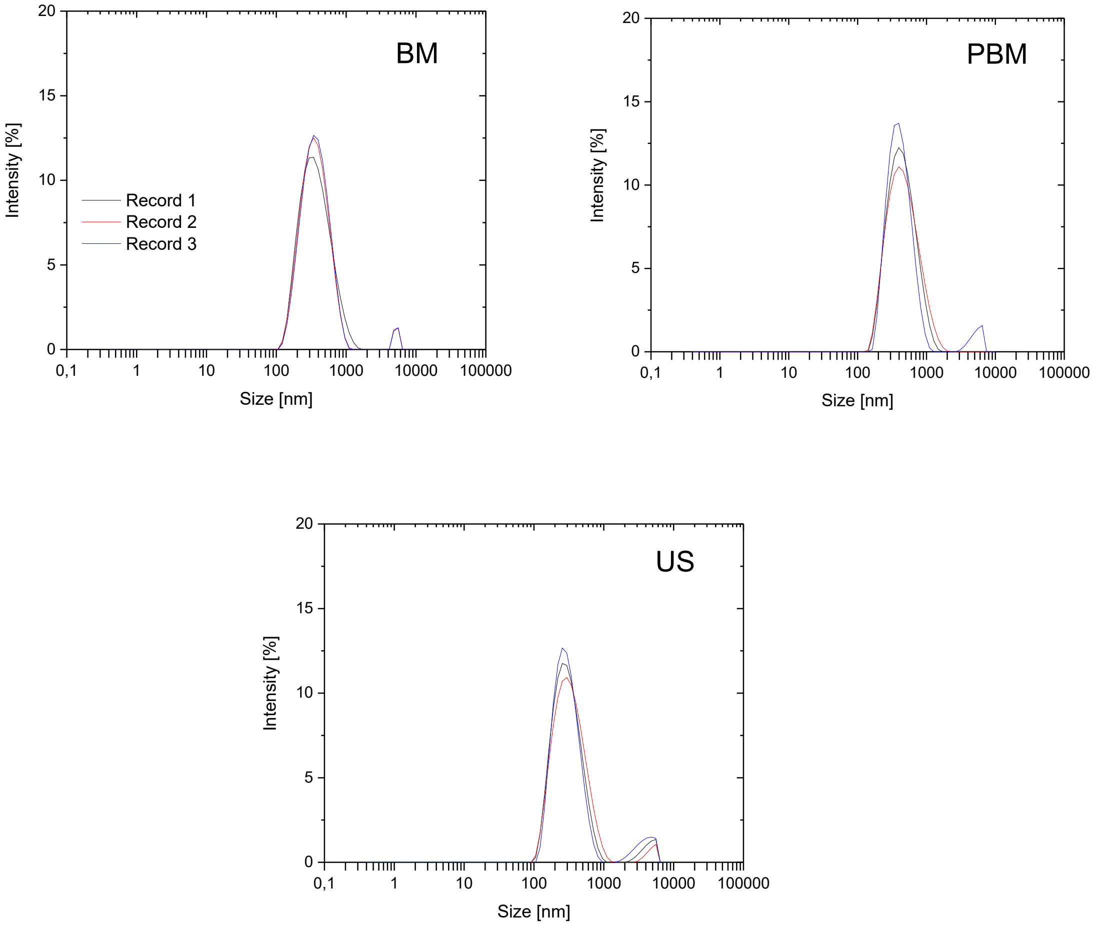

Figure APP2. Intensity graphs of the 0.01 wt.% TiO_2 (Aldrich)/1.5 wt.% D3005 suspension as function of ball milling (BM), planetary ball milling (PBM) and ultrasonication (US)

APPENDIX 5: DLS analysis of the 2 vol.% P25 suspension at different ultrasonication times

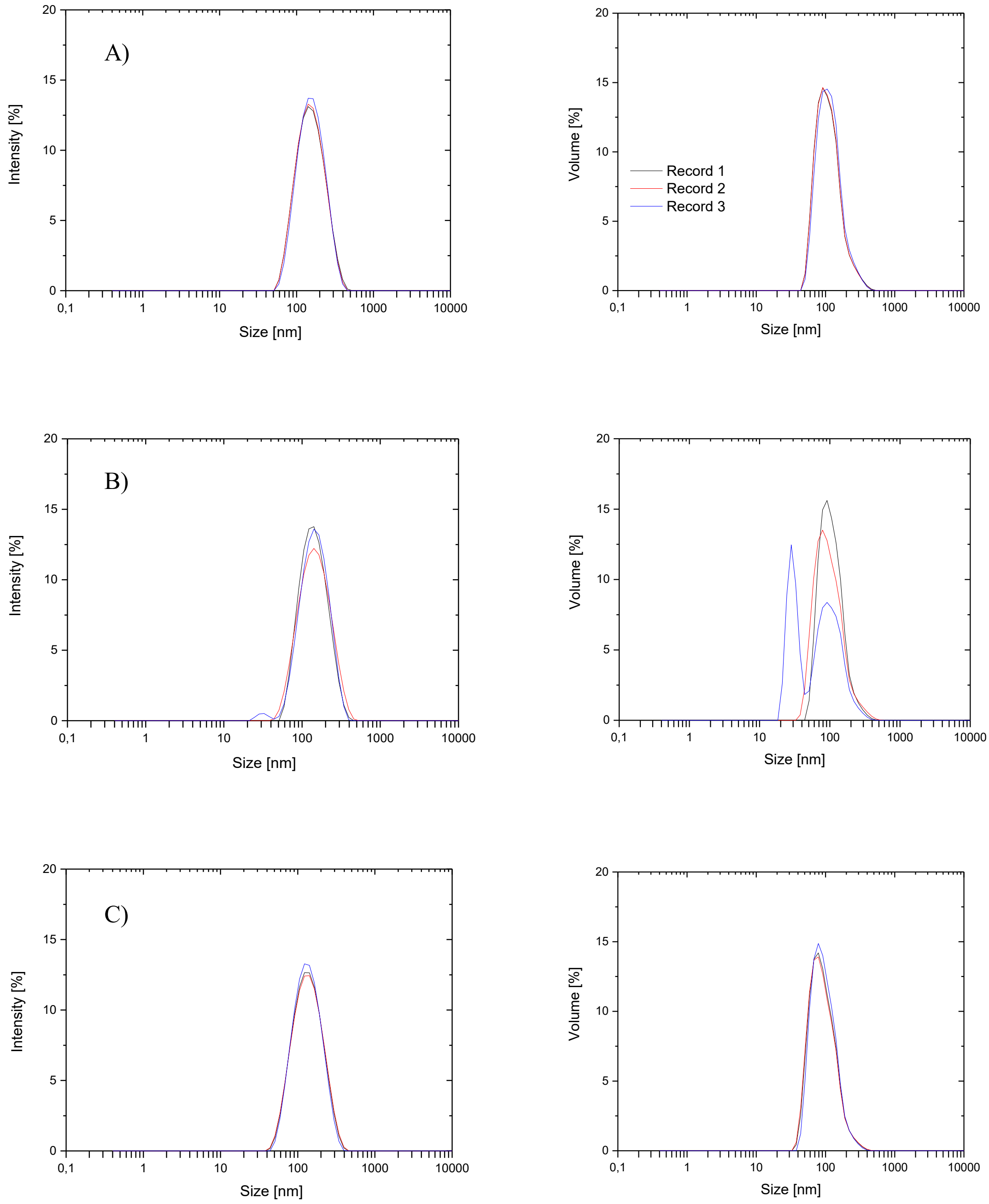

Figure APP3. Intensity and volume graphs of the 2vol.% suspension at different time of ultrasonication: A) 10, B) 30 and C) 50 minutes

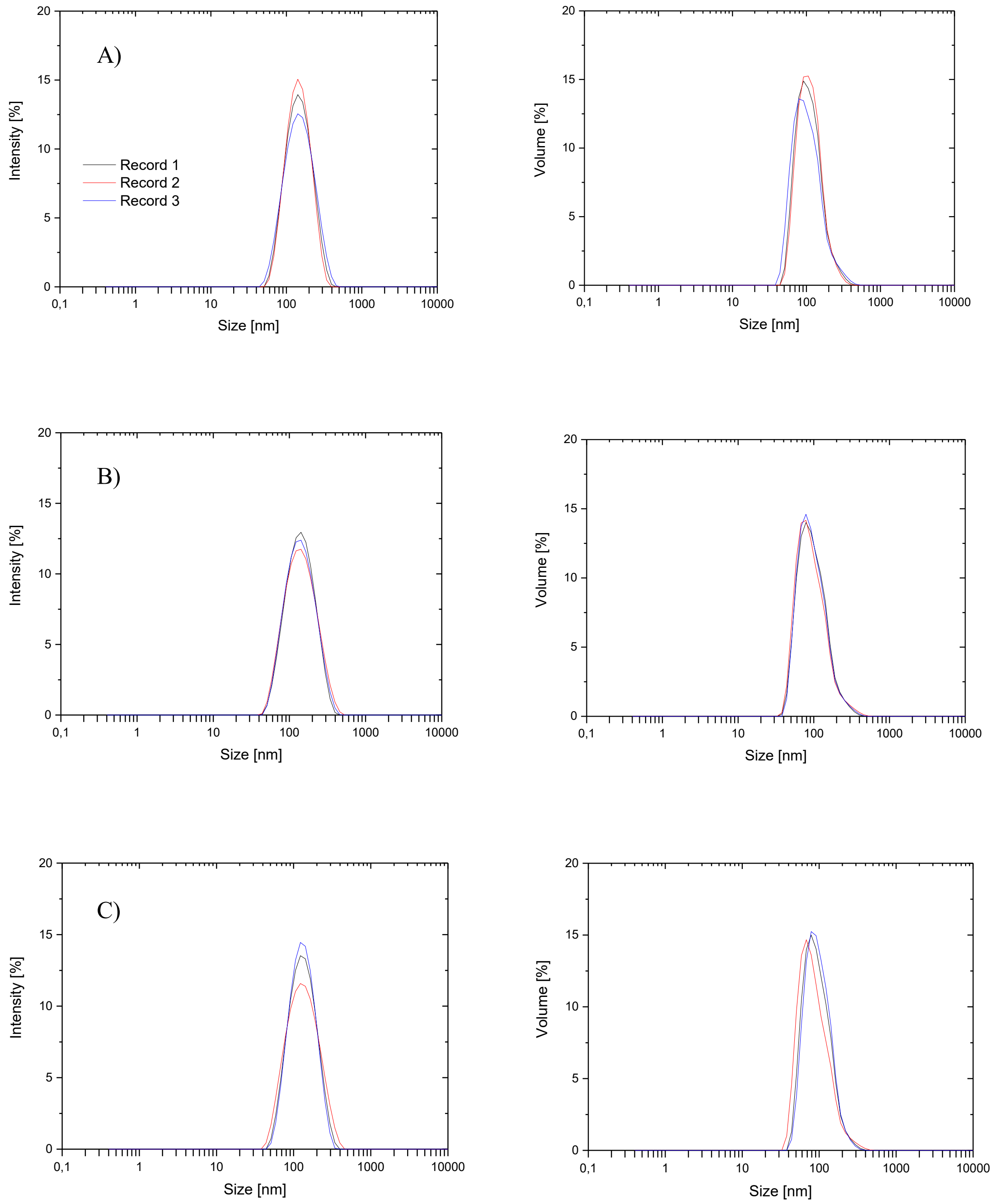

Figure APP4. Intensity and volume graphs of the 2vol.% suspension at different time of ultrasonication: A) 10,_ B) 30 and C) 50 minutes aged for 3 hours

APPENDIX 6: Table of the ejection trials using water and ethanol as ink

Liq.	Pulse voltage [V]	Pulse duration [µs]	Freq [Hz]	Holding Pressure [mbar]	Strobo delay [µs]	Note
Abs EtOH	147	70	1956	SET= -6 READ = -3	300	One single filament where drops can be observed
	158	70	1956	SET= -6 READ = -5,1	240	Liquid filament (2 distinct drops)
	168	70	1956	SET= -6 READ = -5,1	252	Liquid straight filament (1 distinct drops)
	129	99	1956	SET= - 10 READ = -9	186	3 liquid filaments with 3/4 drops
	121	36	1956	SET= -10 READ = -10	236	4 liquid filaments with 2/3 drops
H_2O	160	70	1036	SET= -10 READ = -7,8	300	Unique filament, unique drop, deviated towards the right side
	160	75	1036	SET= -10 READ = -7,8	300	Unique filament, 1 drop and 1straight jet
	69	28	2033	SET= -15 READ = -13,3	64	Drop can't fall, it sticks at the edge
	69	28	2033	SET= -18 READ = -15,4	54	Drop can't fall, it sticks at the edge
	69	27	1036	SET= -15 READ = -11,6	54	Drop can't fall, it sticks at the edge
	69	27	921	SET= -15 READ = -13,8	192	One single drop
	69	27	1611	SET= -15 READ = -15,4	123	Single drop and single filament
	73	21	1611	SET= 15 READ = -13,8	192	Satelitte drops
	73	25	1611	SET= 15 READ = -13,8	224	Single drops